UNIVERSITY OF CALIFORNIA SAN DIEGO

SAN DIEGO STATE UNIVERSITY

Assessing Cell Mechanotype as a Prognostic Marker for Metastatic Risk and Recurrence of Cancer

A dissertation submitted in partial satisfaction of the requirements
for the degree Doctor of Philosophy

in

Engineering Science (Bioengineering)

by

Benjamin Yeoman

Committee in charge:

University of California San Diego

Professor Adam Engler, Co-Chair
Professor Stephanie Fraley
Professor Jing Yang

San Diego State University

Professor Parag Katira, Co-Chair
Professor Sam Kassegne

2022

The Dissertation of Benjamin Yeoman is approved, and it is acceptable in quality and form for publication on microfilm and electronically.

University of California San Diego
San Diego State University

2022

DEDICATION

To my family, friends, and friends of friends, I finally did it. I am done and I would like to dedicate this to all of you. I am eternally grateful for your endless support, for without it this would not have been possible.

TABLE OF CONTENTS

LIST OF FIGURES

LIST OF TABLES

LIST OF ABBREVIATIONS

ECM   Extracellular matrix

PPFC   Parallel plate flow chamber

WA   Weakly adherent

SA   Strongly adherent

SF   Stress fiber

FA   Focal adhesion

TME   Tumor microenvironment

FACS   Fluorescence-activated cell sorting

ACKNOWLEDGEMENTS

I would like to take this opportunity to express my sincere gratitude for all of those who supported me throughout my scientific journey. Firstly, I would like to thank my advisors, Professors Parag Katira and Adam Engler, for providing me with their constant guidance and support. I have learned a great deal from their mentorship and it has been an incredibly rewarding experience being a part of both their labs. I would also like to thank my thesis committee members, Professors Sam Kassegne, Stephanie Fraley, and Jing Yang, for there inspiring lectures and guidance throughout my graduate school tenure. I would also like to thank the National Cancer Institute for their training grant, as it helped make this work possible. Thank you also to my fellow lab members, in the Engler and Katira labs, and their support throughout this project. You all made PhD experience truly exciting and unforgettable, and I feel our scientific discussions were invaluable in this process. I am especially grateful for the hard work of my undergraduate students, Gabe Shatkin and Izzy Williams, both of whom are incredibly talented and contributed immensely to this work.

Lastly, I would like to thank my friends and family for all of their moral support during the harder parts of this project and life in general. And of course, to Jacqui, the love of my life, for her unending love and even more inspiration. You have always pushed to achieve more than I ever thought I could. I know I am stronger with you in my life and together we can achieve anything.

Chapter 1, in part, is a reprint of the material as it appears in Shatkin, G., Yeoman, B., Birmingham, K., Katira, P., Enger, A.J. "Computational Models of Migration Modes Improve our Understanding of Metastasis" APL Bioengineering, 2020. 4: 041505. The dissertation author was a co-author of this paper.

Chapter 2, in full, is a reprint of the material as it appears in Beri, P., Popravko, A., Yeoman, B., Kumar, A., Chen, K., Hodzic, E., Chiang, A., Banisadr, A., Placone, J.K., Carter, H., Fraley, S.I., Katira, P., and Engler, A.J. "Cell Adhesiveness Serves as a Biophysical Marker for Metastatic Potential." *Cancer Research*, 2020. 80(4): 901-911. The dissertation author was a co-author of this paper.

Chapter 3, in full, is a reprint of the material as it appears in Yeoman, B., Shatkin, G., Beri, P., Banisadr, A., Katira, P., and Engler, A.J., "Adhesion Strength and Contractility Enable Metastatic Cells to become Adurotactic." *Cell Reports*, 2021. 34(10): 108816. The dissertation author was the primary author of this paper.

Chapter 4, in full, has been submitted for publication of the material as it may appear in Birmingham, K., Yeoman, B., Beri, P., Tuler, J., Williams, I., Kumar, A., Klein, S., Katira, P., and Engler, A.J. "Stromal Cell Adhesion Predicts Severity of Metastatic Disease." *Nature Biomedical Engineering*, 2022. The dissertation author was a primary author and equal contributor in the authorship of this paper.

VITA

2013 Bachelor of Science in Biology (Bioengineering), San Diego State University

2017 Master of Science in Bioengineering, San Diego State University

2022 Doctor of Philosophy in Engineering Science (Bioengineering), University of California San Diego and San Diego State University

PUBLICATIONS

Yeoman, B., and Katira, P. (2018) "Predicting Persistence Length of Cell Migration in Dense 3D Matrix – Effect of Matrix Fiber Density and Pseudopod Activity", *PLoS One.* 13(11): e0207216.

Collins, T., **Yeoman, B**., and Katira, P. (2020) "To Lead or to Herd: Optimal Strategies for Collective Cell Migration in Heterogenous 3D Environments", *Biomechanics and Modeling in Mechanobiology*. 19: 1551–1564.

Beri, P., Popravko, A., **Yeoman, B**., Kumar, A., Chen, K., Hodzic, E., Chiang, A., Banisadr, A., Placone, J.K., Carter, H., Fraley, S.I., and Engler, A.J. (2020) "Cell Adhesiveness Serves as a Biophysical Marker for Metastatic Potential" *Cancer Res*earch, 80(4): 901-911.

Shatkin, G., **Yeoman, B**., Birmingham, K., Katira, P., and Engler, A.J. (2020) "Computational Models of Migration Modes Improve our Understanding of Metastasis" *APL Bioengineering*, 4: 041505.

Banisadr, A., Eick, M., Beri, P., Parisian, A.D., **Yeoman, B**., Placone, J.K., Engler, A.J., and Furnari, F. (2020) "EGFRvIII uses Intrinsic and Extrinsic Mechanisms to Reduce Glioma Adhesion and Increase Migration" *J Cell Sci*, 133(24): jcs247189.

Yeoman, B., Shatkin, G., Beri, P., Banisadr, A., Katira, P., and Engler, A.J., (2021) "Adhesion Strength and Contractility Enable Metastatic Cells to become Adurotactic" *Cell Reports*, 34(10): 108816.

Teng, E. L., Masutani, E., **Yeoman, B**., Fung, J., Lian, R., Ngo, B., Kumar, A., Placone, J. K., Lo Sardo, V., and Engler A.J. (2021) "High shear stress enhances endothelial permeability in the presence of the risk haplotype at 9p21.3" *APL Bioengineering,* 5, 036102.

Birmingham, K., **Yeoman, B.**, Beri, P., Tuler, J., Williams, I., Kumar, A., Klein, S., Katira, P., and Engler, A.J. (2022) "Stromal Cell Adhesion Predicts Severity of Metastatic Disease" Under review at *Nature Biomedical Engineering*.

ABSTRACT OF THE DISSERTATION

Assessing Cell Mechanotype as a Prognostic Marker for Metastatic Risk and Recurrence of
Cancer

by

Benjamin Yeoman

Doctor of Philosophy in Engineering Science (Bioengineering)

University of California San Diego, 2022
San Diego State University, 2022

Professor Adam Engler, Co-Chair
Professor Parag Katira, Co-Chair

The high mortality rate of cancer is associated with metastasis of the primary tumor and can drastically reduce a patient's 5-year survival rate. Patient outcomes typically scale with the rate of cell dissemination from the primary tumor, but the lack of a universal molecular prognostic marker and cell heterogeneity within the tumor complicate calibrating patient care. Even though there is limited overlap in the genetic mutations and biochemical changes that arise in specific cancer types, all solid tumor cells must detach, migrate, and invade the surrounding

tissue in order to metastasize. The cell mechanotype and its effect on cell-ECM dynamics plays an important role in this process, and offers a more conserved feature across the variety of different cancers. This dissertation aims to utilize these characteristics – specifically adhesion strength between the cell and the extracellular matrix – to assess the metastatic risk of a given cancer cell population. We first examined how heterogeneity in cell-ECM adhesion strength within an isogenic population of cancer cells could present intrapopulation differences in metastatic ability. Weakly adherent cells from a number of different cancer types consistently displayed greater migration speeds in vitro compared to their strongly adherent counterparts. Biophysical modeling and experimental validation suggest that differences in intra-cellular actomyosin activity are the proximate driver for differences in migration speed, rigidity sensing, and durotactic behavior. Using a murine mammary tumor model, we then demonstrated the prognostic capabilities of a divergent parallel-plate flow chamber to measure the adhesion strength and cancer cell percentage of tumor and stromal biopsies, and found that less adherent cancer cells generate more secondary metastases. Taken together, these studies demonstrate the utility of using adhesion strength as a biophysical marker to predict metastatic risk. Our microfluidic device that utilizes shear to measure adhesion strength may provide the means to accurately assess the metastatic potential of a patient's primary tumor and better inform treatment options.

CHAPTER 1. UNDERSTANDING METASTASIS THROUGH COMPUTATIONAL AND EXPERIMENTAL MODELS

1.1 Abstract

Tumor cells migrate through changing microenvironments of diseased and healthy tissue, making their migration particularly challenging to describe. To better understand this process, computational and experimental models have been developed to interrogate how the properties of the cell and its environment affect migratory potential and enable it to become metastatic. In this chapter, I will give an overview of the various approaches that have been used to account for the physical environment's effect on cell migration in both computational and experimental models, with a focus on their application to understanding cancer metastasis and the related phenomenon of durotaxis. I will first discuss some the relevant computer models used to describe both mesenchymal and amoeboid modes of migration, and then highlight how *in vitro* experiments are engineered to recreate the architectural, mechanical, and biological features of the tumor microenvironment. Lastly, I will conclude with perspective elements that would enhance their ability to recapitulate the microenvironment both *in vitro* and *in silico* and survey potential applications for diagnosing diseases or identifying therapeutic targets.

1.2 Introduction

Cell migration is an integral part of many biological functions and pathological conditions, from immune response and wound healing to organ development and cancer metastasis. A cell's ability to move through space and reach its destination is critically important for it to fulfill its intended function. Depending on the cell type and the circumstances it finds

itself in, cells can adopt different modes of migration[1,2], but all modes of migration can be described with the same basic steps: membrane extension, attachment formation, contraction, and rear release[3]. Mechanisms that control each step and the degree to which each step affects migration varies with cell migration mode, as well as the cell's environment. Although a continuum of possibilities exists between the extremes of migration modes, two main subsets of migration, ameboid and mesenchymal migration, are among the most described, especially in the context of—but not exclusive to—cancer metastasis.

Ameboid migration occurs both in single-celled organisms, such as the ameba *Dictyostelium discoideum*, and within specific cell types in multicellular organisms, such as neutrophils[4]. Cells undergoing ameboid migration exhibit rounded protrusions, i.e., blebs, and show little spreading on their substrate. This mode of migration progresses through a three-step blebbing cycle: nucleation, growth, and contraction (Figure 1.1A). The formation and expansion of these blebs are driven by weaknesses in the actin cortex and cytoplasmic pressure differences that cause the cellular membrane to expand outward[5]. During the nucleation and growth phases, it is not clear to what extent the actin cortex ruptures, but there is a clear separation between the two[6]. As blebs transition from growth to contraction, myosin causes the bleb to retract back into the main body of the cell, which can result in an overall movement of the cell toward the direction of the bleb expansion[7]. It should be noted that ameboid cells can exhibit other types of protrusions that are closer to the mesenchymal end of the migration spectrum, i.e., pseudopods[8]. Pseudopods initiate as blebs; however, their expansion from the cell body is coupled with continuous active expansion of F-actin in the underlying cellular membrane. Both types of protrusions can form on the same ameboid cell, and blebs and pseudopods have been shown to operate cooperatively during chemotaxis[9]. Regardless of the main protrusion type,

ameboid cells exhibit clearly defined polarization with a leading and trailing side[10]. They can

also travel at relatively fast speeds compared to other modes of migration[11] (~10 µm/min)

depending on their surroundings. Additionally, these cells do not form strong focal adhesions

with the surrounding extracellular matrix[4] (ECM) and tend to be more processive in their

migration, especially in the dense matrix[12].
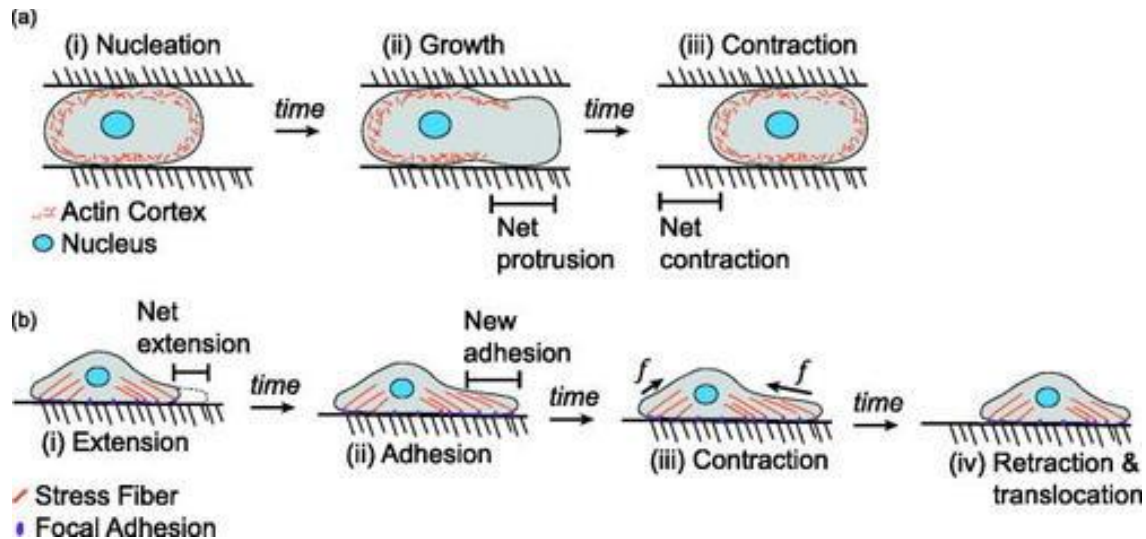
Figure 1.1: Processes of ameboid and mesenchymal migration in cancer
(A) Ameboid migration typically occurs as a three-step blebbing cycle with nucleation, growth, and contraction
steps. (B) Mesenchymal migration typically involves a different process wherein cells extend their leading edge and
adhere, contract, and release their trailing edge.

Conversely, a wide variety of migrating cells contract against focal adhesions in

protrusions from the main cell body to move in a second method often termed mesenchymal

migration (Figure 1.1B). Protrusions used in this mode are typically classified as filopodial or

lamellipodial, with the former being thin spindle-like protrusions and the latter being sheet-like

protrusions[3]. Additionally, cells in the mesenchymal mode form strong focal adhesions to the

ECM[13–15] and, as a result, appear to spread over their substrate; this mode is typically slower than

ameboid migration[4] and is classically observed on two-dimensional substrates. In addition to

morphological differences, there are mechanistic differences between the two modes of

migration; cytoplasmic pressure gradients drive ameboid migration[12] often in confined settings,

3

whereas mesenchymal migration is driven by actin polymerization and the active maturation and turnover of focal adhesions coupled with actin-myosin contraction[16] across a more spread cell. This different mechanism is not entirely distinct from the pressure-driven flowing actin networks of ameboid migration; mesenchymal migrating cells exhibit a retrograde actin flow away from the leading edge and toward the main cell body[17,18]. However, computational models typically treat different migration modes as entirely distinct for the sake of simplicity and are used to answer specific questions. Contact guidance between these modes is also markedly different and results in proliferative differences that could underlie migration[19] and hybrid cell formation[20]. A summary of major differences in migration outcomes[21–30] is shown in Table 1.1.

Table 1.1: Major performance differences between migration modes for cancer cells

	Amoeboid	Mesenchymal	Reference
Migration Speed	2-25 µm/min	0.1-1 µm/min	21–23
Persistence	Low	High	24,25
Morphology	Rounded	Elongated	23,26
ECM Attachment	Weak, short term, lower integrin expression	Integrin clusters forming focal adhesions	23,27
Migration in ECM	Squeezing or blebbing through ECM pores	Adhesion mediated tractions, ECM degradation	23,28,29
CSK Organization	Actin cortex	Actin meshwork, contractile stress fibers, microtubules	23,29,30

Although these two extreme modes represent a majority of cellular movements observed *in vivo* and *in vitro* (and models describing mesenchymal migration are significantly more common than ameboid migration), several other modes, both intermediate and distinct, have also been described but were omitted here for clarity[31]. The use of these modes often depends on the environment's dimensionality (which can regulate adhesion assembly[32]), on the cell type, and on the receptor-ligand pairs as with selectins used in leukocyte migration[33]. These modes often exhibit distinct features, making them easily identifiable, such as the crescent moon

shape and gliding motion of keratocytes[34], but exist in a continuum between mesenchymal and ameboid modes.

1.3 Migration and Cancer Metastasis

Cancer is the second leading cause of death in the United States, and the vast majority of its mortality is associated with secondary tumor formation[35]. In order for cancer cells to metastasize and form secondary disease, they must migrate out of the primary tumor, intravasate into the bloodstream, and then extravasate into other tissues throughout the body[36]. Cells within tumors are also very heterogeneous, making it difficult to separate indolent cancers from deadly ones, as only a subset of cells is able to disseminate from the main tumor and the others remain stationary and benign. Alongside migration mode, directionality is incredibly important for metastasis, yet remains poorly understood in certain contexts. For example, cancer cell chemotaxis (i.e., migration along a chemical concentration gradient) has been studied in-depth in ameboid cells but comparatively little for mesenchymal cells[4,37]. More recently, effort has been made to understand the effect of cells' mechanosensing on migration. For example, the progression of metastatic breast cancer has been related to the levels of mechanosensing proteins in stiff ECM[38]. Cells migrate at different speeds depending on substrate stiffness and oftentimes exhibit durotaxis, the ability to sense and migrate up a stiffness gradient[39–41]. However, this seems counterintuitive for understanding cancer metastasis, as often times, the tumor microenvironment becomes much stiffer than the surrounding healthy stroma due to matrix secretion and cross-linking by cancer-associated fibroblasts[42,43]. In these cases, the metastatic cells must exhibit adurotactic behavior in order to leave the primary tumor, which further complicates our current understanding of cancer cell migration and metastasis. Adding yet another level of complexity is the observation that tumor cells migrate in both the ameboid and

mesenchymal modes and, depending on their environment, can switch between the two[1,2,44]. They can also migrate individually or collectively[45], and their migration is highly dependent on the physical properties of their niche, such as stiffness, porosity, dimensionality, and toporgaphy[46], which can change as a result of clinical care[47]. Despite these many influences, tumor migration models, thus far, largely focus on intracellular mechanisms governing mesenchymal and ameboid modes, and thus, we will describe the effects of additional modes and matrix properties in the context of model limitations later.

1.4 Computational Modeling of Cell Migration

Cancer cell interactions are often very complex; reductionist approaches using model systems, e.g., microfluidic bioreactors[48], explore many isolated variables, and more complex models may even include the vasculature to study extravasation[48,49]. However, despite the simplicity of these model systems, fidelity with *in vivo* disease progression may be limited or at least require context and necessitate significant engineering to generate robust datasets. Computational models, however, may offer an alternative—where applicable—to create and test reasonably complex niches *in silico* to understand migration mechanisms prior to experimental studies, thus better informing the design of more effective and efficient experimental studies.

A key consideration for any computational model is the complexity of its physics; over- or under-determined systems can limit applicability and predictive value. With respect to cell migration, many models consider the following key concepts: force balance, mass conservation, biochemical activity, active forces, and passive forces[50] (Figure 1.2). Force balances are used in all models to determine the net force magnitude and direction, which governs a cell's movement. Mass conservation is especially prevalent in models with a focus on protrusion dynamics or morphology changes in migrating cells to determine cells' changing shapes with a constant mass.

6

Biochemical activity connects intra, inter, and extracellular signaling to cellular and extracellular mechanics. Active forces include forces generated by cytoskeletal dynamics such as actin and microtubule polymerization and depolymerization and actomyosin contractility. On the other hand, passive forces include reaction forces arising within cells, between neighboring cells, and between cells and the surrounding environment elastic strain, viscous drag, and molecular friction[50]. The integration of these components in the model, the degree to which they affect each other, and, more broadly, overall migration depends on a number of intracellular and extracellular parameters in the model's framework. A brief overview of some of the modeling approaches discussed below[51–68], and associated equations, is shown in Table 1.2. Note that this is meant to introduce readers to the various ways that physical laws governing cell migration can be described mathematically and is meant to direct readers to specific examples where these methods are applied. As computational costs continue to go down, the equations and models can become more detailed and combine multiple approaches into hybrid models. For the remainder of this section, we will broadly discuss how the above-described key concepts are modeled and affect cell migration mode citing specific examples.
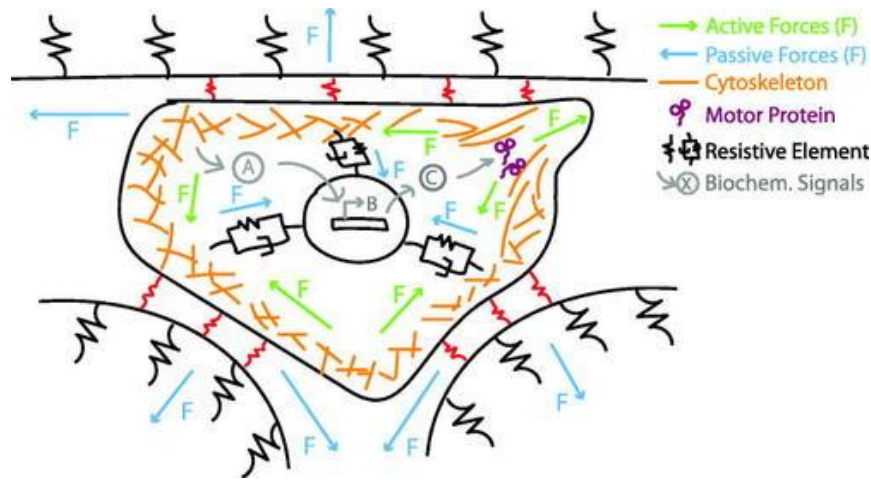
Figure 1.2: Conserved components of computational models of cancer migration
Four concepts are typically present to some degree in computational models of migration: force balance, mass conservation, active forces, and passive forces. Each is illustrated here and where active forces are those generated by motor proteins and polymerization and depolymerization of cytoskeletal filaments and passive forces are those from the viscoelastic parts of the cytoskeleton and ECM as well as from molecular friction.

Table 1.2: List of frequently physical frameworks used to model cancer cell migration and their applications.

Common Modeling Approaches	Applications & Examples
Chemo-mechanical models based on Force dependent reaction kinetics $F(\mu) - \gamma(F,n)v = 0$ … Force balance between active forces driven by chemical potential, μ, dissipative forces, γv. $\gamma(F,n) = K\tau_0 \exp(-\frac{F}{nF_0})$ … stiffness, K, and number, n, and kinetics of molecular bonds, τ_0 dictate drag coefficient, γ	Used to model sub-cellular processes such as cell-substrate bond formation, filament polymerization and gliding and mechanosensing-based changes to predict resulting cell adhesion, traction, and migration (e.g., various spring/dashpot models[51–53], active matter models[54], and molecular clutch models[55]).
Agent-based models focusing on force balance between individual cells and their environment $\vec{F}_{active} + \vec{F}_{passive} + \vec{F}_{dissipative} = 0$ … or an energy minimization approach $E = \sum \lambda_i (A_i - A_0)^2 + \sum \sigma_{ij} l_{ij} + \sum \frac{dU}{d\vec{r}_i} \cdot \vec{r}_i$	Used to model cell populations interacting with each other and the environment. Coarse grained to implicitly include effects of various sub-cellular processes (e.g., force-based models[56–58], energy-based models[59,60], and lattice-based/cellular Potts models[61–63]).
Thermodynamic models based on equilibrium and non-equilibrium Work-Free Energy Change relationships $\Delta F = \sum \Delta \mu_i - k_B T \ln \frac{\Omega}{\Omega_0}$ … Free energy change of the system $W = \int F_{active} dx$ … work done by the system Equilibrium … minimize (ΔF) Non-Equilibrium … $\Delta F \gtrsim W$	Used to model both cellular and sub-cellular processes and assess the energetic states that the system can occupy (e.g., free-energy-based models[64,65]).
Continuum Phase-Field models $\frac{d\Phi_i}{dt} + \vec{v}_i \cdot \vec{\nabla} \Phi_i + \frac{\delta F}{\delta \Phi_i} = 0$ … Describes the dynamics of the cell shape in response to free energy changes. The free energy functional, F, is chosen so that minima correspond to phases (i.e., intracellular and extracellular environment) of the system.	Used to describe cell and surrounding free space as an evolving phase-field, with the moving boundary representing the cell membrane. Well suited to describe collective migration[66,67] and migration of cell monolayers[68].

1.4.1 Mesenchymal migration models: applications and directions

Computational models describing mesenchymal cell migration primarily focus on intracellular active forces driving protrusion and retraction of lamellipodia and filopodia, balancing these forces against elastic, viscous, and friction forces within and outside the cell, and mass balance that defines the cell shape as the cell migrates under the action of these forces[50,69–71]. At the nanoscale, these models can focus on the dynamics of actin polymerization and depolymerization, force generation by individual myosin motors, binding and unbinding of adhesion receptors to the extracellular matrix, clustering of adhesion receptors and maturation of adhesion sites, and binding of polymerized actin filaments to these receptors to form adhesion complexes[27,72,73]. At this scale, models incorporate force generation and sensing aspects such as conformational changes in adhesion complex proteins, recruitment of additional actin-myosin fibers, and branching of actin fibers. At the mesoscale, models focus on cell spreading, filopodial and lamellipodial protrusion and contraction, coupling between the nucleus and the cytoskeleton, viscoelastic strains within the cytoskeleton and the nucleus under the influence of active and passive migration forces, and resulting cell shape changes[30,61,70,74,75]. Models at this scale are particularly useful for predicting cell shape dynamics and interactions between two neighboring cells or a single cell and its environment. At the microscale, the focus of modeling is on overall cell migration dynamics under the influence of a driving force balanced by the drag forces from the environment[56–58,76,77]. At this scale, the goal of the models is to predict cell migration velocity and path persistence as a function of the mechanistic interactions between the cell, its neighbors, and the surrounding extracellular matrix. Computational models may focus on a specific length scale or combine multiple length scales to predict migration dynamics. Models can also vary in their representation of the extracellular environment. For example, to describe cell migration on

a 2D substrate, the ECM can be described as a continuous elastic material or discretized into a collection of binding sites connected to springs[61,63,78–80]. In 3D, the ECM can be described as a viscous continuum, discretely as a collection of randomly or uniformly distributed binding sites, or as fibers distributed randomly or along the grid in 3D space[56,62,76,81,82]. Depending on the choice of the ECM model, various aspects of cell–ECM interactions can be integrated such as ECM degradation, ECM remodeling, contact guidance along aligned fibers, and squeezing of cell through ECM pores. A common thread between all these models of mesenchymal cell migration is that the migration is driven by forces generated within long protrusions that grow along the surface in search of sufficient binding sites in 2D and along the length of fibers in 3D.

The primary goal of these computational models has been to predict how fast and persistently cells will migrate along or within a given substrate depending on their specific mechanical and chemical properties. Models have also been successful in predicting experimentally observed behavior of the biphasic dependence of migration speed on ECM density, adhesivity, and stiffness[41]. Models can also recreate qualitative trends in migration persistence, which have been observed experimentally and clinically. More recently, modeling of experimentally observed emergent phenomena such as chemotaxis, durotaxis, haptotaxis, and contact guidance, which direct cells along specific directions, is gaining attention. How mechanobiology affects migration, i.e., how do changes in niche parameters direct processive migration and ultimately intravasation, is of extreme importance in understanding processes such as wound healing and cancer metastasis. Most adherent cells migrate toward a stiffer region of a substrate when presented with a gradient[83], i.e., "durotax;" yet, tumors are inherently stiff relative to adjacent, soft stroma *in vivo*[84,85]. created by cancer-associated fibroblasts. This creates a cancer cell "migration paradox" where tumor cells must migrate down ECM stiffness gradients

that otherwise support migration in the opposing direction (Figure 1.3). Here, we will focus on a

few mesenchymal cell migration models that explain cancer cell durotaxis and their applicability

toward answering the cancer cell migration paradox. That being said, it is important to note that

we are restricting our discussion and this concept to the disseminating cells from the tumor.

Many other cells must migrate toward the tumor, i.e., durotax, including inflammatory cells,

among others.
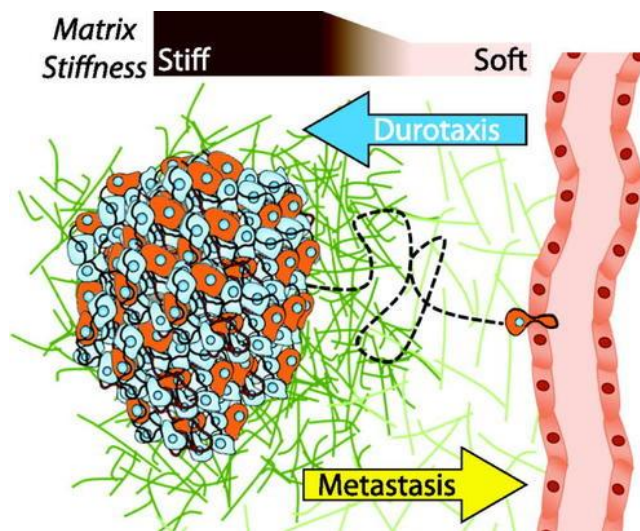
Figure 1.3: The migration paradox
Most cells migrate toward stiffer regions of tissues in a process called durotaxis. However, tumor cells must migrate
from stiff tumors through the progressively softer matrix to disseminate from a tumor core and intravasate into the
blood stream. This metastatic migratory process is counter to conventional thought on stiffness gradient migration,
and it is not clear which migration mode, if any based on available data, permits such migration. Note that for
simplicity, additional cell types, e.g., cancer associated fibroblasts, have been omitted but play a key role in niche
remodeling nonetheless.

To start, many models describe migrating cells as polarized with a higher probability of

protrusion at the leading edge and retraction fibers at the trailing edge. Focal adhesions form

preferentially along the leading edge and dissociate more frequently along the trailing edge,

resulting in net motion in the direction of the leading edge[3]. Some computational models

replicate durotaxis on a surface using polarized cell filopodia, which are more likely to grow

along elastic fibers aligned along an increasing stiffness gradient[81]. This approach to simulating

migration succeeds in predicting the general movement of durotactic cells and in creating a more

realistic representation of ECM fiber networks rather than conventional models that treat the substrate as a continuum. Yet, such a rigid integration of durotaxis is not without disadvantages, e.g., durotactic behavior has to be built into the model, rather than durotactic behavior arising from it. Furthermore, while the elastic fibers can be deformed, the cell cannot remodel or degrade them. Thus, from such polarity-based models and those that take similar approaches, e.g., adhesions that bind more strongly on the stiffer region than softer regions forcing polarized shapes a priori[86], it may be difficult to infer mechanisms of durotaxis or even adurotaxis as observed in cancer *in vivo*. These models are, however, convenient to study the effect of inter-cellular heterogeneity in these parameters on overall population dynamics when predicting collective cell behavior. Indeed, within a tumor, not all cells metastasize, and thus, cancer migration models should highlight both cellular and temporal heterogeneity[87] when describing gradients.

One of the early models that explained the origin of durotactic behavior rather than making it an intrinsic property of migrating cells was by Schwarz *et al.*, which used a simple 2 spring attachment-detachment model between the actin myosin force generating elements, cell membrane attached adhesion protein, and the substrate[51]. The model showed that as the substrate stiffness increases, the rate at which the force is generated within the actin–myosin filament increases, leading to larger overall traction forces within the lifetime of a cell–substrate adhesion bond. The increase in traction forces on stiffer substrates drives cell migration up the stiffness gradient explaining durotaxis. This phenomenon has since been integrated as an *a priori* mechanism of cell migration in a number of other models. A more recent addition to models explaining durotaxis is based on a rigidity sensing-based change in the biochemical activity of motor protein regulating units within the cell[72]. Increased feedback from a stiffer

substrate drives increased myosin activity and higher speeds for cells in stiffer regions, driving an accumulation of cells up a stiffness gradient. A third alternate model focuses on the mechanical response of the ECM fibers rather than that of the cell itself. The model is based on fiber mechanics that suggests that the deformation/extension of a fiber decreases as a cell gets closer to the point where the fiber is crosslinked to a stiffer environment. This generates a stronger passive force on the cell, pulling the cell toward the stiffer regions and driving durotaxis[81]. There are many other models that explain durotaxis through variations or combinations of the above-described themes that we are not discussing here. A more recent model[88] by Heck *et al.* suggests yet another possible explanation for durotactic behavior. This model accounts for ECM as an obstacle that the cell must negotiate or degrade; this type of confined migration is often observed in dense tissue where degradation by the cancer cell proceeds filopodial extension[89] and requires significant deformation (which can be measured in high throughput with fluidics[90]). The model predicts that migration is most affected by ECM stiffness, cell adhesion strength, and protrusion properties, e.g., number, lifetime, and length. The model shows the standard correlation between matrix stiffness and migration speed, consistent with past models and experimental observation using degradation and filopodial extension[91]. They also show that adhesion turnover makes migration more processive. By incorporating force-dependent adhesion turnover rates and increased forces in stiffer ECM regions, they show an additional mechanism for durotactic behavior driven by increased persistence. A connection between processive migration and adhesion strength is also supported experimentally as seen when a weakly adherent phenotype results in a reduced disease-free interval[92]. The implication that protrusion activity and matrix deformation in three-dimensions, not the development of robust focal adhesions as in two dimensions, as the origin of their

processivity, may be consistent with some results in three dimensions[28].

The models discussed so far cover most known aspects of mesenchymal cell migration and also can be used to describe a number of emergent phenomena. With regard to durotactic behavior, they all suggest using one argument or another that cells should durotax, and for the most part, adherent cells do so. However, the cancer cell migration paradox of metastatic cells migrating against a stiffness gradient to metastasize still remains unanswered. It may be necessary to develop mechanistic models that explain anti-, a-, and durotactic migration that focus not on the ECM but rather on the cytoskeletal elements that drive mesenchymal migration; here, we summarize two such models. To interrogate such cytoskeletal elements, the most common mesenchymal model used has been the molecular motor-clutch[93], which employs multiple molecular motors to pull actin filaments toward the cell body on a compliant, continuous substrate; conversely, the molecular clutch binds to actin stochastically and links it to the extracellular environment via a force-dependent Bell model connection[94]. These models typically predict a stiffness-dependent relationship for migration where on compliant substrates, the motors undergo load-fail cycles, whereas on stiff substrates, the complex slips. This model predicts biphasic behaviors in force and migration that can reinforce adhesion[95], with an optimal stiffness region that cells will most likely migrate to. The model, thus, does not always predict durotaxis or antidurotaxis, but rather migration in the direction of the preferred stiffness for a given cell type. Optimal stiffness for a cell type is dependent on the actomyosin contractile force that the cells can generate and the number of clutches between the cell and the substrate. Overall, the clutch model may provide a possible reason for the adurotactic migration of metastatic cancer cells away from a stiff tumor ECM, but validation of experimentally observation of adurotaxis by highly metastatic cancer cells needs to be further explored. Another model in which the

mechanical environment can be considered in migration is an equilibrium thermodynamics model. This model provides an alternative way to characterize the two-way feedback loop between cell contractility and matrix realignment. This model calculates the total change in free energy of the system, consisting of the energies of the cell, matrix, and adhesions to determine whether or not migration will occur as the system tries to move into a lower energy state[65]. Similar to the clutch model, this thermodynamic migration model predicts a biphasic migration response to matrix stiffness and depends on the contractile force that a cell can generate and the strength of its adhesions. It is possible to envision that in the presence of gradients, cells could adurotactically migrate to an optimum away from the tumor, thus achieving goals similar to the clutch model.

Overall, due to important fluctuations in force[96], heterogeneous adhesion within a tumor[92], and stiffness gradients (vs changing but static substrates in these models) on the stroma[85], there is a need for new models where these or similar parameters are incorporated together, e.g., maximum force generated by a stress fiber, catch bond dynamics, etc. Changes to the force-bond lifetime relationship could then result in anti-, a-, and durotactic behavior depending on how each parameter varies with the others.

1.4.2 Ameboid migration models

Ameboid migration is dominated by propulsive membrane blebbing, i.e., the key concept of force balances, rather than spreading and forming strong focal adhesions to their substrate, i.e., the key concept of active contractile forces[4]. It also relies less on modification or degradation of the adjacent ECM and more so on becoming highly deformable and pushing through matrix pores. Despite the differences between mesenchymal and ameboid migration, cancer cells display unique plasticity in their ability to switch between modes[24,97], making our

understanding of ameboid migration even more critical. Unlike mesenchymal migration, ameboid migration models reviewed here tend to focus on intracellular parameters, e.g., the development of pressure gradients to form blebs or propel the cell forward[12], rather than on the cells' physical environment. Despite this, ameboid cells may indirectly mechano-sense, which may be necessary for tumor metastasis.

A common characteristic of ameboid models is that they highlight a specific aspect of migration based on the nature of their model. For example, cell membrane deformability—modeled as a system of springs—has been used to determine a cancer cell's migration speed through confined spaces[70], such as pores in a matrix. This model suggests that, but does not assess, stiffness gradients are able to drive a cells' direction of travel, but polarization in this model is simply defined to guide the cells through the obstacles and is not a result of it. The ECM playing only a passive role in influencing cell behavior is also observed in an earlier model from the study[7] by Lim *et al.* In this model, the cell has a permeable actin cortex inside an impermeable outer membrane, with adhesion points connecting the two. Cell movement occurs when membrane-cortex adhesions rupture, the outer membrane expands, and the actin cortex is pulled toward the rupture by a cytoplasmic pressure gradient; again, the matrix is only an obstacle and polarization is built in to the model rather than a result of it. From such models, neither mechanosensing nor migration from gradients has been considered.

Ameboid-like migration has been frequently observed in 1[98]- and three dimensions[99,100] when the environment requires less adhesive, confined migration distinct from mesenchymal modes. Despite not engaging traditional machinery, cancer cells in this mode and confinement do recognize substrate stiffness unlike the models mentioned previously, and it is observed that stiffer, confined spaces support more ameboid migration[26]. Thus, models that

highlight this behavior often consider possible ways that gradient sensing could occur in ameboid migration, either *de novo* or as a switch between models. For example, probabilistic models highlight that migration mode switching occurs in heterogenous matrix conditions and that both migration modes and plasticity are advantageous in heterogenous tumors because cells can sense their niche and switch modes as needed. Modulating the degree of cytoskeletal polymerization can also induce transitions[71] as observed by Niculescu *et al.* Simulated cells displayed ameboid blebbing or a spread lamellipodium and gliding behavior simply by changing maximum actin polymerization. Each mode fed back on itself, and so switching events were rare as in *in vitro* observations but were not dependent on local conditions, i.e., cell could not sense environmental changes.

All models discussed in this section portray a common trend and limitation of computational models used for ameboid migration: focus remains on processes within the cell rather than interactions between the cell and its environment. Even for the few models that incorporate interactions between migrating cells and their physical environment, they still simplified as they restrict the cell from taking some shape or prevent the membrane from expanding into the physical obstacle. Although an emerging part of the literature[100], mechanosensing in this mode should be validated so that we better understand the environmental conditions and gradients that could result in migrating cells switching between modes[1,2] and if ameboid migration could support adurotaxis as the mechanisms still remain to be elucidated (Figure 1.3). While these models are able to analyze how cells change the shape and what sized spaces they can fit through, thus providing information about the process of migration, they are limited in that they only account for one portion of complicated processes like tumor metastasis and adurotaxis.

1.5 *In Vitro* Tumor Models for Migration and Metastasis

Tumor models are designed to recapitulate the properties of the tumor microenvironment and provide an essential platform for understanding the progression and treatment of cancer *in vitro*. These tools serve a low-cost and high throughput alternative to screen for drug therapies compared to *in vivo* animals models[101], and contribute to our understanding of tumorigenesis in ways that may not be fully captured with just computational modeling. By recreating the unique properties of the tumor microenvironment, researchers can use these systems to identify and evaluate specific tumor pathways and cell behaviors involved in disease progression[102]. Advances in these models have also provided new insights into the critical steps of the metastatic cascade, including intravasation, extravasation, angiogenesis, matrix remodeling, and immune response[101,103]. These models vary in complexity from simple 2D cultures comprised of tumor-derived cell lines to bioprinted 3D structures incorporating multiple different cell types, each striving to recapitulate the key mechanical and biological functions of the tumor microenvironment. In this section, I will discuss how these *in vitro* models are engineered to recreate the properties of the tumor microenvironment, and then examine how they can be used to characterize the metastatic potential that arises from the biophysical properties of the cell and its environment.

1.5.1 Reproducing the tumor microenvironment for cell migration

The tumor microenvironment (TME) is a complex and heterogenous structure consisting of a variety of different cell types, including cancer associated fibroblasts (CAFs) and a variety of immune cells, that are surrounded by a 3D fibrillar extracellular matrix. CAFs are strong contributors to the construction of the TME[104], and with the help of tumor cells, stiffen the surrounding matrix via the secretion of collagen and other fibrillar proteins[84,85]. These natural

materials can be used to create 2D or 3D hydrogels that recreate a specific ECM composition

(Figure 1.4A). The stiffness, i.e., the Young's modulus, of these gels can be modulated by

adjusting the polymer concentration or crosslink density to match that of the TME (Figure 1.4B),

enabling cells in culture to respond in a similar manner to their natural environment. The

behavior of cancer cells is also affected by the architecture and topography of ECM fibers, and

invasion and metastasis can be induced by the degree of fiber alignment (Figure 1.4C).

Additionally, the porosity of the ECM can determine how effectively malignant and

nonmalignant cells move through the TME (Figure 1.4D), which is strongly dependent on the

size and stiffness of a cell's nucleus. Taken together, *in vitro* models that capture many of these

properties will be more relevant to understanding the cell behaviors that are induced by the TME.
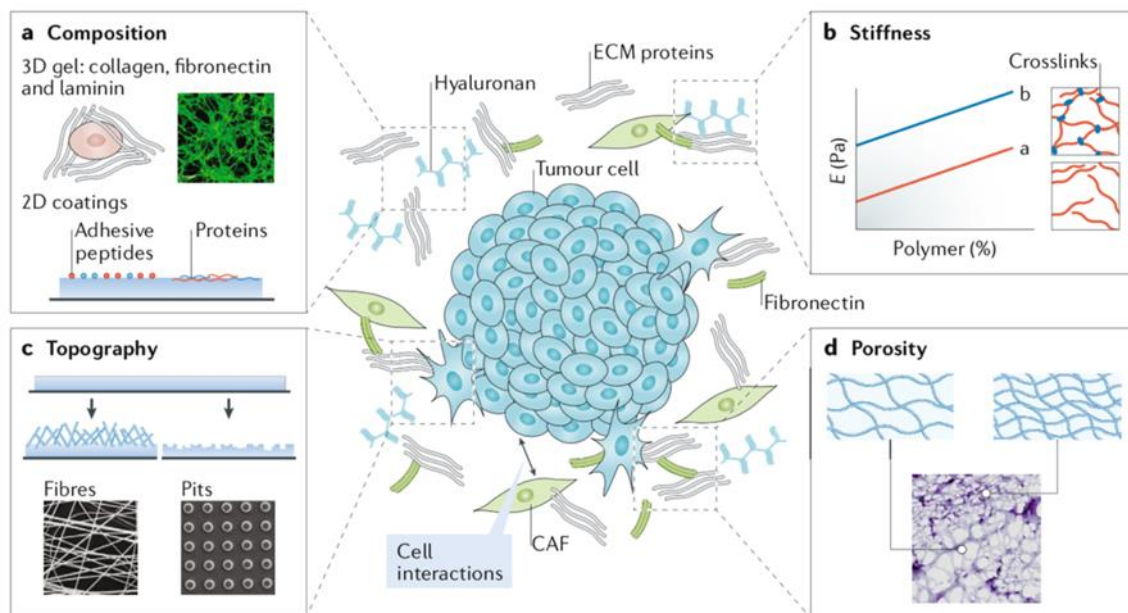
Figure is reproduced and modified with permission from ref.,[102]

Figure 1.4: Mechanical properties of the tumor microenvironment
(A) The composition of the ECM that makes up the TME can vary in ligand type and presentation. 2D hydrogels can be coated in these proteins, or 3D hydrogels comprised of them, to recreate a specific ECM composition. (B) Stiffness of the TME also effects cell behavior and can be modulated by adjusting polymer size and length to increase entanglements (line a) or crosslinking (line b). The stiffness, i.e., Young's modulus, is calculated by the stress in the material per cross-sectional area. (C) Topographical features can be fabricated by electro-spinning biocompatible polymer fibers onto a surface, or specific nano- or microtopographical features such as pits or channels can be etched into a material. (D) Modulating bulk polymer density or droplet size in emulsions allows for creating model TMEs with varying pore size and connectivity. CAF, cancer-associated fibroblast.

TME models can be used as 2D or 3D migration assays to assess the migratory potential of cancer cells. 2D migration assays are generally easier to produce, and are able to recreate important features of the TME such as ECM stiffness and ligand density[105,106]. Polyacrylamide hydrogels offer a simple way of tuning substrate stiffness, and photo-initiators allow for the use of photomasks to selectively stiffen regions as a means of interrogating the durotactic behavior of cells[105]. While these models are useful for analyzing a cell's response to a small number of variables, they do not necessarily faithfully behavior that would be seen in a 3D environment. Spheroid models utilize aggregates of cells that can either be grown in suspension or embedded in a 3D matrix comprised of various ECM proteins[101,107,108]. These models are useful for drug screening studies and in the case of embedded spheroids, studies of invasion, collective migration, and matrix remodeling[109–111]. 3D spheroid models better recapitulate the cell-cell and cell-ECM interactions that you would find *in vivo*, but require more advanced fabrication methods to model gradients in stiffness, ligand density, or chemotactic signals. New advances in 3D bioprinting have made it possible to spatially organize the matrix architecture by offering precise control over cell population and ECM deposition[112–114].

While it is important that these systems be designed to incorporate the mechanical and materials properties of the TME, they must also take into account requirements beyond just materials. Tumors often contain a variety of different cells types, including CAFs, endothelial cells, pericytes, and immune cells[102,103], and the vast majority of *in vitro* models lack some of this essential diversity. Immune-based cancer treatments often fail to treat solid tumors due to the physical and chemical barriers created in the TME by these cell types[103,115] A handful of microfluidic systems have been developed to include some of these interactions[116,117], that have begun to shed light on tumor-immune interactions that occur in the TME. As these technologies

mature, they will certainly offer new insights into the effects of the biophysical properties of the cell and its environment on tumor progression and metastasis.

1.5.2 Utilizing biophysical metrics for migratory and metastatic potential

Researchers have begun to look towards using the biophysical properties of a cell that allow them to escape from the TME of the primary tumor as a way of predicting metastatic potential. Because the cells must migrate through confined pores in the stromal ECM, which are often smaller than the nucleus of the cell, metastatic cells must be compliant enough to squeeze through them. Thus, cell deformability have emerged as invasive marker for aggressive cancer cells[118] and techniques developed to characterize this deformability *ex vivo*[119,120] (Figure 1.5A). Whole cell deformability can be measured using micropipette aspiration, optical stretching, or microfluidic confinement assays, or at the local scale using atomic force microscopy (AFM) to obtain the specific stiffness of the nucleus. Cell contractility may also play an important role in metastasis, and has been shown to increase with metastatic potential[121]. Traction force microscopy can be used to measure stresses generated by the cell by tracking fluorescent bead displacement as a cell pulls against an ECM coated hydrogel[122] (Figure 1.5B). Cell-ECM adhesion strength has been shown to be another important biophysical characteristic that correlates with metastatic potential, where cancer cells with a lower adhesion strength tend to be more metastatic[123]. Spinning disk assays or microfluidic parallel plate chambers can be used asses cell-ECM adhesion strength[124,125], by generating fluid shear stresses on cells that are adherent on ECM coated glass slides (Figure 1.5C). These biophysical properties tend to be more universal across cancers of different tissue origins, making them promising indicators for predicting metastatic potential for a broader range of cancers.
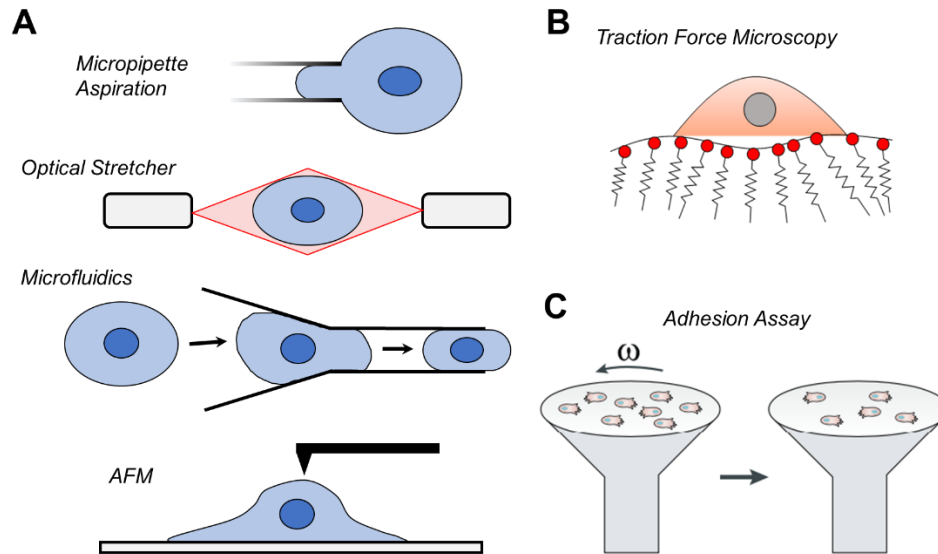
Figure 1.5: Biophysical markers emerging as metrics of metastatic potential
(A) Assays for measuring cell deformation. (B) Cell contractility can be measured using traction force microscopy. Stress generated by a cell can be calculated by measuring bead displacement in a substrate of known stiffness. (C) Spinning disk assay to measure cell-ECM adhesion strength. Shear stress experience by the cells increases as a function of radial position.

1.5.3 Early-stage detection technologies for cancer using biophysical parameters

Current standard of care for detecting cancers consists of regular screenings, such helical computed tomography scans for lung cancer, mammography for breast cancer, or colonoscopy, sigmoidoscopy, and stool tests for colon cancer. While these tests can be life-saving when they catch disease early enough, they offer a complete assessment of tumor state or expected patient outcomes. A relatively recent advancement in diagnosing the degree of cancer progression and metastasis has been the development of screens to detect circulating tumor cells (CTC) in the peripheral blood. Developments in biomaterial-based detection systems utilize the increased epithelial cell adhesion molecule (EPCAM) expression on the surface of CTCs to capture and enumerate the quantity of tumor cells circulating in the blood[126], with their presence correlating with a decreased progression-free survival and decreased overall survival. The main drawback to these screens however, is that by the time tumor cells are detectable in the bloodstream the cancer has already progressed to a dangerous degree.

Emerging technologies that utilize some of the biophysical properties of tumor cells collected from the primary tumor aim to better prognose metastatic risk prior to metastasis. Several studies have looked at how migration speeds, displacement, and persistence differ across multiple cancer lines[36,127], most notably one that used a microfluidic based platform to characterize a migratory signature predictive of metastatic potential[128]. While this device also required staining of Ki67 to assess cell proliferation rate, they were able to accurately predict which immortalized or patient-derived breast cancers would be highly aggressive or not, showing that cells isolated from a patient's primary tumor can reliably belie their metastatic risk. Another group used live-cell phenotypic-biomarkers and machine learning to stratify prostate cancer patients based on risk[129]. Although these tests have yet to receive FDA approval, they provide promising evidence that these biophysical traits can be useful for assessing metastatic risk.

Cell-ECM adhesion strength and the mechanisms that regulate it provide another physical metric to assess metastatic potential of cancer cells. A range of tools exist to measure the strength of these bonds, from single integrin-RGD ligand bonds measured via AFM[130], to whole cell-ECM interactions using fluidic shear assays[123–125]. These assays require a relatively small number of cancer cells, on the order of a few thousand cells, that can be collected from either the primary tumor or surrounding stroma. However, one major complication is that because tumor rarely consist primarily of cancer cells, patient biopsies will contain a variety of different cell types. Once advantage of using adhesion strength over other biophysical properties is that there is at least a 3-fold difference in adhesion strength between healthy and cancer cells[92,123]. This could provide a label-free metric to quantify the number of cancer cells that may have only locally invaded the surrounding stroma, and allow clinicians to assess metastatic risk

before these cancer cells reach the bloodstream.

1.6 Perspectives and Conclusions

The models discussed in this chapter show varying degrees of importance given to cells' mechanosensing capabilities and the effects of the ECM on migration. This is especially important to understand in cancer, where cells' ability to sense and migrate against a stiffness gradient may contribute to their ability to metastasize[38,42,43]. Due to the complex nature of cell migration and mechanosensing, computational models offer one of our best ways to understand and learn about migrating cell behavior. However, none of the models discussed consider all the variables involved in migration and to do so would likely be overcomplicated, computationally taxing, and, therefore, infeasible. Even the models that give extensive thought to the cells' physical environment do not consider cells' ability to switch between migration modes as other models do[26]. Beyond this, few models explore the cooperative or inhibitory migration behaviors arising from interactions between multiple cell types such as metastatic cancer cells, cancer-associated fibroblasts, and senescent tumor cells, which can all occupy neighboring spaces within the tumor microenvironment. Multicellular interactions can be extremely complex and can assist or hinder durotactic behavior through short- and long-range mechanical and chemical coupling[131–134]. No single modeling framework captures the complete breadth of these observations as far as we are aware. The current work on computational cell migration models has undoubtedly helped increase our knowledge of processes like cancer metastasis and migration in general to address the cancer cell migration paradox, but there are still many unanswered questions on how cell migration is guided by gradient sensing mechanisms illustrated in the paradox (Figure 1.3).

Improvements in *in vitro* tumor model systems have been useful for understanding many

of the cell and matrix mechanics used in the computational models discussed in this chapter. Experimental models provide a means to test and improve upon the theories created by the *in silico* simulations, which together highlight the essential drivers for cancer cell migration and metastasis. By designing computational and experimental models in parallel, we can improve our ability to recognize and assess the underlying physics of disease progression. Computational models can be used to quickly predict what are the key characteristics that affect a specific behavior, and guide the experimental design to effectively test these predictions. This knowledge can then be translated into diagnostic assays that utilize the keystone phenotypes that exist across multiple cancer types and are necessary for driving metastasis. As the genetic and molecular drivers for these phenotypes becomes better understood, both models can be used to generate potential therapeutic avenues towards treating cancer.

The scope of the research discussed in this dissertation encompasses the design and application of these types of models to describe how cells with a lower cell-ECM adhesion strength have increased metastatic potential. We will first characterize how differences in adhesion strength within an isogenic population of cancer cells allows the more weakly adherent subset to become more migratory. Then using both computational and *in vitro* models, how these differences allow these cells to migrate counter to typical durotactic behavior, allowing weakly adherent cells to migrate from the stiffer tumor ECM into the softer stroma. Finally, we will use a *in vivo* murine model to characterize differences in metastatic potential of weakly and strongly adherent breast cancer, and use a microfluidic parallel plate assay to measure the adhesion strength of the primary tumor and surrounding stroma of the injected cancer cells. The eventual goal is to use cell-ECM adhesion strength as a metric for metastatic potential in a clinical setting, and improve patient outcome by informing doctors on the best form of treatment.

1.7 Acknowledgements

Chapter 1, in part, is a reprint of the material as it appears in Shatkin, G., Yeoman, B., Birmingham, K., Katira, P., Enger, A.J. "Computational Models of Migration Modes Improve our Understanding of Metastasis" APL Bioengineering, 2020. 4: 041505. The dissertation author was a co-author of this paper.

CHAPTER 2. CELL ADHESIVENESS SERVES AS A

BIOPHYSICAL MARKER FOR METASTATIC POTENTIAL

2.1 Abstract

Tumors are heterogeneous and composed of cells with different dissemination abilities. Despite significant effort, there is no universal biological marker that serves as a metric for metastatic potential of solid tumors. Common to disseminating cells from such tumors, however, is the need to modulate their adhesion as they detach from the tumor and migrate through stroma to intravasate. Adhesion strength is heterogeneous even among cancer cells within a given population, and using a parallel plate flow chamber, we separated and sorted these populations into weakly and strongly adherent groups; when cultured under stromal conditions, this adhesion phenotype was stable over multiple days, sorting cycles, and common across all epithelial tumor lines investigated. Weakly adherent cells displayed increased migration in both two-dimensional and three-dimensional migration assays; this was maintained for several days in culture. Subpopulations did not show differences in expression of proteins involved in the focal adhesion complex but did exhibit intrinsic focal adhesion assembly as well as contractile differences that resulted from differential expression of genes involved in microtubules, cytoskeleton linkages, and motor activity. In human breast tumors, expression of genes associated with the weakly adherent population resulted in worse progression-free and disease-free intervals. These data suggest that adhesion strength could potentially serve as a stable marker for migration and metastatic potential within a given tumor population and that the fraction of weakly adherent cells present within a tumor could act as a physical marker for metastatic potential.

2.2 Introduction

The high mortality rate associated with cancer is due to metastasis from a primary tumor to a distal site[35,135]. Patient outcomes typically scale with rate of cell dissemination from the tumor, resulting in lower 5-year survival rates for aggressive tumors such as invasive ductal carcinoma[135]. However, determining cell dissemination rate from a tumor is difficult due to heterogeneity, that is cells in the same tumor have different propensities for forming secondary metastases[136–138]. Furthermore, there are no universal biochemical markers that predict metastatic potential across solid tumors[137,139]; next-generation assays that use these biomarkers typically only surveil cells post-intravasation.

Biophysical markers, such as cell deformability, are an emerging alternative to assess metastatic potential[102,118,140–143]. Assays based on these metrics focus largely on characterizing the physical properties of already circulating cells rather than understanding how cancer cells physically interact with and adhere to the extracellular matrix (ECM) at the onset of invasion. Given that all cancer cells must interact with the ECM to initiate metastasis, understanding variations in these interactions can serve as an early indicator of metastatic ability. For optimal cell migration into adjacent parenchyma, cells must turnover their focal adhesions (FA) to move through the tissue effectively; extremely unstable or stable adhesion can arrest migration as the cell can never establish contractile forces or unbind and retract rear portions of the cell[144]. Thus, migration speed is a function of the strength of attachment and is maximized when migrating cells can cycle their adhesions[144,145]. Indeed, invasive cancer cells have more dynamic FAs than their noninvasive counterparts[146], and decreased adhesion strength corresponds to increased metastatic potential[147]. As a result, the adhesion of cancer cells to ECM proteins is becoming an accepted metric for metastatic potential[148,149].

Many assays have been developed to demonstrate how adhesion differs in metastatic cells compared with their nonmetastatic counterparts[148,150–152]. However, such assays are either low throughput or not quantitative. It is also difficult to assess adhesive heterogeneity within a single cancer line using these methods[153]. We have previously demonstrated that metastatic breast cancer cells display lower cell-ECM adhesion strength than their nonmetastatic counterparts using a spinning-disk shear assay[123,154], especially when cells are exposed to an environment whose low cation concentration mirrors stroma[155,156]. We also observed an inherent heterogeneity in adhesion strength in multiple lineages including breast, prostate, and lung cancer cell lines[123]. Given this information, we developed a parallel plate flow chamber to isolate distinct fractions of cells from a heterogeneous population. Cells were isolated by applying a uniform shear stress to the cell population in the presence of stromal concentrations of Mg and Ca cations[155,156]. Within a given tumor line, we observed significant adhesion heterogeneity and found that the more weakly adherent fraction displays increased migration in both two dimension (2D) and three dimension (3D). This is due to the increased contractility and FA disassembly present in weakly adherent cells, resulting from transcriptomic expression differences in cytoskeletal components. Together, these data suggest that intrinsic differences in adhesion strength of cells within a population can act as markers of intratumoral heterogeneity in metastatic potential and be exploited to biophysically fractionate subpopulations.

2.3 Results

2.3.1 SA and WA phenotypes are maintained after sort

We fabricated a parallel plate flow chamber that exposes cells to discrete, uniform shear stresses to isolate fractions of cells based on adhesion strength, and study those cells within a heterogeneous population (Supplementary Figure S2.6). To ensure that the application of shear

did not change the adhesive heterogeneity of the population, we isolated weakly and strongly

adherent fractions of MDA-MB-231 cells from a parental cell population by exposing the cell to

a shear of 170 dynes/cm2 and stratifying the populations depending on whether they were found

in the flow-through or still attached to the device. After sorting, cells were cultured separately,

remixed, seeded into the device, and subsequently sheared. We found no significant changes

between the percent of WA and SA cells when tracking cells between days 0 and 2 (Figure

2.1A), indicating that the parallel plate shear device assesses, but does not alter, the inherent

adhesion heterogeneity of the population.
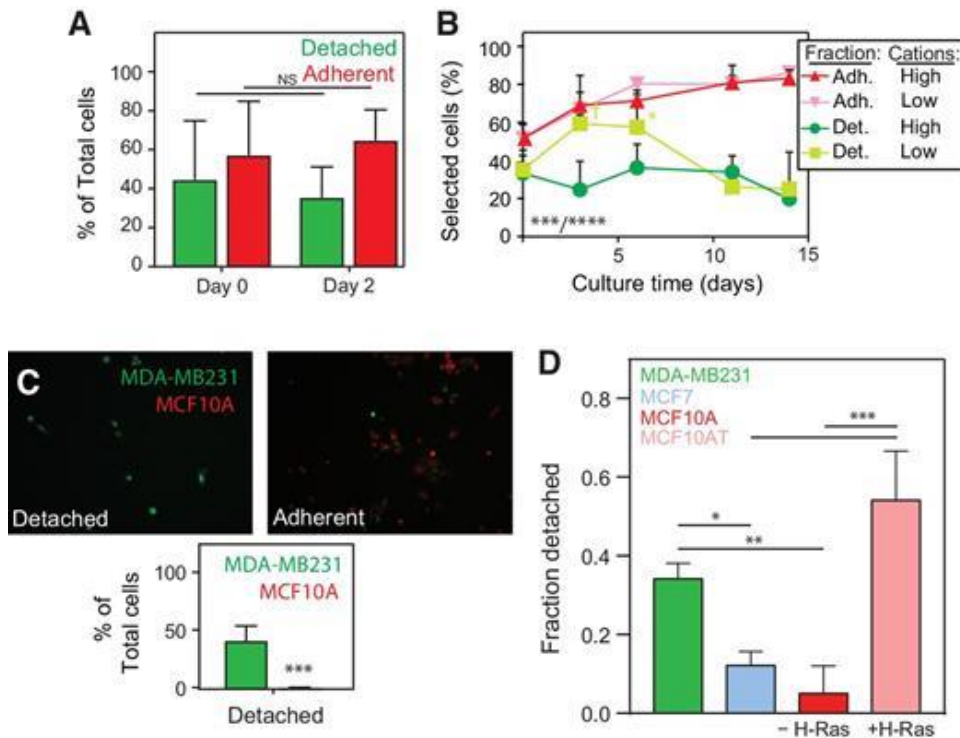
Figure 2.1: Low cation PPFC accurately and precisely sorts cancer cell populations that are stable long-term
(A) MDA-MB-231 populations were sorted at day 0, remixed, and then resorted at day 2. Differences between WA
and SA populations were assessed by two-tailed unpaired t test (n = 3). (B) Adherent cells post-sort were cultured in
high cations for 3, 6, 11, and 14 days and resorted. Cells that detached were cultured in high cations or low cations
mirroring stroma prior to resorting. Differences between WA and SA populations as a function of culture time and
condition were assessed by two-way ANOVA with Tukey test for multiple comparisons (n = 3). For time and
condition, ANOVA showed ***, $P < 0.001$ and ****, $P < 0.0001$, respectively as indicated at the corner of the plot.
Individual comparisons to their counterpart cation conditions are indicated in the plot with †, $P < 0.1$; *, $P < 0.05$.
(C) Images of cells from the flow-through (detached) and remaining on the plate (adherent) after exposure to shear
along with quantification of the percentage of cells that detached relative to plated cells from each line (n = 3). ***,
$P < 0.001$ for two-tailed unpaired t test between lines. (D) Plot showing the fraction of detached cells from MDA-
MB-231, MCF7, and MCF10A and their H-Ras–transformed counterparts MCF10AT after exposure to 250
dynes/cm2 of shear stress. NS, not significant.

We next wanted to determine if the adhesion phenotype is stably maintained post isolation. We isolated both fractions from MDA-MB-231 cells, cultured them separately in either normal or reduced cation media, and then repeated the isolation on the separated fractions. We found that strongly adherent cells maintained their adherent phenotype 14 days post isolation, regardless of culture conditions. Weakly adherent cells did not maintain their adhesion phenotype in normal culture media as cells reverted back to their distribution in the parental population; if the selection pressure of low stromal-like cation concentrations was maintained post isolation, weakly adherent cells were enriched to more than 70% of the population 6 days post isolation (Figure 2.1B).

2.3.2 Parallel plate flow chamber can distinguish between WA and SA cell lines

To test the ability of the flow chamber to select for cells known to have a weaker adhesion strength as a result their higher metastatic potential, MDA-MB-231 (metastatic breast cancer line) and MCF10A (nonmalignant breast cell line) cells were seeded in a 50:50 mixture and exposed to a shear stress that should detach the MDA-MB-231 cells but not the MCF10A cells (170 dynes/cm2 based on population adhesion assays[123]). The fraction of cells that detached contained 41.7% of the total number of MDA-MB-231 cells, whereas only 0.7% of the total number of MCF10A cells were present in the detached fraction (Figure 2.1C), consistent with 10-fold higher adhesion strength of MCF10A versus MDA-MB-231 cells in the absence of cations[123] and suggesting that this assay could distinguish metastatic cells from noncancerous cells.

To link quantitative adhesiveness to metastatic potential, we exposed four cell lines of varying metastatic potential (high metastatic capability: MDA-MB-231; low metastatic capability: MCF7 and MCF10A; and H-Ras transformed: MCF10AT, which give rise to invasive

carcinomas in vivo[157]) to 250 dynes/cm2 of shear stress and counted the fraction of detached

cells. As expected, cells with greater tumorigenic and/or metastatic potential had significantly

greater detachment at the same shear stress in comparison to cells with lower tumorigenic and/or

metastatic potential (Figure 2.1D).

2.3.3 WA cells display greater migratory propensity than SA cells

To assess migration differences in adhesion sorted populations, we isolated the ~2%

most weakly and most strongly adherent cells of the MDA-MB-231 population using 28 and 510

dynes/cm2, respectively and seeded them onto type I collagen gels. Over 24 hours post plating,

we found that WA cells displayed significantly higher average speed than the SA or unselected

(non-sheared) cells (Figure 2.2A). Weakly adherent cells also displayed increased total cell

displacement than the SA or unselected cells (Figure 2.2B; Supplemental Figure S2.7). Because

the adhesion phenotype appears stable, we investigated if migratory differences were stable. WA

and SA cells along with unselected population were imaged after selection, and then re-imaged 2

days later. No significant differences for any population were observed after selection or later

while the WA fraction maintained its increased migratory propensity (Figure 2.2C). The two

populations did not exhibit differential proliferation during migration assessments (Figure 2.2D),

suggesting that higher migration speeds for WA cells were not the result of proliferation

differences. In addition to sorting a metastatic population, we further demonstrated sorting

fidelity by directly comparing the ~2% most WA and SA of MCF10A and isogenic H-Ras

transformed MCF10AT cells. Post-sort on collagen gels, we observed that the WA fraction of

MCF10AT cells had increased migration speed and displacement relative to its strongly adherent

counterpart, whereas MCF10A cell fractions did not show differences (Supplemental Figure

S2.8). These data suggest that heterogeneity in migratory phenotype as a result of selection by

adhesion strength is only present in more aggressive cells with increased tumorigenic capability.
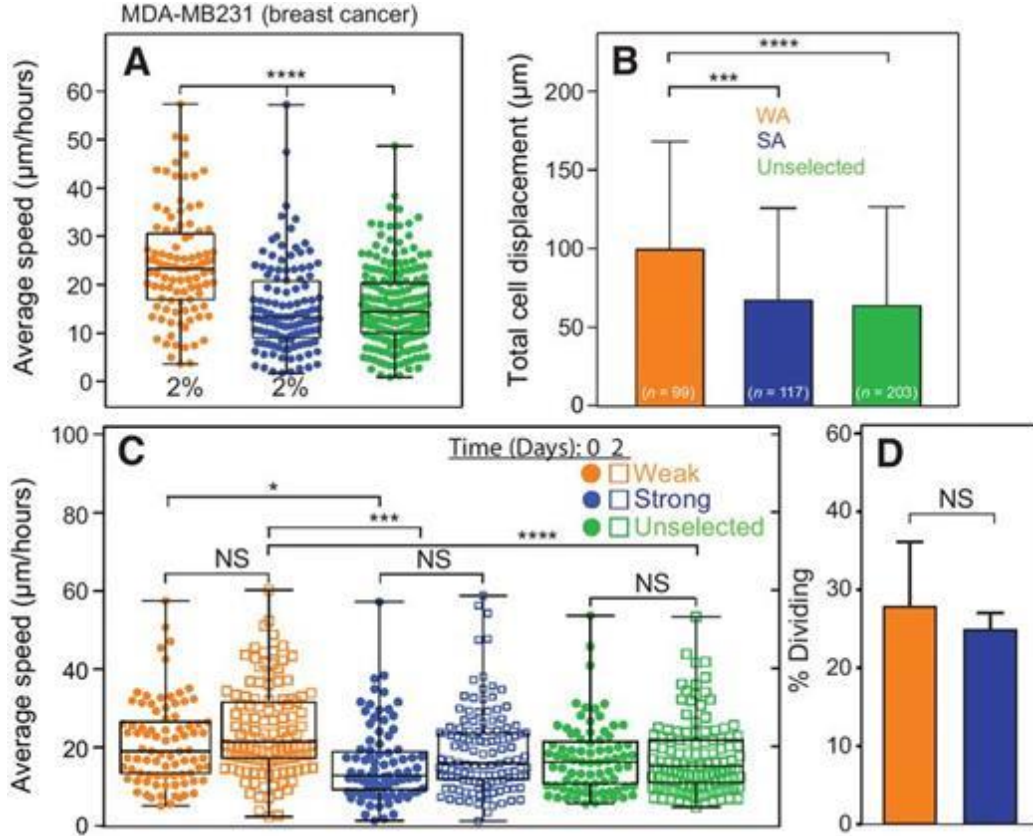
Figure 2.2: Sorted populations of single cells and spheroids exhibit and sustain different migration patterns.
(A) and (B), Average speed (A) and total displacement (B) were plotted for MDA-MB-231 cells sorted by the indicated shear stress and allowed to migrate on collagen gels for 24 hours. Percentages in A reflect the portion of each population that detaches or remains adherent at a given stress; n = 3 biological replicates for the number of cells per condition inset in the bars in B. (C) Average speed was measured after initial isolation and after 2 days, n = 3 biological replicates. (D) Plot showing the percentage of dividing cells on a collagen gel over 24 hours for cells selected by the indicated shear stress. n = 3 biological replicates.
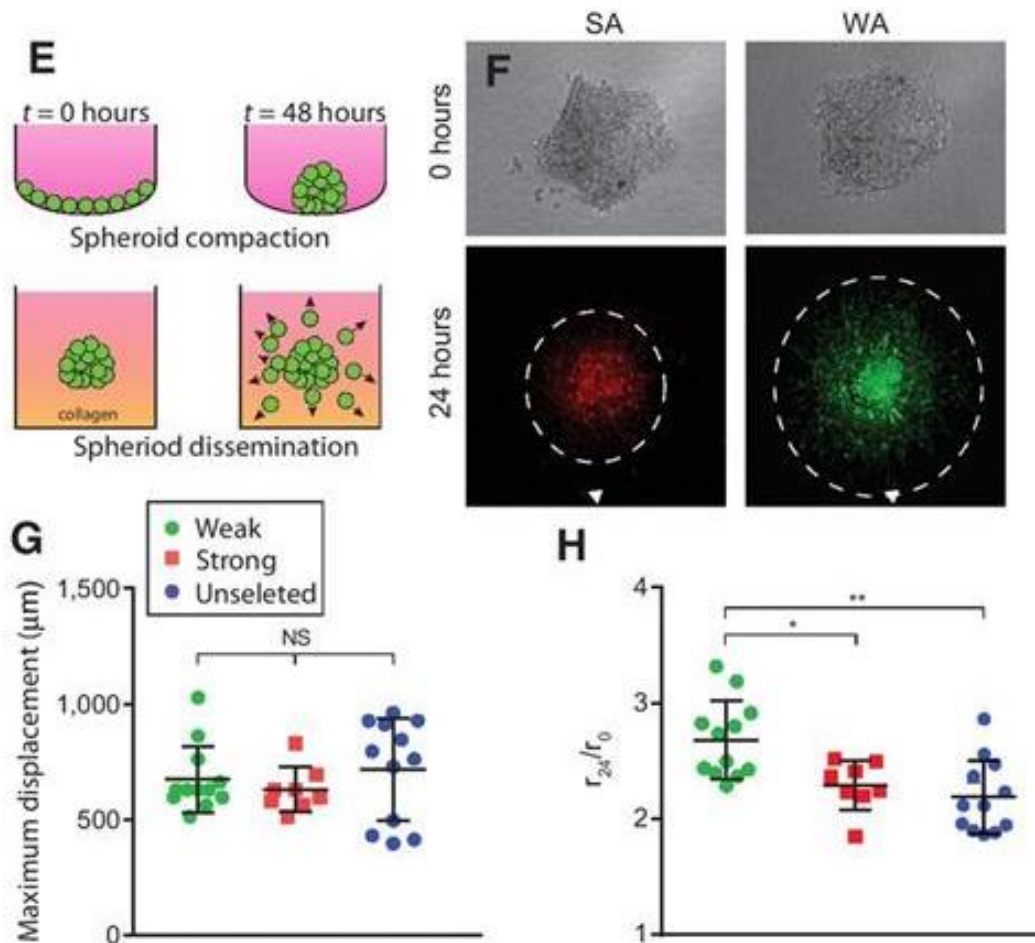
Figure 2.3:-Continued: Sorted populations of single cells and spheroids exhibit and sustain different migration patterns.
(E) Schematic of tumor spheroid formation (top) and subsequent dissemination (bottom) in a collagen
gel. (F) Brightfield images at the time of spheroid embedding in a collagen gel and fluorescent image 24 hours later.
Dashed line, average radius of disseminating cells. (G) and (H) Plots of maximum (G) and normalized (H) average
outward radial migration of cells selected by indicated shear (see Supplementary Fig. S5, for radius measurements).
One-way ANOVA with Tukey test for multiple comparisons was used to indicate significance, where *, $P < 0.05$;
**, $P < 0.01$; ***, $P < 0.001$; ***, $P < 0.0001$; NS, not significant.

Migration can often be affected by matrix properties, and so we sought to determine if

migration differences are intrinsic and therefore persist regardless of environmental changes that

could reduce substrate adhesion. WA and SA MDA-MB-231 cells were plated on

polyacrylamide gels of low (300 Pa) and high stiffness (1.8 kPa) and migration observed for 24

hours. WA cells were more migratory that the SA cells independent of substrate stiffness.

However, average speed scaled with substrate stiffness gel for both cell fractions, which indicates that both fractions are mechanically sensitive (Supplemental Figure S2.9). These results indicate that there are cell intrinsic differences independent of environmental changes that could potentially alter substrate adhesion.

Assays thus far show behaviors in 2D rather than 3D, so we next assessed the outward migration from spheroids containing WA, SA, or unselected cells (Figure 2.2E and F). There was no significant difference in maximum cell displacement (Figure 2.2G), but the leading edge of weakly adherent cells, that is the distance at which the signal is higher than background (Supplemental Figure S2.10), migrated further than SA and unselected cells, indicated by the significantly higher ratio of final radius to initial radius (Figure 2.2F and H). Consistent with 2D migration, these 3D spheroid data bolster the concept that the fraction of tumor cells with the WA most represents those with the highest metastatic potential.

All the cells examined thus far are mammary epithelial, so we next explored whether cells from other epithelial tumors would exhibit the same cation-dependent adhesion sorting and migration phenotype. WA and SA NCI-H1299 metastatic lung cancer cells were isolated and their migration analyzed. As with the metastatic mammary tumor line, WA metastatic lung cancer cells were more migratory than their SA counterparts (Supplemental Figure S2.11), suggesting that this behavior may be universal across epithelial tumors.

2.3.4 WA cells have more labile FAs and are more contractile

Migratory differences between WA and SA cells did not result from expression differences in FA proteins, for example pFAK, FAK, paxillin, or actin (Figure 2.3A). However, we previously found that metastatic cells preferentially disassemble their FAs relative to nonmetastatic cells when exposed to low cation conditions[123]. Consistent with this, we found that

the strongly adherent subpopulation of MDA-MB-231 cells did not fully disassemble FAs after removal of cations. Conversely, WA cells disassembled their FAs in the absence of cations on fibronectin (Figure 2.3B–D) or on type I collagen-coated substrates (Supplemental Figure S2.12). These data suggest that weak adhesion could be driven by differential sensitivity to cations and could therefore enhance migration. Similarly, cancer cells that exhibit increased contractility are also more migratory than their less contractile counterparts[121,158]. To ascertain if adhesive state is coupled with contractility differences, traction force microscopy was performed on cells post-sort. WA cells were significantly more contractile than their strongly adherent counterparts (Figure 2.3E and F), suggesting that weakly adherent cells represent a more aggressive fraction of the population.
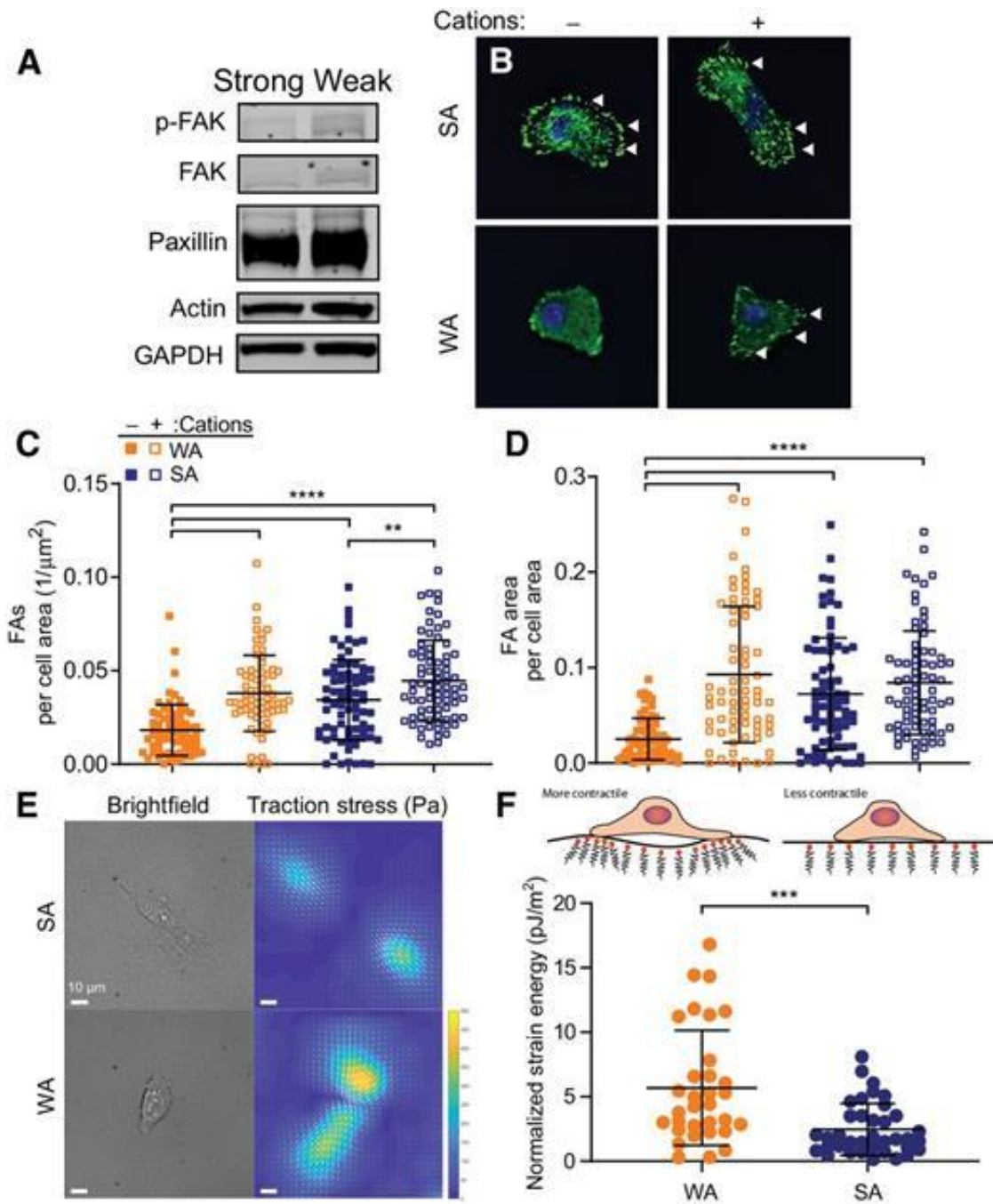
Figure 2.4: Adherent phenotypes within a cancer line result from intrinsic adhesion stability and contractility differences

(A) Comparison of the expression of common FA proteins in SA and WA cells. (B) Representative images of FAs in SA and WA cells when subjected to with or without cation conditions. (C) and (D) FA density (C) and total area per cell area (D) are plotted for the indicated sorting and cation conditions. n = 3 biological replicates and >50 cells/condition. One-way ANOVA, with Tukey multiple comparison test was performed for the indicated comparisons with **, $P < 0.01$; ***, $P < 0.001$; ****, $P < 0.0001$. (E) Brightfield and traction stress plots for cells from the indicated shear conditions. Scale bar, 10 μm. (F) Plot of normalized strain energy for WA and SA cells. n = 3 biological replicates and >30 cells/condition. A two-tailed unpaired t test between lines indicated **, $P < 0.01$; ***, $P < 0.001$; ****, $P < 0.0001$.

2.3.5 Intrinsic transcriptional variation in microtubule proteins contributes to increased migration of WA cells

Given that populations sorted at the less restrictive 170 dynes/cm2 still remain stable with over 1 to 2 weeks in culture, and cells sorted at the more restrictive 28 dynes/cm2 show cell intrinsic migration differences independent of environmental changes that are stable for days in culture, we next interrogated transcriptional differences underlying WA and SA phenotypes sorted at 28 dynes/cm2. Stability appears in part because individual populations do not out compete each other, that is cell proliferation rates appear similar (Supplementary Figure S2.13). With stable sorting and expansion, we sought to assess differences through post-sort RNA sequencing (RNA-seq). Analyses revealed 500 differentially expressed genes between the subpopulations (Figure 2.4A); replicates clustered by subpopulation when comparing differentially expressed genes (Figure 2.4B). Analysis of genes upregulated in weakly adherent cells demonstrated significant enrichment of gene ontology terms involved in microtubule and cytoskeletal organization and binding (Figure 2.4C). Genes in these categories with the most significant expression differences are involved in cytoskeletal components, specifically microtubule-associated proteins. For example, GAS2L3 has been implicated in linking microtubules and actin and results in increased FA turnover and migration; SYNE2 is also essential for nuclear-cytoskeletal mechano-transduction in invasion and cell contraction[159–161]. Components linking the cytoskeleton to the nuclear or plasma membranes were also implicated, for example AKAP9, which regulates microtubule movement and is highly expressed in highly metastatic cells[162,163] (Figure 2.4D). There was also significant enrichment in the expression of motor proteins, specifically those involved in vesicular transport along microtubules (KIF14, DYNC1H1) as well as in cytoskeletal contraction (MYO9A; Figure 2.4C and D). KIF14, in

particular, is a potent oncogene that is highly expressed in several cancers, particularly breast

cancer, and is linked to improved invasiveness and dynamically changing FAs[164,165]. Changes

detected through RNA-seq were validated by qPCR, which confirmed increased expression in

WA cells (Figure 2.4E).
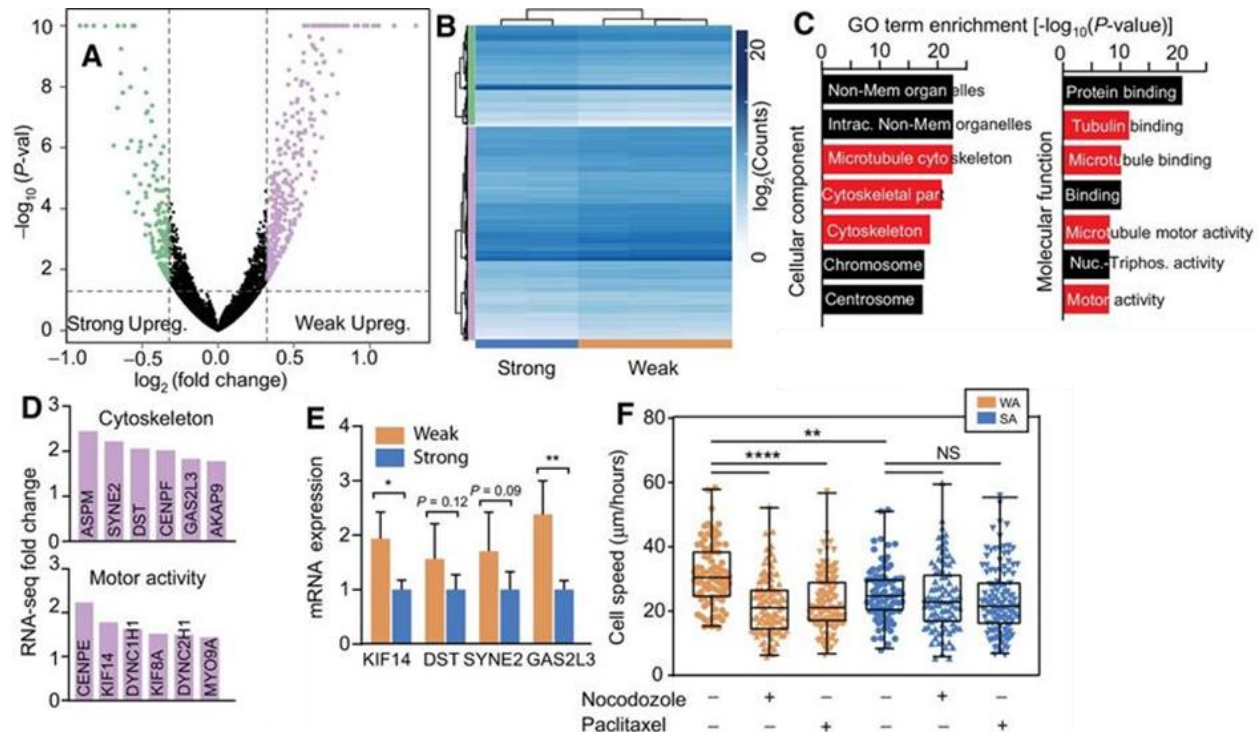
Figure 2.5: RNA-seq identifies intrinsic patterns that indicate structural rather than expression changes in adhesion

(A) Differences in gene expression between WA and SA MDA-MB-231 cells. (B) Hierarchical clustering of differentially expressed genes between WA and SA cells. Vertical bars indicate clustering of genes that are upregulated in SA cells and WA cells. (C) Gene ontology terms that are upregulated in the WA subpopulation. Cytoskeletal and microtubule gene ontology terms, as well as proteins that bind to these components, were significantly upregulated in WA cells. (D) Expressions of genes upregulated in cytoskeleton and motor activity, normalized to SA subpopulation. (E) Validation of RNA-seq gene expression differences via qPCR for select genes. *, $P < 0.05$ and **, $P < 0.01$ for two-tailed unpaired t test between WA and SA cells. (F) Average speed of WA and SA cells when treated with microtubule-targeting drugs. At identical concentrations of nocodazole (0.2 μg/mL) and paclitaxel (0.5 μg/mL), WA cells displayed a significant decrease in migration speed, whereas the SA cells demonstrated no change. One-way ANOVA with Tukey multiple comparison test was performed for the indicated comparisons with **, $P < 0.01$; ***, $P < 0.001$; and ****, $P < 0.0001$. NS, not significant.

To functionally confirm a link between the upregulated microtubule components in the

WA cells and their subsequent increased migration, we exposed both WA and SA cells to either

nocodazole or paclitaxel to dissemble or cap microtubules, respectively. When tracking

migration, untreated WA cells had increased average speed compared with untreated strongly adherent cells. However, when treated with either microtubule-targeting drugs, the WA cells exhibited a significant decrease in average speed, whereas the SA cells were unaffected (Figure 2.4F). These data suggest that inhibiting the microtubule cytoskeleton preferentially impacts the WA fraction and points to microtubule-affecting agents as potent therapeutic targets.

Finally, we investigated whether differentially expressed genes linked to the highlighted microtubule, cytoskeletal, and microtubule-binding protein ontology terms played a role in human cancer progression. We narrowed the list of genes down to those linked to our highlighted GO terms in Fig. 4C, resulting in 100 genes (Supplemental Table S2.2). Using this gene set, we then analyzed The Cancer Genome Atlas (TCGA) breast cancer dataset and restricted our analysis to patients with triple-negative breast cancer (TNBC) with tumors that ranged from stage I to III. We then compared patients who had gene expression scores that aligned with the SA and WA cells. We observed that patients with gene expression profiles similar to the WA cells had decreased progression-free intervals (Figure 2.5A) and disease-free intervals (Figure 2.5B) compared with patients with gene expression profiles similar to the SA cells. These data suggest that increased expression of genes associated with microtubule and microtubule-binding proteins, as present in the WA fraction, could define an "adhesive signature" that results in an increase in metastatic potential and promotes human breast tumor progression.
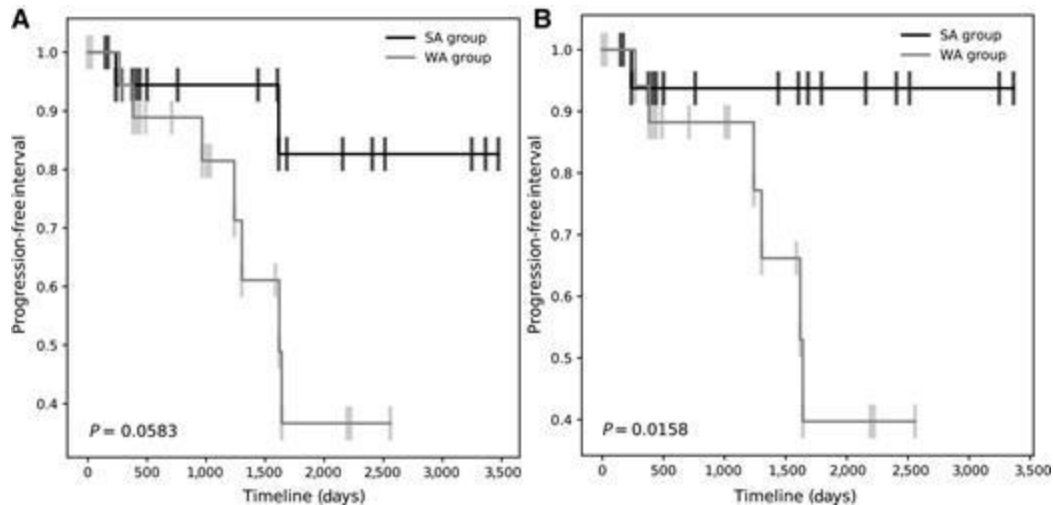
Figure 2.6: Expression of microtubule-associated genes resembling WA fraction predicts poor outcome in patients with breast cancer
(A) and (B) Progression-free interval (A) and disease-free interval (B) of patients with TNBC with stage I to III tumors. Patients with gene expression that resembled SA and WA cells were compared. Genes were restricted to those associated with highlighted gene ontology terms in Figure 2.4C, resulting in a cohort of 100 genes.

2.4 Discussion

Because of the highly heterogeneous nature of tumor cells, both within a given tumor as well as across tumors from different patients, it is difficult to assess tumor aggressiveness and the likelihood of metastasis. In addition, there are no universal biochemical markers that can be utilized to determine metastatic potential. The emergence of biophysical markers is a new approach to identifying the most aggressive subpopulations of the tumor population. Common cell–ECM interactions of early dissemination of cancer cells of different tumor origins and subsequent ECM deformation reflect the importance of identifying biophysical markers as metrics for metastatic potential[35,135]. To accomplish this, we utilized a parallel plate flow chamber to study the correlation between decreased adhesion strength of cells to ECM proteins and their subsequent metastatic potential. In conjunction with our previous studies[123], we showed that metastatic cancer cells are significantly less adherent than their nonmetastatic counterparts. This is demonstrated by the ability to select for MDA-MB-231 cells over MCF10A cells from a mixed population. We also found that WA can serve as a potential marker for metastatic

41

potential, which was demonstrated by the greater percent detachments of MDA-MB-231 and MCF10AT cells in comparison to MCF7 and MCF10A cells at the same shear stress.

This study also identified heterogeneity in adhesion strength of cells within a metastatic cancer cell population, especially under stromal-like cation conditions, which may be linked to heterogeneity in metastatic potential of cells within a tumor population and/or circulating tumor cells. This notion is supported by our observations that WA MDA-MB-231 cells exhibited increased migration in comparison to their strongly adherent counterparts. These differences in migration exist in both 2D and 3D environments, which indicates that the WA subpopulation represents the cells that are more likely to leave the primary tumor and establish secondary metastases[166–168]. The stability of this increased migratory propensity for multiple days post-sorting further demonstrates the intrinsic nature of this phenotype. In addition, recapitulating this phenotype in metastatic lung cancer cells suggests that adhesion strength is broadly involved in the more migratory subpopulations within tumors from multiple epithelial backgrounds.

The ability to select this more migratory subpopulation of the cell line stems from differences in FA disassembly between the WA and SA cells. Faster FA disassembly of WA cells is consistent with previous findings that link quicker FA disassembly to more migratory cell lines[146,169,170]. In addition, WA cells are more contractile than their SA counterparts, where increased contractility has also been linked to increased migration and more aggressive cancers[121,158]. Differences in migration, FA assembly, and contractility can be tied to inherent transcriptomic differences between WA and SA cells; genes linked to the cytoskeleton, specifically to microtubules, as well as motor proteins involved in vesicular transport and contraction showed significant differential expression. When we compared human patients with breast cancer with gene expression signatures that resembled the WA and SA cells for our genes

of interest, we observed decreased progression-free and disease-free intervals, implying that tumors resembling the WA fraction are more aggressive. Several standard cancer therapy drugs (nocodazole, taxols, etc.) target microtubules to reduce the growth and spread of aggressive tumors, indicating that differences in microtubules and the cytoskeleton could explain the heterogeneity of tumor cell populations. We confirmed these findings by treating WA cells to nocodazole and paclitaxel and found that their migration speed reduced to that of the SA cells, whose speed was unaffected by both drugs. Therefore, targeting the cytoskeleton is potentially an important method of restricting the motility of highly aggressive subpopulations early in tumor development and suppressing the migratory populations that we observe[171].

This study reveals a strategy to identify distinct subpopulations via shear separation that can be implemented to study the dissemination of cells from a variety of epithelial cancers. Comparing WA cell populations across multiple metastatic cell lines of various tumor origins could enable the identification of similarities among the most aggressive subpopulation in an effort to identify more universal targeted treatments. Finally, this shear assay can be adapted to study diseases with a similar adhesion component, highlighting the versatility of this technique.

2.5 Methods

2.5.1 Cell culture

MDA-MB-231 and MCF7 cells were cultured in DMEM, 10% FBS, and 1% antibiotic/antimycotic; MCF10A and MCF10AT cells were cultured in DMEM/F-12, 5% horse serum, 1% penicillin/streptomycin (Pen/Strep), 0.5 µg/mL hydrocortisone, 20 ng/mL hEGF, 10 µg/mL insulin, 100 ng/mL cholera toxin; NCI-H1299 cells were cultured in RPMI, 10% FBS, and 1% Pen/Strep. Products were purchased from Life Technologies. All cells were obtained from ATCC (authenticated by morphology, growth curve, and isoenzyme analysis), verified

Mycoplasma free via PCR, and were not used beyond passage 10.

2.5.2 Parallel plate shear assay

Glass plates (Brain Research Laboratories) were sonicated in 70% ethanol and water. Plates were coated with fibronectin at 2 µg/cm^2 for 60 minutes and then blocked with 5% BSA for 2 hours at 37°C. Plates are then seeded with cells at a density of 5,000 cells/cm^2 and incubated overnight. Components of the parallel plate shear assay (polysulfone base plate), 38-µm-thick silicone gasket (SMI), polypropylene luer fixtures (Cole Parmer), 1/8-inch inner diameter tubing (Thermo Fisher Scientific) were assembled and the glass plate was clamped to the base plate containing the inlet and outlet. The inlet tubing was connected to a syringe pump. Shear stress, τ, was calculated using the following equation:

$$\tau = \frac{6\mu Q}{wh^2} \tag{2.1}$$

where μ is viscosity of the fluid, Q is volumetric flow rate, w is the width of the chamber, and h is the height of the chamber.

2.5.3 Isolating weakly and strongly adherent cells

To test adhesion stability of weakly adherent (WA) and strongly adherent (SA) fractions of the population, we first determined an intermediate shear stress to detach roughly 40% of cells (~170 dynes/cm^2 for MDA-MB-231 cells). PBS without magnesium and calcium and with 4.5 g/L of dextrose was used to shear cells. Cells were subjected to the intermediate shear stress for 3 minutes to isolate WA cells in the flow-through, which was collected at the outlet. 0.25% trypsin-EDTA was added to the device to isolate SA cells. Once cells detached, media was pushed through the device to neutralize the trypsin and remove the SA cells. Both populations were then seeded.

To perform the adhesion stability remixed population assay, WA and SA cells were

isolated at day 0, cultured separately for 24 hours, re-mixed and seeded onto a plate overnight, then re-isolated at 48 hours after the initial isolation.

To isolate the weakest and strongest 2% of the MDA-MB-231 cell population for migration assays, the seeded plate was subjected to a low shear stress (28 dynes/cm^2) for 3 minutes to isolate WA cells in the flow through from the outlet. The shear stress was then increased to a high shear stress (510 dynes/cm^2) for 2 minutes to eliminate intermediate cell fractions. The remaining steps to isolate SA cells are listed above. The weakest MCF10A and MCF10AT cells were isolated using 170 and 130 dynes/cm^2 of shear stress, respectively; the strongest were isolated using 1,275 and 595 dynes/cm^2, respectively.

2.5.4 Coculture assay

MDA-MB-231 and MCF10A cells were trypsinized and resuspended in 25 μmol/L of CellTracker fluorescent probes (Molecular Probes, Life Technologies) in serum-free DMEM: MDA-MB-231 in green CMFDA and MCF10A in Orange CMRA. Cell-dye solutions were incubated at room temperature for 20 minutes. The cells were then centrifuged and resuspended in MDA-MB-231 media. Cells were mixed 50:50 and seeded such that the final seeding density was 5,000 cells/cm^2, then incubated overnight.

Upon isolation of WA and SA cells, both fractions were seeded, incubated overnight, then fixed the following day with 3.7% formaldehyde for 10 minutes. Cells were imaged using a Nikon Eclipse Ti-S microscope at ×10 magnification with FITC and Texas Red and counted by color.

2.5.5 Measuring percent detachment versus metastatic capability

MDA-MB-231, MCF7, MCF10A, and MCF10AT cells were subjected to 250 dynes/cm^2 of shear. The detached and adherent fractions were isolated as described and counted

to calculate the fraction of cells detached.

2.5.6 Immunofluorescence staining and FA analysis

Fixed cells were incubated for 10 minutes at room temperature with CellMask Deep Red plasma membrane stain (1:1,000; Thermo Fisher Scientific) in 1 mmol/L $MgCl_2$ solution, followed by incubation for 1 hour at room temperature with blocking solution of 10% goat serum, 0.1% saponin, 1% BSA, 0.03 M glycine in 1 mmol/L $MgCl_2$ solution. Primary paxillin antibody (1:250; ab32084; Abcam) in blocking solution was applied overnight at 4°C. Then, a secondary Alexa Fluor 488-conjugated antibody (1:2,000; Invitrogen) in blocking solution was applied for 1 hour at room temperature, followed by Hoechst 33342 (1:2,000; Invitrogen) in DI water for 10 minutes at room temperature. The cells were subsequently mounted with Fluoromount-G (Southern Biotech). The samples were imaged with a Zeiss LSM 780 confocal microscope (Zeiss) with a 63× oil-immersion objective. A custom-written ImageJ program was used to quantify cell area and FA number and size. All FA metrics were computed across the entire cell to avoid regional biases.

2.5.7 Traction force microscopy

Cell tractions were measured as described and calculated using a custom MATLAB routine[122]. 2% (v/v) of 0.2 μm diameter 580/605 FluoSpheres microspheres (Invitrogen) were added to the prepolymer solution, composed of 5% acrylamide, 0.06% bisacrylamide, 1% ammonium persulfate (Thermo Fisher Scientific), and 0.1% (v/v) of N,N,N',N'-tetramethylethylenediamine (VWR International). Gels were prepared in 12-well glass bottom plates (Cellvis), which were precleaned in a UV/Ozone cleaner (ProCleaner Plus; Bioforce Nanosciences) and methacrylated to ensure binding of the gel. Collagen was bound to the surface by adding 0.2 mg/mL sulfo-SANPAH and activating with UV light (wavelength 350 nm) for 10

minutes followed by incubation with 0.15 mg/mL type I collagen. Isolated cells were seeded at $\sim$15,000 cells/cm^2 on the gels and allowed to adhere for 3 hours. Brightfield images were taken of each cell prior to obtaining microsphere displacements at 60$\times$. Bead reference positions were then reobtained after removing the cells with a 10% (v/v) Triton X solution for 10 minutes. Strain energy was determined from the traction stress map and normalized to cell area.

2.5.8 Western blotting

WA and SA cells were isolated and plated in fibronectin-coated 12-well plates for 3 hours. Cells were lysed with mRIPA supplemented with phosphatase and protease inhibitors as described previously[172]. Protein concentration was measured using a BCA assay. Five micrograms of protein were mixed with 50 mmol/L DTT, loading buffer, and mRIPA, heated at 95°C for 5 minutes, and loaded into a Bolt 4% to 12% Bis-Tris Plus gel (Invitrogen) and then run with MES running buffer for 30 minutes at 200 V. Protein was transferred to a nitrocellulose membrane using an iBlot Cell Transfer Stack (Invitrogen). Membrane was blocked with 5% SeaBlock for 1 hour at room temperature then incubated overnight at 4°C with anti-paxillin (Abcam, ab32084), anti-pFAK (Y397; Abcam, ab81298), anti-FAK (Origene, TA506161), anti-actin (Abcam, ab8226), and anti-GAPDH (Abcam, ab8245). The membrane was then incubated for 2 hours at room temperature with Alexa Fluor 680 donkey antimouse (Life Technologies, A32788) and Alexa Fluor 790 donkey anti-rabbit (Life Technologies, A11374) antibodies. The membrane was imaged using a Li-Cor Odyssey CLx and analyzed using Image Studio Lite (Li-Cor).

2.5.9 2D migration assays on collagen gels

2.4 mg/mL type I collagen gels were prepared by mixing collagen (Corning) with PBS, DI water, and 1 M NaOH and adjusted to pH 7.0. Gels were added to a 12-well plate and cured

at 37°C for 30 minutes. The weakest and strongest 2% of the cell population were seeded onto the gels and incubated overnight. The cells were imaged with a Nikon Eclipse Ti-S microscope equipped with a temperature- and CO2-controlled stage. Cells were imaged at 10× in brightfield every 15 minutes for 24 hours. The migration data were analyzed via Fiji. The positions were normalized to the starting point and analyzed via a custom MATLAB script to compute instantaneous speed and cell displacement. Cells that divided or did not remain in the frame for 24 hours were not tracked. Cells that interacted with other cells for more than 2 hours were not tracked, as cell–cell interactions artificially slowed cell speed. For MDA-MB-231 cell migration under drug treatment, cells were treated with either 0.2 µg/mL nocodazole (Cayman Chemical) or 0.5 µg/mL paclitaxel (LC Laboratories). Cells were imaged the following day for 24 hours and tracked as stated above.

2.5.10 2D migration assays on polyacrylamide gels of varying stiffness

Polyacrylamide gels of low and high stiffness were prepared as described in the TFM methods section, without fluorescent microbeads. The high stiffness prepolymer solution has an identical composition to the gels used for TFM, whereas the low stiffness prepolymer solution consists of 3% acrylamide and 0.06% bisacrylamide with all other components identical to the high stiffness gel. Cells were isolated, seeded, and tracked as described previously.

2.5.11 Preparing spheroids of MDA-MB-231 cells

The weakest and strongest 2% of the MDA-MB-231 cell population and unselected cells were isolated and seeded in a 12-well plate overnight. Cells were trypsinized and resuspended in 25 µmol/L CellTracker fluorescent probes (Molecular Probes, Life Technologies) as described above. Cells were then centrifuged and resuspended in a solution of 0.25% Methocult in culture media. A total of 2,500 cells (either WA or SA) were added to wells in a 96-well Corning Ultra-

Low Attachment Spheroid Microplate (Corning) then incubated for 48 hours.

2.5.12 3D migration assays in collagen gels

Collagen gels were prepared as described previously. Spheroids were embedded in a collagen gel solution and added to a 24-well plate. Media was added to the top of the gel, and a time 0 image was captured at ×10 magnification with brightfield to obtain initial radius. Embedded spheroids were incubated for 24 hours, after which, they were fixed with 3.7% formaldehyde in solution A for 20 minutes. Spheroids were imaged with a Zeiss LSM 780 confocal microscope at ×10 magnification with the FITC and Texas Red channel. Z-stack images were acquired at 30 μm intervals from the bottom to the top of the spheroid. Maximum intensity projection images were generated and input into a custom Python script to analyze invasive index of spheroid and maximum displacement of cells in the spheroid. Invasive index is defined as:

$$I = \frac{r_{final}}{r_{initial}} \tag{2.2}$$

where $r_{initial}$ is the radius at time $t = 0$ hours of the spheroid and r_{final} is the radius at time $t = 24$ hours.

2.5.13 RNA sequencing

RNA from WA and SA cells was purified using Qiagen RNeasy Mini Kit (Qiagen, 74104). RNA quality was assessed using TapeStation (Agilent), RNA libraries were prepared using the Illumina TruSeq Stranded RNA, High Throughput Library Prep Kit and sequenced using the Illumina HiSeq 4000 system to generate 50 bp single-end reads. Data were analyzed by Rosalind (https://rosalind.onramp.bio/), with a HyperScale architecture developed by OnRamp BioInformatics, Inc. Reads were trimmed using cutadapt[173]. Quality scores were assessed using FastQC[174]. Reads were aligned to the Homo sapiens genome build hg19 using STAR[175].

Individual sample reads were quantified using HTseq[176] and normalized via relative log expression (RLE) using DESeq2 R library[177]. Read Distribution percentages, heatmaps, and sample plots were generated as part of the QC step using RSeQC[178]. DEseq2 was also used to calculate fold changes and P values. Clustering for the differentially expressed gene heatmap was done using the Partitioning Around Medoids method with the fpc R library[179]. Functional enrichment analysis of pathways, gene ontology, domain structure, and other ontologies was performed using HOMER[180]. Enrichment was calculated relative to a set of background genes relevant for the experiment.

2.5.14 qPCR

RNA from WA and SA cells was purified using Qiagen RNeasy Mini Kit and reverse transcribed using SuperScript III Reverse Transcriptase (Thermo Fisher Scientific, 18080093). Quantitative PCR was performed (45 cycles, 95°C for 15 seconds followed by 60°C for 1 min) using a 7900HT Fast Real-Time PCR System (Thermo Scientific, 4329001) with the primers listed (Supplementary Table S2.1), and iQ SYBR Green Supermix (Bio-Rad Laboratories, 1708880). Target genes were normalized to GAPDH and mRNA quantity was calculated on the basis of a standard curve generated from a fibronectin plasmid.

2.5.15 The cancer genome atlas dataset analysis

The Cancer Genome Atlas (TCGA) raw data were downloaded from NIH NCI GDC Data portal directly. Corresponding clinical metadata were obtained from a previous publication[181]. Only the patients with breast cancer (BRCA) with reported negative histological staining for the three markers (Her2, ER, PR) and American Joint Committee on Cancer (AJCC) pathology stages below stage IV were included in our analysis cohort. Patient data were analyzed to determine correlation between gene expression corresponding to WA or SA phenotypes and 5-

year survival. Patient data were analyzed by normalizing patient gene expression to z-transformed scores with respect to the differentially expressed genes between the WA and SA subpopulations. The z-scores were then summed for every patient, and z-score sum-based quantiles were mapped to SA and WA categories based on mean gene expression levels. The Kaplan–Meier method was used to create survival plots comparing the 20% of individuals with the lowest score to the 20% with the highest score. The log-rank test was used to determine significance of survival differences between groups. Survival analyses use the Lifelines python library (https://lifelines.readthedocs.io/en/latest/). Relevant scripts for the analysis of TCGA data are available at: https://github.com/kec162ucsd/Tumor-Heterogeneity-Adhesion-Strength/.

2.5.16 Statistical analysis

2D migration assays, 3D spheroid migration assays, and FA disassembly plots were analyzed using a one-way ANOVA with Tukey test for multiple comparisons. Adhesion stability remixed population assay was analyzed with a two-way ANOVA, with Sidak multiple comparison test. All other comparisons were performed using two-tailed unpaired t test unless otherwise indicated. For all analyses, *, $P < 0.05$; **, $P < 0.01$; ***, $P < 0.001$; and ****, $P < 0.0001$. Data expressed as box-and-whisker plots show all points with the whisker ends corresponding to minimum and maximum values. All other values are expressed as mean $\pm$ SD. Statistical analyses were performed using Prism software.

2.6 Supplementary Information
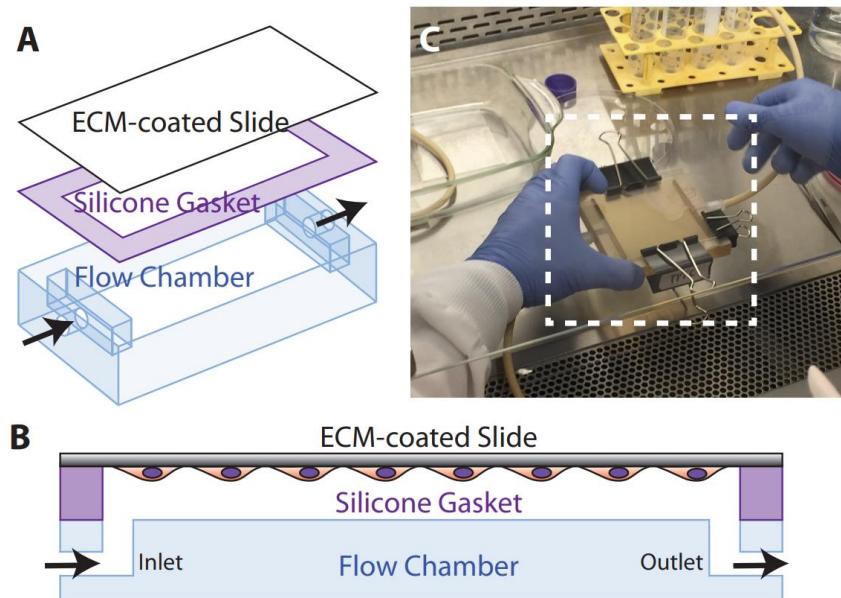
Supplemental Figure S2.7: PPFC Assembly and Use
(A) Exploded parts diagram of the flow chamber. Arrows indicate fluid direction. (B) Assembled cross-section schematic of the flow chamber with cell locations shown and fluid flow indicated. (C) Image of assembled flow chamber (dashed lines).
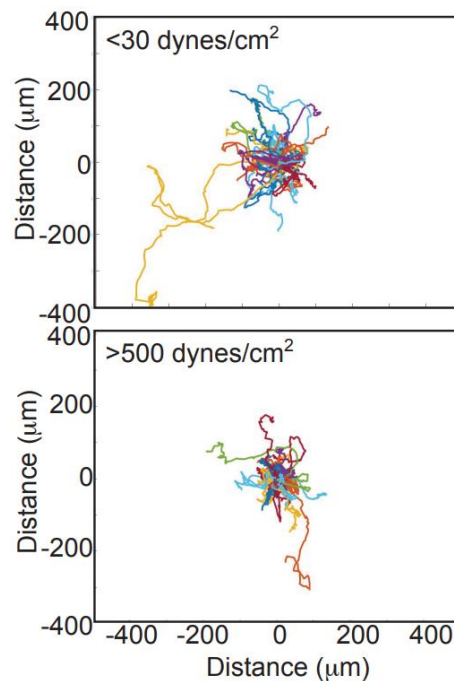
Supplemental Figure S2.8: Rose Plots of Post-Sort Cells
Rose plots of MDA-MB231 cells (each colored differently to visualize their paths) selected at 500 dynes/cm2. n=3 biological replicates and 250 cells/condition shown.
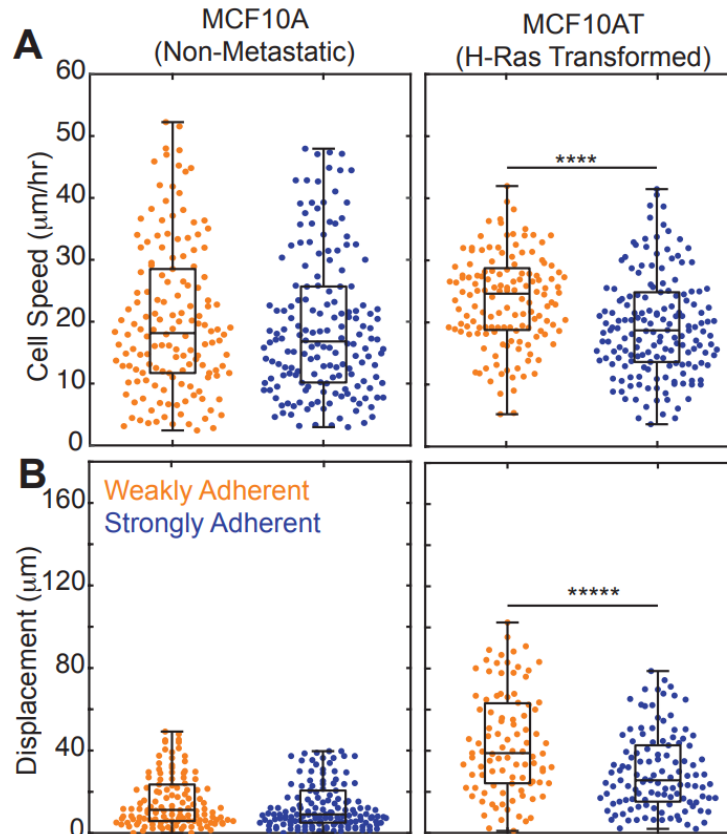
Supplemental Figure S2.9 : Migratory Differences in Isogenic MCF10A and MCF10AT Cells
(A) Average speed and (B) total displacement of MCF10A and MCF10AT cells sorted for the indicated fractions and allowed to migrate on collagen gels for 8 hours. n=3 biological replicates and >90 cells/condition. A two-tailed unpaired t-test between lines indicated ****p<0.00001.
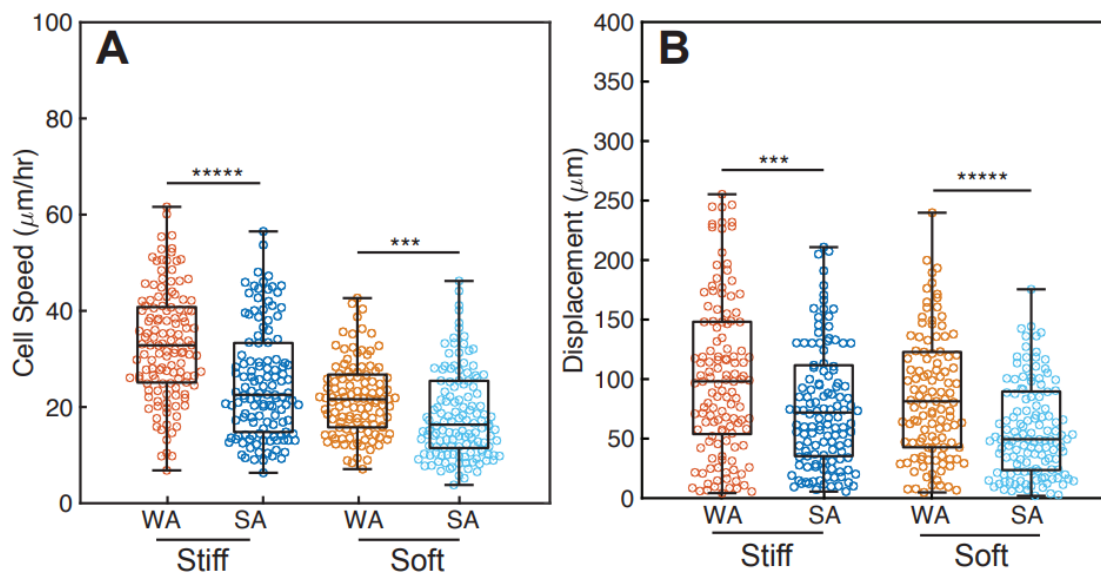
Supplemental Figure S2.10: Sorted Populations of MDA-MB231 Cells Display Migratory Differences Under Different Substrate Stiffnesses
(A) Average speed and (B) total displacement over 24 hours is plotted for MDA-MB231 weakly and strongly adherent cells on soft (300 Pa) and stiff (1.8 kPa) collagen-coated polyacrylamide gels. A two-tailed unpaired t-test between lines indicated ****p<0.00001.
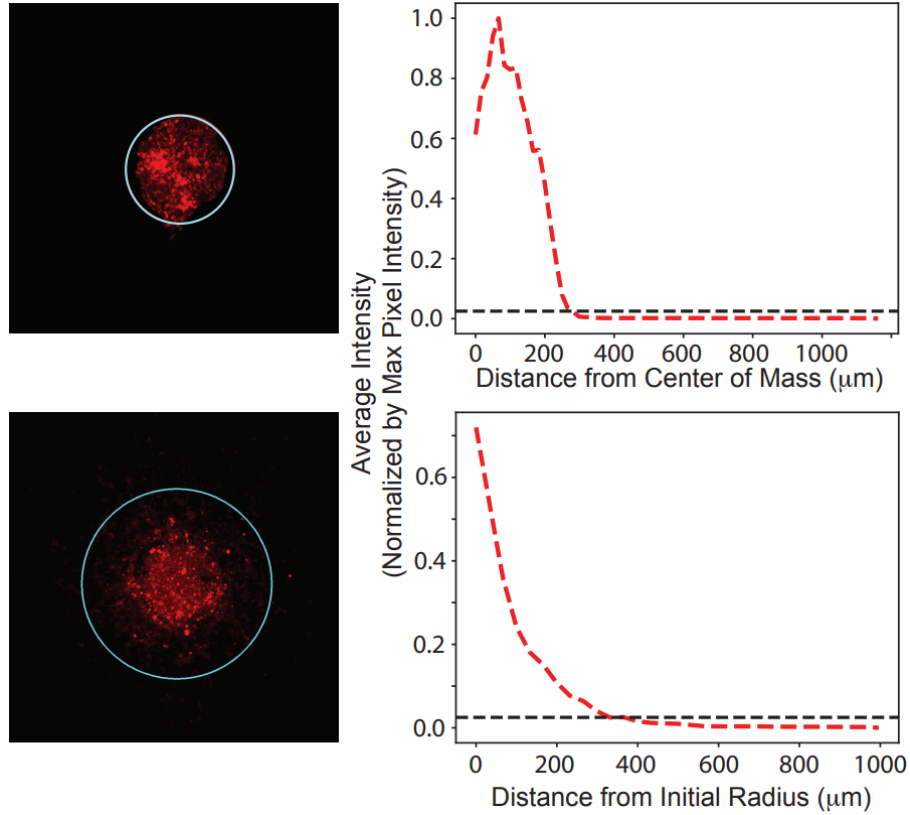
Supplemental Figure S2.11: Determining Spheroid Front

To automate the detection process for the leading edge of a spheroid embedded in and migrating through a collage gel, image analysis code was written to identify the radial intensity of the spheroid and surround matrix. When that line drops to within 2% of baseline, the average radius of the spheroid is calculated. The invasive ratio is then calculated. Examples of image used to determine the threshold for average radius (top) and the calculation of average radius after 24 hours (bottom) are displayed.
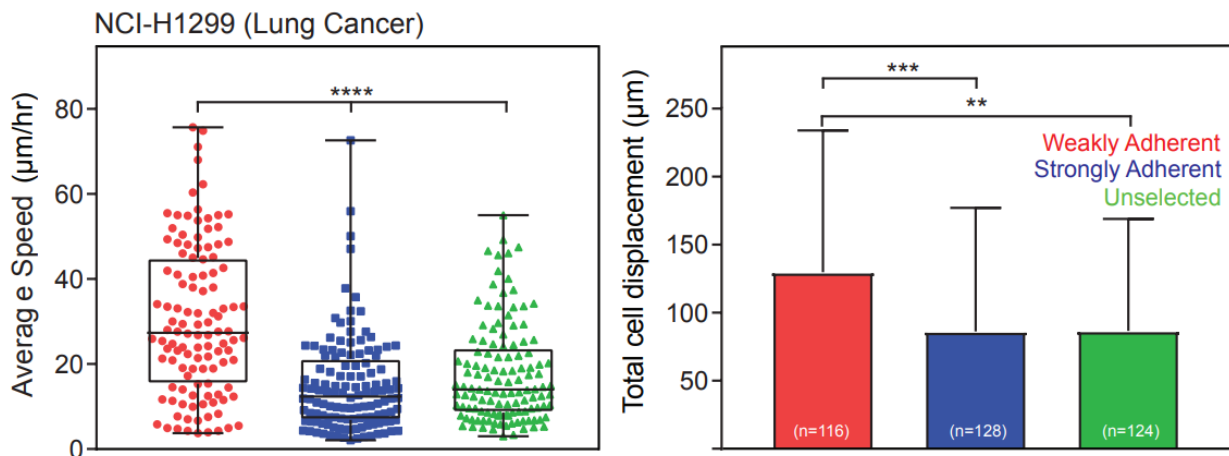
Supplemental Figure S2.12: Other Epithelial Cell Populations Exhibit Migration Differences Post-Sort

(A) Average speed and (B) total displacement is plotted for NCI-H1299 lung carcinoma cells sorted by the indicated shear stress and allowed to migrate on collagen gels for 24 hours. Percentages in panel A reflect the portion of each population that detaches or remains adherent at a given stress. n=3 biological replicates for the number of cells per condition inset in the bars in panel B. One-way ANOVA with Tukey test for multiple comparisons was used to indicate significance where **p<0.0001.
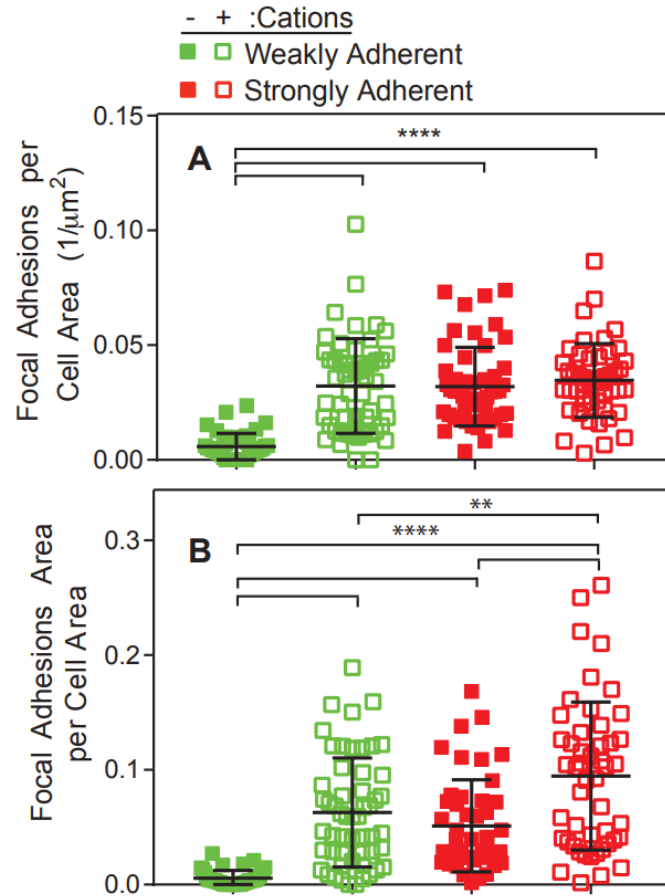
Supplemental Figure S2.13: Focal Adhesion Disassembly in Stromal Cation Conditions
(A) Focal adhesion density and (B) total area per cell area is plotted for the indicated sorting and cation conditions for MDA-MB231 cells cultured on collagen. n=3 biological replicates and >50 cells/condition. One-way ANOVA with Tukey's multiple comparison test was performed for the indicated comparisons with $**p<0.0001$.
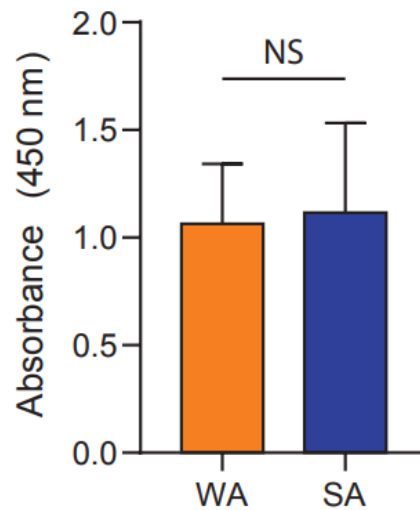
Supplemental Figure S2.14: Proliferation of Post-Sort Cells in not Different
BrdU absorbance is plotted for cells post sort.

Supplemental Table S2.1: qPCR Primers
Primer sequences for real time PCR.

Target Gene	Forward	Reverse
GAS2L3	AGCCTGCAATTCAAGTATGGTT	TGGTCCGTGTCTGGGAGTC
DST	GATCTTACAGCTCTGCCAGTGTGT	AGTAGCTTCTTTGGCATCATTGAA
KIF14	TGGTGAAATGGCCTGTACAAGT	GGCAACCAGTTAACCCTTTGAG
SYNE2	ACCACCCTATGGAAAGCTACT	CATCTCCCATCTGTCGAAGGC
GAPDH	TCGACAGTCAGCCGCATCTTC	ACCAAATCCGTTGACTCCGAC
Fibronectin (Standard)	AGGCTTGAACCAACCTACGGA	GCCTAAGCACTGGCACAACAG

Supplemental Table S2.2: Genes linked to highlighted GO terms that were used for TCGA analysis
List of all genes from the ontological terms in Figure 2.4 that were included in the TCGA analysis. Genes are shown in alphabetical order.

Gene Name	Gene Name	Gene Name	Gene Name
AHNAK	CEP350	KIF11	PEAK1
AKAP13	CEP97	KIF14	PLEKHH2
AKAP9	CKAP2	KIF18A	PLK2
ALMS1	CKAP5	KIF18B	PSRC1
APC	CNTRL	KIF20A	PTPN14
ASPM	DCLRE1B	KIF20B	RANBP2
ATM	DSP	KIF4A	RBBP6
BIRC6	DST	KNSTRN	RCSD1
BMF	DTL	KRT17	REEP4
BRCA2	DYNC1H1	KRT81	RIF1
BUB1B	DYNC2H1	MACF1	SAA1
CCDC88A	E2F1	MAP1B	SCLT1
CCNA1	ESPL1	MCM2	SETD2
CCNB1	FLG	MCM3	SH3PXD2A
CCNB2	FRMD6	MDN1	SLC7A11
CCNF	GAS2L3	MYH15	SPAG5
CDC25B	GEM	MYO5A	SPTBN1
CDC42BPA	GEN1	MYO9A	SYNE1
CDC42EP2	GPSM2	NAV1	SYNE2
CDC45	GTSE1	NDE1	TACC3
CDC6	HDAC4	NEK2	TOP2A
CENPE	HERC2	PAWR	TRIM59
CENPF	HMMR	PCNA	TTK
CENPJ	HTT	PCNT	UBR4
CEP192	KIAA0586	PDE4DIP	UTRN

2.7 Acknowledgments

Chapter 2, in full, is a reprint of the material as it appears in Beri, P., Popravko, A., Yeoman, B., Kumar, A., Chen, K., Hodzic, E., Chiang, A., Banisadr, A., Placone, J.K., Carter, H., Fraley, S.I., Katira, P., and Engler, A.J. "Cell Adhesiveness Serves as a Biophysical Marker for Metastatic Potential." Cancer Research, 2020. 80(4): 901-911. The dissertation author was a co-author of this paper.

CHAPTER 3. ADHESION STRENGTH AND CONTRACTILITY ENABLE METASTATIC CELLS TO BECOME ADUROTACTIC

3.1 Abstract

Significant changes in cell stiffness, contractility, and adhesion, i.e., mechanotype, are observed during a variety of biological processes. Whether cell mechanics merely change as a side effect of or driver for biological processes is still unclear. Here, we sort genotypically similar metastatic cancer cells into strongly adherent (SA) versus weakly adherent (WA) phenotypes to study how contractility and adhesion differences alter the ability of cells to sense and respond to gradients in material stiffness. We observe that SA cells migrate up a stiffness gradient, or durotax, while WA cells largely ignore the gradient, i.e., adurotax. Biophysical modeling and experimental validation suggest that differences in cell migration and durotaxis between weakly and strongly adherent cells are driven by differences in intra-cellular actomyosin activity. These results provide a direct relationship between cell phenotype and durotaxis and suggest how, unlike other senescent cells, metastatic cancer cells navigate against stiffness gradients.

3.2 Introduction

Durotaxis is a form of directional cell migration in which cells respond to and move toward extracellular regions of increasing stiffness[83,182]. Durotactic migration has been observed in a large number of migratory cells of mesenchymal lineage and is almost universally reported to occur in both 2D and 3D environments in the direction of increasing stiffness[182–184], with some speculation that it may occur in reverse[185,186]. While multi-que migrational responses may occur

in vivo[187], as the majority of tumors progress, their microenvironment gradually becomes stiffer than the surrounding stroma[42,188]. This suggests that the ability to move against stiffness gradients seems to be highly relevant at least in some cancers. Therefore, a breakdown in the normal processes regulating durotaxis may contribute to cancer cells developing different sensitivities to stiffness gradients leading to an increase in metastatic potential.

Several mechanisms have been proposed for the molecular basis of durotaxis[131,189], but how and when these molecular interactions are transduced into a directed force along or against a stiffness gradient is unclear. Computational and mathematical models have bridged gaps in our understanding of how cell mechanics and the microenvironment affect the speed, persistence[50,58,76,81,190,191], and emergent behaviors such as durotaxis[184,192–194]. However, a number of these models make additional a priori assumptions about how intra-cellular processes are differentially affected by stiffness in order to show durotactic behavior[195]. Additionally, co-occurrence of durotaxis, adurotaxis, or anti-durotaxis in similar cell populations, as might occur in metastatic tumors, is difficult to explain by current models.

We hypothesize that mechanotypic heterogeneity across and within cell populations might be responsible for differential durotactic behavior in these populations. In recent work, we found that adhesion strength acted as a physical marker that sorted isogenic cells into weakly and strongly adhesive cell groups that were more versus less contractile and migratory[92], respectively. RNA sequencing further showed transcriptional differences characteristic of distinct mechanotypes that sorted patient outcomes in The Cancer Genome Atlas (TCGA); patients with the weakly adhesive gene signatures relapsed at a rate 2-fold higher than the strongly adhesive gene signatures. Such differences could contribute to durotactic differences not previously observed, and here we show that mechanotypic differences are the proximate driver

for differential rigidity sensing and adurotactic behavior.

3.3 Results

3.3.1 Adhesion dynamics define an adurotactic phenotype

Here, we report that weakly adherent populations of various types of cancers cells are significantly less durotactic than their strongly adherent counterparts, potentially explaining how tumor cells migrate down stiffness gradients. Using the parallel plate flow chamber (PPFC)[92], cells are isolated based on adhesion strength and seeded onto photopatterned hydrogels with alternating soft and stiff elasticity profiles that match Young's moduli of softer stromal and stiffer tumor extracellular matrix (ECM) for each type of cancer (Figures 3.1A and 3.1B), i.e., 0.3 and 1.5 kPa for mammary[85,196], 4 and 20 kPa for lung[197–199], and 10 and 30 kPa for prostate[200–202]. When cells were plated on these gradients and observed by time-lapse video microscopy, we found that strongly adherent (SA) cells on average migrate significantly slower than their weakly adherent (WA) counterparts for mammary, lung, and prostate cancer cell lines (Figure 3.1C; Figure S3.5A) on stiff substrates, and slightly slower on softer substrates. Although slower, SA cells for each cell type were more likely to durotax and less likely to undergo adurotaxis than WA subpopulations (Figure 3.1D; Figure S3.5B); quantitatively, the durotactic odds ratio is calculated as the ratio of the odds that a SA cell is durotactic to the odds that a WA cells is durotactic. We found that this ratio was between 1.75 and 3 for durotaxis. Conversely for adurotaxis, that ratio was between 0.66 and 0.33 across all cell lines, which indicates that SA cells durotax and WA cells adurotax. Consistent with phenotype differences, we observe accumulation only of the SA cells over 24 h in culture on patterned substrates as SA cells moved from a random distribution to one biased toward stiffer regions (Figure 3.1E; Figure S3.5C). These behaviors again are largely conserved across cell lines from multiple tumor types,

60

albeit with varying degrees of effect such that accumulation is most robust for a mammary cell line. While the effects are the same, variability may be due in part to inherent mechanotype differences. For example, cells sort into WA and SA subpopulations at different shear stress in the PPFC; lung tumor cells are less adherent overall with the SA fraction sorting at >180 dynes/cm2, while prostate and mammary lines require >500 dynes/cm2 to sort their SA fraction.
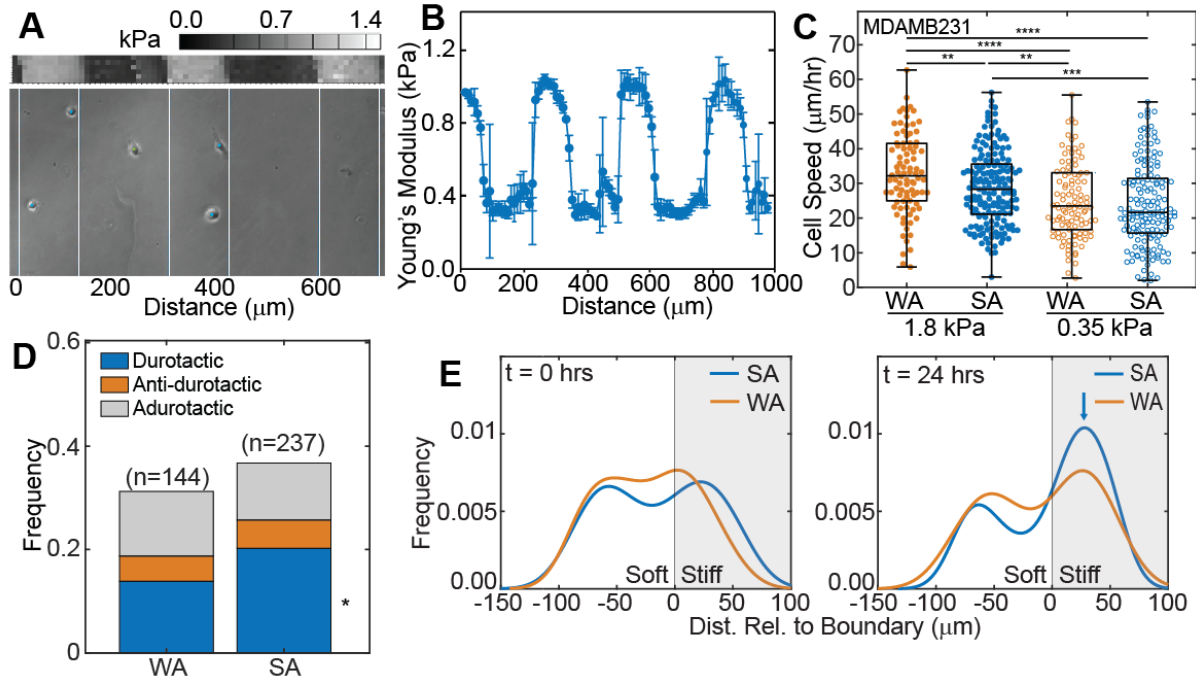
Figure 3.1: Weakly adherent cells exhibit higher adurotactic behavior
A) Bright-field image of cells (dots) with lines to indicate transitions between soft and stiff substrate regions of step-gradient hydrogels (bottom). Double-headed arrows indicate the distance relative to the closest gradient or boundary. Atomic force microscopy (AFM) map is also shown (center) with corresponding color map (top). Position is indicated in micrometers. (B) Plot of average substrate stiffness versus position for step-gradient hydrogels (n > 3). Error bars represent standard deviation. (C) MDA-MB-231 cell speed on soft or stiff side of step-gradient hydrogels is plotted. Data are shown for cells sorted by adhesion strength, i.e., weakly (orange) versus strongly (blue), and cells on softer (open) versus stiffer (closed) regions. (n > 144 cells for each condition from triplicate experiments). $*p < 0.05$, $***p < 10^{-3}$, $****p < 10^{-4}$ were determined by one-way ANOVA with Tukey test for multiple comparisons for the indicated comparisons. (D) For adhesion-sorted MDA-MB-231 cells that encounter the step gradient, the fraction of durotactic, anti-durotactic, and adurotactic behavior is plotted. Data represent n = 45 of 144 WA cells and 88 of 237 cells that crossed the gradient over triplicate experiments. Comparisons made using a Fisher's exact test for the same migration behavior between WA and SA cells, $*p < 0.05$. (E) At 0 and 24 h, probability density function of MDA-MB-231 cell distribution (calculated using the unbounded kernel density function) versus hydrogel position is shown for weakly (orange) versus strongly (blue) adherent cells from triplicate experiments. The stiffer region is shaded in gray. Blue arrow indicates a peak in the strongly adherent cell distribution at 24 h.

To understand what gives rise to mechanotype, we first measured traction forces across adhesion-sorted cell lines. We found that weakly adherent tumor cells exhibit higher traction

forces—measured for prostate cell lines on both single modulus soft and stiff substrates (Figure S3.6A) and for mammary cell lines on single modulus stiff substrates mimicking their fibrotic niche (Figure 3.2A); the lung cell lines were generally less adherent, and thus we did not observe significant traction differences (Figure S3.6A). This general trend, however, may appear counterintuitive: first, that weakly adherent cells generate stronger forces, and second, that cells generating stronger forces show decreased durotaxis and increased adurotaxis. We note that, as WA cells approached the gradient from either side, their velocities are dependent on distance to the boundary irrespective of the side they are approaching from, while SA cell speed generally increases moving from softer to stiffer substrates (Figure S3.6B). This suggests possible traction force redistribution along the cell length for the WA cells as they move across the stiffness gradient. We also noted that focal adhesion sizes were stiffness dependent for SA cells, while focal adhesion sizes for WA were the similar on either stiffness (Figures S3.7A and S3.7B). These observations suggest that adurotaxis could arise from a lack of change in balance between adhesion dynamics, redistribution of traction forces across the stiffness gradient, or both. Conversely, what does not appear to regulate durotaxis are differences in cytokine expression; blotting of 105 cytokines showed only 4 that were expressed above background and none were differentially expressed (Figure S3.7C).
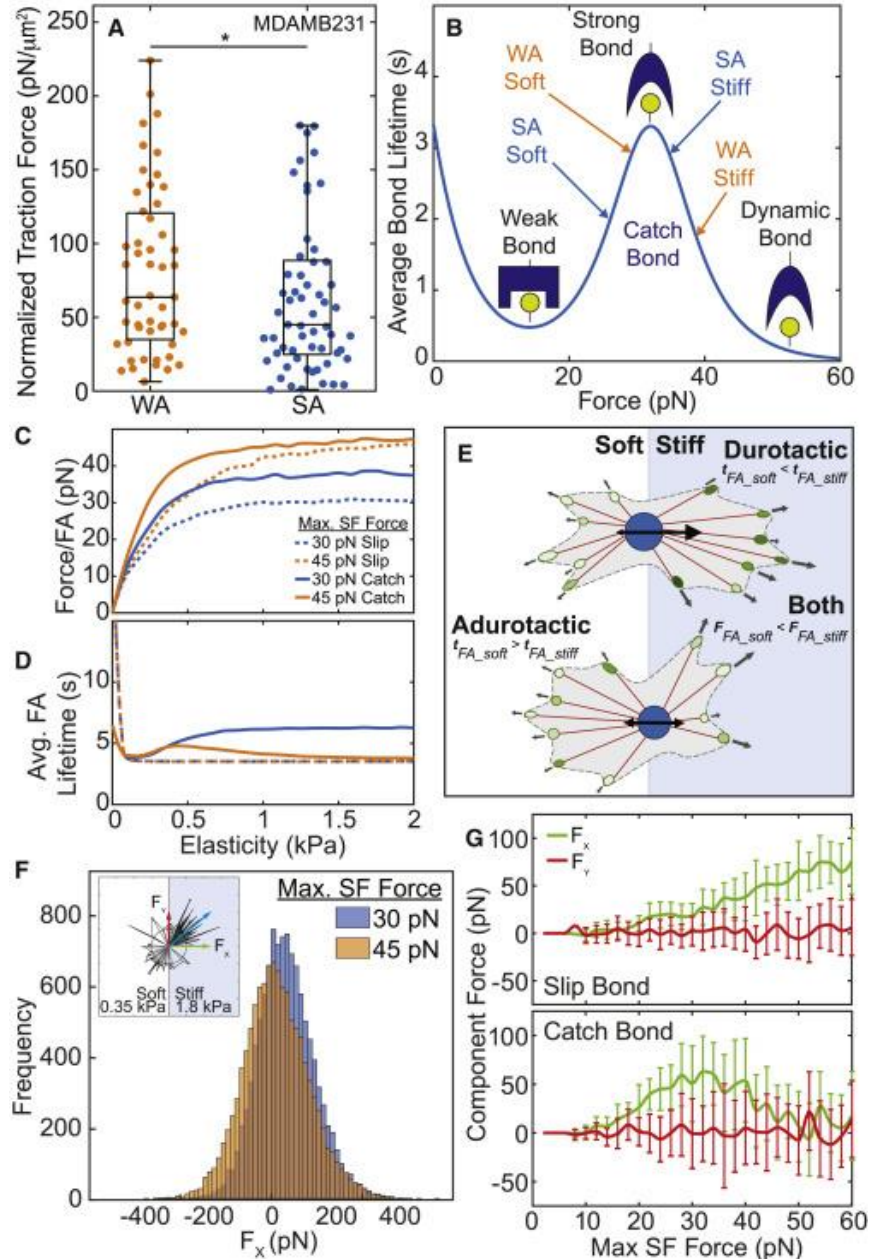
Figure 3.2: Higher forces on catch bonds leads to adurotactic behavior
(A) Traction force, normalized to cell area, is plotted for MDA-MB-231 cells on single-modulus hydrogels. Data are shown for weakly (orange) versus strongly (blue) adherent cells, (n > 50). *p < 0.05 was determined by one-way ANOVA with Tukey test for multiple comparisons. (B) Schematic of bond lifetime versus force with bond states for weakly (orange) versus strongly (blue) adherent cells as used in the computational model. (C) Force/FA versus substrate elasticity for catch (solid lines) and slip bonds (dashed lines) comparing 30 pN max SF force (blue) and 45 pN max SF force (orange), predicted by computational model. (D) Average FA lifetime plotted versus substrate elasticity for the same simulations. (E) Schematic of cells migrating over a step gradient. For durotactic cells, higher tractions and longer bond lifetimes on the stiff side drive adhesion maturation and net migration toward the stiffer substrate. For adurotactic cells, tractions balance across the boundary due to longer bond lifetimes on the soft side of the step gradient. (F) Histogram of all X component forces simulated over 1 h for a cell fixed at a step gradient, comparing 30 pN max SF force (blue) and 45 pN max SF force (orange). Inset shows model cell with protruding stress fibers and X component force (green arrow), Y component force (red arrow), and resultant force (blue arrow). (G) X and Y component forces versus max SF force for slip bonds (top) and catch bonds (bottom) from the computational model. Colors match the arrows in inset for Figure 3.2E. Error bars represent standard deviation.

63

To test the above suggestions, we employed a focal adhesion maturation and traction force generation model dependent on catch bond dynamics between cell-adhesion proteins and the substrate (Figure 3.2B). In this model, polymerizing actin fibers bind to substrate bound adhesion proteins, mature into actin-myosin stress fibers (SFs) and focal adhesions (FAs), and generate traction forces between the cell and the substrate. The focal adhesions grow/shrink via addition/dissociation of individual integrin-substrate bonds and SF recruitment in a force-dependent manner. Stress fibers are limited by the maximum force that each one can generate, i.e., max SF force, and ideally corresponds to the myosin stall force of collectively contracting heads against the actin stress fiber; max SF force is reached exponentially as the stress fiber pulls against the substrate[51]. The substrate stiffness in this model controls the rate of force increase in the stress fibers (Equation 3.5), which in turn alters the force generated in each stress fiber dependent on the associated integrin-substrate adhesion lifetime. The forces driving cell migration are obtained by vectorially summing forces in all the FA bound SFs within the cell at any given instant. Using this model, we compared the effect of integrin catch and slip bonds dynamics[43] on the force per adhesion and on focal adhesion lifetimes as a function of substrate stiffness for cells with different max SF force (assigned from prior observations of SF force[51]). As a function of substrate stiffness, both catch and slip bonds show increased force per focal adhesion, with catch bonds generating and sustaining higher forces due to bond strengthening and recruitment of secondary stress fibers (Figure 3.2C). For focal adhesion lifetimes, lifetimes with slip bond dynamics remained constant across relevant substrate stiffness. For catch bonds, however, lower max SF forces saturated focal adhesion lifetimes at higher values whereas higher max SF forces exhibit a small peak near normal mammary stiffness and then drop to saturate at a lower value at higher stiffnesses (Figure 3.2D). These data suggest that max SF force and

stiffness-dependent values for FA lifetimes optimize cell-migration forces for a given mechanotype. To test the predicted changes in adhesion lifetimes based on substrate stiffness, we applied a range of shear stress to cells cultured on substrates resembling normal and pathological mammary stiffness using a population-based adhesion assay[203]. We found that cells selected on glass as weakly but not strongly adherent could modulate their average adhesion strength and become more adherent in softer conditions (Figure S3.7D). These results align with model predictions based on catch-bond dynamics between the cell-adhesion receptors and the substrate (solid lines in Figure 3.2D). Since average FA lifetime is more substrate stiffness sensitive for weakly adherent cells and identical to strongly adherent cells on softer substrates, these data suggest that weakly adherent cells are less adherent and primed to migrate on stiffer substrates with lower FA lifetimes. These correlations will next be explored in a cell-based model to understand mechanotype mechanisms.

3.3.2 Actomyosin contractility defines adhesion phenotype and explains migration behavior

In this model framework (Figures S3.8A and S3.8B), we compared a range of max SF forces, finding that 30 pN indeed corresponds to peak bond lifetime at high substrate stiffness but that at higher max SF force, softer substrates experience longer bond lifetimes. We also found monotonically increasing force per adhesion for catch bonds, consistent with higher traction forces seen experimentally in WA cells (Figure 3.2A). Bond lifetimes were insensitive to stiffness for slip bonds, while force per adhesion increased monotonically as with catch bonds (Figure S3.8C). The relationship between average bond lifetime and substrate elasticity suggests that by increasing max SF force, a scenario could arise in which a cell's catch bonds are more stable adhesions on a softer substrate (Figure 3.2E). Stress fibers attached to those adhesion sites would have more time to pull a WA cell in the direction of the softer substrate, balancing

numerous shorter-lived forces in focal adhesions on the stiffer region. To illustrate this, we fixed

a cell at the step gradient interface and measured force generated parallel (F_x) and perpendicular

(F_y) to the gradient. On average, cells with 30 pN max SF force had a positive Fx, indicating that

the overall force on the cell is pulling it toward the stiffer substrate, whereas cells with 45 pN

max SF force had neutral F_x, suggesting the cell would behave adurotactically (Figure 3.2F).

This scenario requires cell-surface adhesions to behave as catch bonds, which appears

reasonable[130,204,205]. We would also note that when slip bond dynamics are used, it results in cells

with higher max SF force to durotax (Figure 3.2G), which would be at odds with experimental

results where WA cells are more contractile but less durotactic than SA cells.

     The main input required for this model is the max SF force of the WA and SA mammary

cells, but with this difference cell-migration speeds and traction forces match experimental

observations with the small exception of migration speeds of SA cells on soft substrates, which

go up slightly according to the model (Figures 3.3A and 3.3B). While a fine tuning of other

model parameters can fix the disparity, we focus only on the effect of max SF force here and

maintain other parameter values at those commonly found in literature. Additionally, just this

difference in max SF force enables the model to correctly predict durotactic differences (Figure

3.3C) and the accumulation of SA cells on stiffer substrates versus uniform distribution of WA

cells across the gradient over 24 h for mammary cells (Figure 3.3D). Importantly, when substrate

stiffness is altered to resemble the prostate cancer stiffness gradient[200–202], mammary cell

parameters (Table S3.1) cause SA cells to not durotax (Figure S3.8D). However, when substrate

stiffness range is maintained, i.e., 0.35 to 1.8 kPa, but the gradient made shallower, we do not

observe changes in cell accumulation on the stiff region of the substrate for SA cells; i.e., they

continue to durotax; for WA cells under the same conditions, they still fail to accumulate (Figure

S3.8E). Thus, it would appear that durotactic and adurotactic behaviors may not be very sensitive

to gradient magnitude but rather the mere presence of a gradient.

Figure 3.3: Differential bond stiffness affect tractions to induce adurotaxis
(A) Model cell speed on simulated on soft or stiff side of step gradient is plotted. Data are shown for cells of differing max SF force, i.e., 45 pN (orange) versus 30 pN (blue), and cells on softer (open) versus stiffer (closed) regions. (n = 100 cells for each simulation). (B) Average traction force per focal adhesion, as determined from the computational model, is plotted for 45 pN (orange) and 30 pN (blue) max SF force (n = 100 cells for each condition). $*p < 0.05$, $**p < 10{-2}$, $***p < 10{-3}$, $****p < 10{-4}$ were determined by one-way ANOVA with Tukey test for multiple comparisons for the indicated comparisons in (A) and (B). (C) For model cells that encounter the step gradient, the fraction of durotactic, anti-durotactic, and adurotactic behavior is plotted. Data represent n = 44 of 100 and 36 of 100 cells simulated at 45 and 30 pN, respectively; those not counted did not interact with the gradient. Comparisons made using a Fisher's exact test for the same migration behavior between 30 and 45 pN conditions, $*p < 0.05$ and $**p < 0.01$. (D) At 0 and 24 h, the model probability density function (PDF) of cell distribution versus simulated hydrogel position is shown for cells with 45 pN (orange) versus 30 pN (blue) max SF force. The stiffer region is shaded in gray. Blue arrow indicates a peak in the 30 pN cell distribution at 24 h. $*p < 0.05$, $**p < 10{-2}$, $****p < 10{-4}$ were determined by paired Student's t test for the indicated comparisons unless otherwise stated.

3.3.3 Adurotactic phenotype is titratable by myosin activity

The dependence of durotaxis on a change of max SF forces implies that the number of active myosin motors per SF filament could affect behavior; prior work suggests that such differences could impart control over cell migration and stiffness[206]. To validate such control in our system, we reduced the number of active myosin motors within a cell, i.e., SF force, finding that it increases the durotactic tendency of cells as predicted by the model between 30 and 45 pN (Figure 3.4A). Furthermore, we tested this experimentally by inhibiting the myosin II activity of WA mammary cells with blebbistatin. Cell speed decreased for blebbistatin treated cells on soft and stiff substrates (Figure 3.4B), resulting in similar velocities as untreated SA cells. Furthermore, treated cells are 2-fold more likely to migrate from the soft substrate into the stiff substrate and much less likely to exhibit antidurotactic migration (Figure 3.4C). WA mammary cells also showed a dose-dependent response to blebbistatin treatment, wherein the WA phenotype became more durotactic, resembling the durotactic behavior of SA cells (Figure 3.4D). Conversely, SA mammary cells also showed a dose-dependent response to lysophosphatidic acid treatment, wherein the SA phenotype became less durotactic, resembling the adurotactic behavior of WA cells (Figure 3.4E). These data confirm the suggestion that max SF force, as produced by the number of active myosin motors per SF filament, enables WA cells to exhibit less durotaxis and is a mechanical argument for why WA cells metastasize.
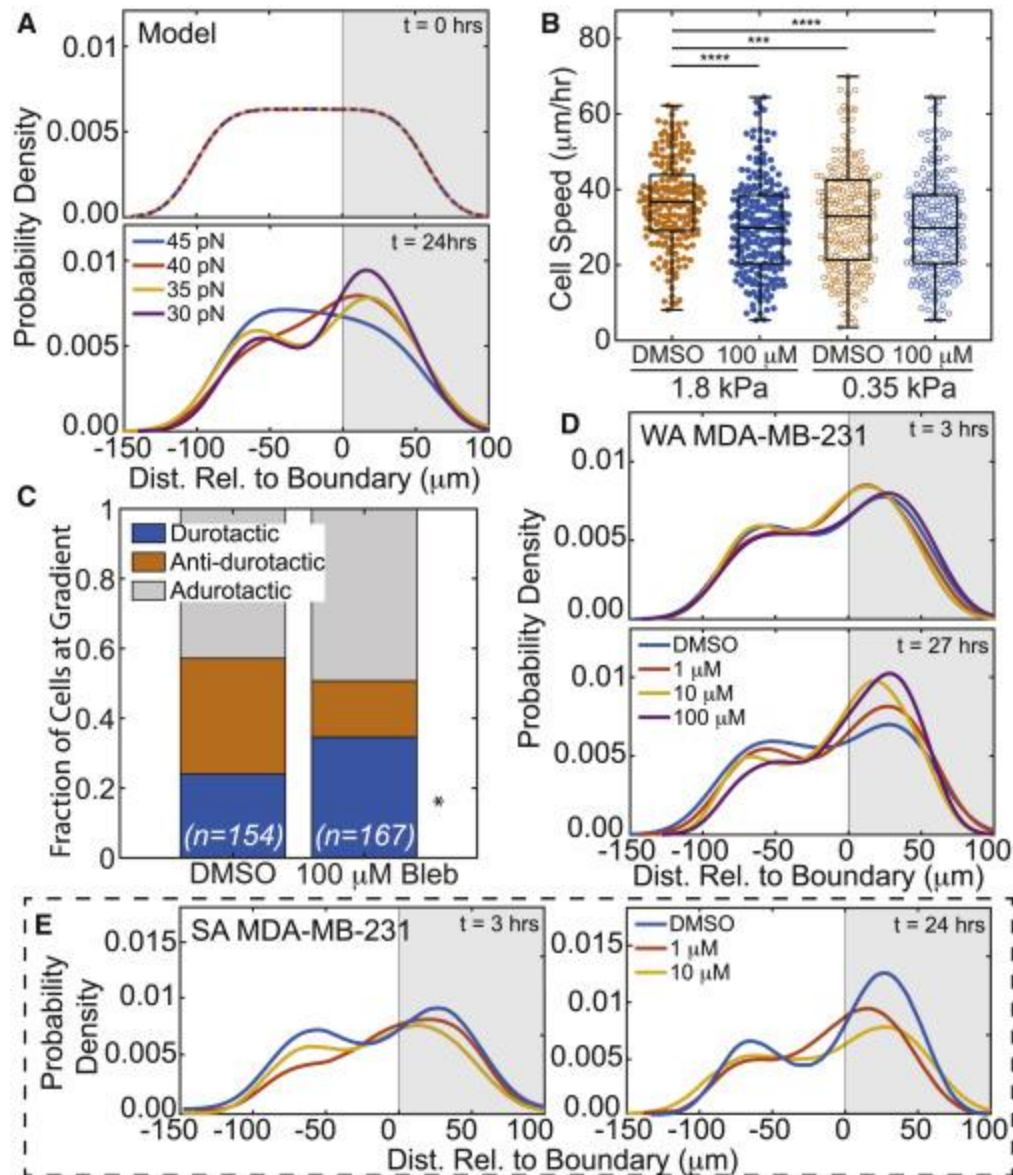
Figure 3.4: Tuning contractility modulates adurotaxis in adhesion-sorted cells
(A) Model PDF of cell distribution versus simulated hydrogel position as predicted for 30 (purple), 35 (yellow), 40 (red), and 45 pN (blue) max SF forces at t = 0 and t = 24 h. Durotactic tendency increased with decreasing max SF force. (B) Weakly adherent MDA-MB-231 cell speed on soft or stiff side of step-gradient hydrogels for cells is plotted. Data are shown for blebbistatin-treated and nontreated cells, i.e., DMSO (orange) versus 100 μM (blue), and cells on softer (open) versus stiffer (closed) regions. (n > 245 cells for each condition from triplicate experiments). ∗∗∗p < 10−3, ∗∗∗∗p < 10−4 were determined by one-way ANOVA with Tukey test for multiple comparisons for the indicated comparisons. (C) For treated and nontreated weakly adherent MDA-MB-231 cells that encounter the step gradient, the fraction of durotactic, anti-durotactic, and adurotactic behavior is plotted. Data represent n = 154 of 256 DMSO-treated and 167 of 245 blebbistatin-treated cells over triplicate experiments; those not counted did not interact with the gradient. Comparisons were made using a Fisher's exact test for the same migration behavior between treated and DMSO, ∗p < 0.05. (D) Weakly adherent MDA-MB-231 PDF of cell distribution was plotted versus hydrogel position for blebbistatin treatment of 100 μM (purple), 10 μM (yellow), 1 μM (red), or DMSO (blue) at t = 3 and t = 27 h. (E) Strongly adherent MDA-MB-231 PDF of cell distribution was plotted versus hydrogel position for LPA treatment of 10 μM (yellow), 1 μM (red), or DMSO (blue) at t = 3 and t = 24 h.

69

3.4 Discussion

The findings of this work help explain how a metastatic cell's distinct mechanotype correlates to the paradoxical migration down a stiffness gradient that occurs during cancer metastasis. Cancer cells isolated by their adhesion strength from a seemingly isogenic population exhibit consistent behavior across different cell lines from vastly different cancer types; moreover, each cancer type exhibits adurotaxis in their tumor-specific niche, which change dramatically for step gradient strength (between 3- and 5-fold) and gradient range (from 0.3 to 30 kPa). Despite these differences, greater contractility in weakly adherent cells is conserved and led to decreased durotactic behavior that is not directly governed by lack of rigidity sensing, as evidenced by slow down at the gradient boundary. From previous work, RNA sequencing shows a distinct underlying phenotype for weakly versus strongly adherent cells with differences in cytoskeletal protein expression, which relates to decreased progression-free and disease-free intervals when compared to the gene expression signatures of human patients[92]. A weakly adherent cell's ability to migrate against stiffness gradients connects this observation to the material properties of the niche, which contribute to its increased metastatic potential.

Computational modeling suggests that mechanotype differences in weakly and strongly adherent cells arises from increased contractility. Furthermore, it demonstrates that catch bonds are a necessary component for the diverging migratory behaviors seen in metastatic cells. Interestingly, catch-bond dynamics have been largely left out of most cell-migration and FA dynamics models until recently[207]. Additionally, the model is able to simulate cells that exhibit both durotaxis and adurotaxis without relying on any a priori assumptions about how rigidity sensing mechanisms are uniquely dependent on substrate stiffness[184]. Actomyosin activity within in single stress fiber largely determines the stress a single bond experiences[206], with substrate

70

stiffness affecting maximum force loading rate. The biphasic nature of catch bond lifetime allows cancer cells to become more migratory and less durotactic with increased contractility, which likely contributes to the greater metastatic potential as well as sets population stability as observed experimentally[92]. That being said, while our data suggest a cytoskeletally driven mechanism, it does not rule out confounding issues from adhesion location, composition, or dynamics.

While material properties change between tumors[85,196–202] and can be affected by cancer treatment[47], we found that durotactic behavior and migration speed can be tuned by actomyosin contractility, without any direct tweaks to protein expression levels. This suggests that the differences in migratory behavior are indeed linked directly to cell mechanotype within its niche. This may also explain why drugs that specifically target proteins involved in cell contractility are so effective at reducing invasion and metastasis. Yet tumors are heterogeneous and likely contain cells that encompass a range of actomyosin activities. Additionally, the ECM surrounding tumors show dynamic, non-linear properties, which are known to influence the outcome of tumor progression and metastasis[208–210]. These heterogeneities and tumor plasticity could present some key challenges to drug development. While our current in vitro and in silico models do not focus on these parameters, our results suggest that future metastatic modeling should couple adhesion dynamics, stress fiber considerations, and heterogeneity in cellular and ECM mechanics when identifying the lowest effective dose required to prevent metastasis.

3.5 Methods

3.5.1 Cell culture

Human metastatic cell lines used in this study include MDA-MB-231 (mammary, female 51 years), PC-3 (prostate, male 62 years), and NCI-H1299 (lung, male 43 years). MDA-MB-231

cells were cultured in DMEM, 10% FBS, and 1% antibiotic/antimycotic; PC-3 cells were

cultured in F-12K, 10% FBS, and 1% penicillin/streptomycin; NCI-H1299 cells cultured in

RPMI 1640, 10% FBS, and 1% antibiotic/antimycotic. All cells were purchased from ATCC and

authenticated by morphology, growth curve, and isoenzyme analysis. PCR was used to verify

cultures were free of Mycoplasma, and cells were not used beyond passage 11. Media reagents

were purchased from Life Technologies.

3.5.2 Fabrication of step-gradient polyacrylamide gels

We used a two-step photopolymerization method described previously[105] to produce

hydrogels with alternating elasticity profiles. Acrylamide concentrations of the prepolymer

solutions were modified to obtain elasticities matching that of the tumor and stromal

environment of each type of cancer. For breast cancer hydrogels, 3% acrylamide (3.7% for lung,

6.4% for prostate) and 0.4% bis-acrylamide were used for the first prepolymer solution, which

was polymerized between a methacrylated 18mm coverslip and a chlorosilanated glass slide by

exposing to ultraviolet light (350 nm) for 5 minutes, using 2-hydroxy-4'-(2-hydroxyethoxy)-2-

methylpropiophenone (0.5%) as the photo-initiator. The PA hydrogel was removed from the

chlorosilanated glass slide and dehydrated for 1 hour on a hot plate at 30° C prior to rehydrating

with a 2% acrylamide (3.7% for lung, 3.2% for prostate) and 0.4% bis-acrylamide prepolymer

solution. The rehydrated gel was again exposed to UV light for 5 min through a high-resolution

chrome patterned photomask 200 μm dark stripes and 100 μm clear stripes. The Young's moduli

of each region were validated using atomic force microscopy.

The hydrogels were then placed in a 12-well plate on top of 50 μl of 2 mg/ml of collagen

I to adhere the coverslip to the bottom of the well. After the collagen polymerized, the gels were

immersed in a solution of sulfosuccinimidyl 6-(4'-azido-2′-nitrophenylamino)hexanoate (0.2

mg/ml, Sulfo-SANPAH; Pierce) dissolved in 4-(2-hydroxyethyl)-1-piperazineethanesulfonic acid buffer (pH 8.4, 50 mM) and exposed to UV light (350 nm) for 10 minutes. After washing several times with PBS, the functionalized surface of the gels was coated with collagen I (150 µg/ml) by incubating overnight at 37° C.

3.5.3 Isolating weakly and strongly adherent cells

Weakly and strongly adherent cells were isolated at varying shear stresses using a parallel plate flow chamber[92]. To ensure sufficient spacing between individual cells, MDA-MB-231 and NCI-H1299 cells were seeded at ~1800 cells/cm2 onto a fibronectin (2 µg/cm2) coated glass plate and incubated overnight. PC-3 cells were found to detach more consistently on a collagen I (1 µg/cm2) coated glass plate and seeded lower at 1500 cells/cm2. For each cell line, PBS free of magnesium and calcium and with 4.5 g/L of dextrose was used to shear cells. Shear stresses used to detach the weakly adherent (WA) population were selected to collect about 20,000 cells at a given flow rate (3 min at 30 dynes/cm2 for MDA-MB-231, 3 min at 60 dynes/cm2 for PC-3 and NCI-H1299 cells). The strongly adherent (SA) population was collected after washing away the intermediate population at a higher shear stress (2 min 500 at dynes/cm2 for MDA-MB-231, 5 min at 300 dynes/cm2 for NCI-H1299, and 2 min at 750 dynes/cm2 for PC-3), and detaching the remaining SA population using 0.25% trypsin-EDTA. Media was then pumped though the device to neutralize the trypsin and collect the SA cells. Collected cells were then seeded onto hydrogels and allowed to adhere for at least 2 hours prior to imaging.

3.5.4 Population-based adhesion assay

Cells were seeded onto 0.35 and 1.8 kPa hydrogels attached to 25 mm glass coverslips that were functionalized with 10 µg/mL human fibronectin. Cells were seeded at a density ~1,800 cells/cm2 to minimize cell-cell contact. Cells attached to coverslips for a minimum of 12

hr using appropriate cell culture media at which time they were then mounted on a custom-built

spinning-disk device[203], submerged into temperature-controlled PBS free of magnesium and

calcium and with 4.5 g/L of dextrose, and exposed to a range of fluid sheer–depending on

rotational speed–for 5 min. Once spun, cells were then fixed with 3.7% formaldehyde. Cell

nuclei were then stained with 4',6-Diamidino-2-Phenylindole (DAPI, 1:2500) and imaged using

a CSU-X1 confocal scanner unit (Yokogawa), QuantEM:512SC camera (Photometrics), and MS-

2000-WK multi-axis stage controller (Applied Scientific Instrumentation) on a Nikon Ti-S

microscope. Metamorph 7.6 software and a custom-written MATLAB script

(https://github.com/englea52/EnglerLab, MathWorks, Natick, MA) was used to stitched together

1500 individual images of nuclei and quantify average cell adhesion, i.e., $\tau 50$, which is defined

as the shear stress at which 50% of the initial cell population is removed by shear stress. Shear

stress was calculated based on Equation 3.1:

$$\tau = \frac{4}{5} r \sqrt{\rho \mu \omega^3} \qquad (3.1)$$

where r is the radial position from the center of the disk, ρ is the buffer density, μ is the buffer

viscosity, and ω is the rotational velocity.

3.5.5 2D migration assays

Isolated cells were seeded at ~1500 cells/well onto step-gradient gels fixed in a 12-well

plate and allowed to adhere for no more than 2 hours to ensure a random distribution across the

step-gradient at the start of imaging. The cells were imaged over 24 hours using a Nikon Eclipse

Ti-S microscope equipped with a temperature and CO2 controller (Pathology Devices Inc.,

LiveCell). Images at multiple cell positions were taken in brightfield at 10x every 15 minutes.

Cell trajectories were collected and analyzed using a custom MATLAB script

(https://github.com/compactmatterlab/Durotaxis, MathWorks, Natick, MA). To prevent biases

due to differences in cell division on soft or stiff substrates, daughter cells were excluded in trajectory analysis. From cell trajectories, we categorized cell migration as durotactic, anti-durotactic, or adurotactic, meaning that cells migrated across the substrate stiffness boundary only from soft to stiff, only from stiff to soft, or crossed the boundary multiple times, respectively; cells never approaching the boundary were not categorized. Trajectories were used to determine the distance between each cell and its closest soft-stiff boundary and plot the distribution of cells across the boundary. For cell migrating under drug treatment, cells were treated with either DMSO, 1µM, 10µM, or 100µM (S)4'nitroBlebbistatin (24171, Cayman Chemical Co.) or lysophosphatidic acid and imaged 3 hours after treatment for up to 24 hours.

3.5.6 Traction force microscopy

Traction forces were measured as previously described and calculated using a custom MATLAB script[122]. Cells were seeded on to single-modulus polyacrylamide hydrogels with an elasticity matching their respective tumor microenvironment. Prepolymer solutions contained 2% (v/v) of 0.2 µm diameter 580/605 FluoSpheres microspheres (Invitrogen). Gels were prepared as we previously described[92] in 24-well glass bottom plates (Cellvis). Cells were seeded at ~5,000 cells per well and allowed to adhere for at least 3 hours. Brightfield images were taken at 60x to obtain cell areas as measured in ImageJ. Bead images were then captured every minute for 30 minutes. Reference images were then taken after removing the cells with 10% (v/v) Triton X solution. Traction forces were determined from the traction stress map and normalized to cell area.

3.5.7 Computational modeling

To understand how durotaxis and adurotaxis can occur due to differences in cell contractility and adhesion dynamics, we built a computational model that incorporates focal

adhesion formation, stress fiber (SF) mediated force generation, and catch or slip bond dynamics between the cell receptors and surface adhesion sites. This model is described in detail below.

1) A cell is defined by a central point. A random number of stress fibers, obtained from a Poisson distribution with mean μ_{SF}, are generated about the central point. Each stress fiber has an initial length equal to the radius of the cell (5 µm) and is oriented radially. The angular distribution of these stress fiber is uniform from 0 to 2π radian.

2) These stress fibers can then grow in length radially based on the rate of actin polymerization (v_{act_L} if along the leading edge, defined by a region within -π/2 and π/2 radians of the cell migration direction, or v_{act_T} if in the direction of the trailing edge, a region complimentary to the leading edge) or shrink in length based on the rate of depolymerization (v_{ret}). (Initial cell migration direction is picked randomly, though this changes as described in part 7). The stress fibers switch from polymerization to depolymerization sporadically at time intervals generated from an exponential random number based on an average retraction time (t_{ret}), while depolymerization stops when the stress fiber reaches a minimum length (assumed to be the cell radius). The polymerizing and depolymerizing stress fibers are free to diffuse angularly about the cell center, with a diffusion coefficient dependent on the length of the SF[211], Equation 3.2.

$$D_{rot} = \frac{3k_B T ln(L/d_{act})}{\pi \eta L^3}$$

(3.2)

Here k_B is Boltzmann's constant, T is temperature, L is the length of the actin filament, d_{act} is the diameter of an F-actin, and η is the viscosity of the cytoplasm.

3) Both polymerizing and depolymerizing SFs can bind to the substrate at their free end and begin to form a focal adhesion via integrin-substate bonds. This arrests the growth, shrinking and diffusion of the SF. The newly formed ECM-integrin-SF complex may be comprised of

solely an adaptor protein (i.e., paxillin[212], zyxin[213], etc.[214–216]), an adaptor protein with a stress sensor protein (i.e., vinculin[217,218], talin[218,219]), or branched (i.e., Apr2/3[220]) with some combination of adaptor and tension sensor proteins. The dynamics of these protein interactions are modeled by first determining the SF-integrin-ECM binding probability, calculated by Equation 3.3,

$$P_{on} = 1 - e^{-\Delta t k_{on}} \tag{3.3}$$

where Δt is the model's timestep and k_{on} is the assembly rate of the SF-integrin-ECM complex. The number of integrins bound to the SF is determined stochastically using the Poisson distribution with an average given by the average number of integrins/F-actin (μ_{Int}). We assume stress fibers with more than one integrin have a branching protein already bound to the SF prior to assembly of the complex. Likewise, each integrin has a certain probability (P_{tal}) of being bound to a stress sensor protein prior to complex assembly.

4) Integrin-ECM bonds have a certain probability of unbinding based on the applied load on each bond via the SF and the catch or slip bond dynamics measured experimentally[130] by Kong et al. and calculated by (Equation 3.4a), (Equation 3.4b), (Equation 3.4c),

$$P_{off} = 1 - e^{\Delta t k_{off}(f)} \tag{3.4a}$$

$$k_{off}(f) = \left[A e^{-f\xi/k_B T} + \left(B e^{f\xi/k_B T} + C e^{-f\xi/k_B T} \right)^{-1} \right]^{-1} \quad for\ catch \tag{3.4b}$$

$$k_{off}(f) = K_0 e^{f/F_b} \quad for\ slip \tag{3.4c}$$

where A, B, and C are constants, ξ is the unbinding length, and f is the load on an individual bond. For slip bonds, K_0 is the unloaded off rate and F_b is the characteristic bond rupture force[72]. When a single SF is bound to multiple integrin-ECM bonds, the SF forces is distributed equally across each of these bonds.

5) The SF force increases exponentially with time[51] based on Equation 3.5,

$$F = F_s \left(1 - e^{-v_0 K_{ecm} t / F_s} \right)$$ (3.5)

where F_s is the max SF force, determined by the myosin motor force (F_{myo}) times the

number of myosin motors (n_{myo}). v_0 is the myosin sliding velocity and K_{ecm} is the

underlying ECM stiffness. The model is based on the linear force velocity relationship of

molecular motors such as non-muscle myosin II[221], and a simple two-spring model. The

stiffness of the ECM is converted from the user defined Young's modulus (E_{stiff}, E_{soft}) by

multiplying the modulus with a characteristic length (set to 0.1 μm) based on the order of

magnitude for molecular sensing of myosin and related motor protein structures, e.g., thin

filaments. The ECM stiffness value is spatially varied to simulate the photopatterned PA

gels with a gradient length (L_{grad}) of 10μm between the soft and stiff regions, as determined

from AFM measurements. The stiffness of the protein complexes involved in the ECM bond

is neglected as they are an order of magnitude stiffer than the underlying substrate.

6) If a tension sensor protein experiences a sufficiently large force $f > F_{thres}$ it opens actin

binding sites for recruiting new SFs[217,218], leading to FA growth and maturation. A new SFs

(not one of the existing SFs) will bind to this open site with a given probability determined

by Equation 3.6,

$$P_{act} = 1 - e^{-t_{SF} K_{act}}$$ (3.6)

where t_{SF} is the time the binding site has been open and K_{act} is the SF binding rate. Number

of new SFs that can be recruited is limited by a finite max number of SFs possible in the cell

(n_{SF}). The new stress fibers are not explicitly simulated as the initial free SFs described in

part 2, but are included as newly formed ECM-Integrin-SF complexes described in part 3,

within the vicinity of and parallel to the recruiting ECM-Integrin-SF complex.

7) The forces at all bound ECM-Integrin-SF complexes are then summed ($\sum \vec{F}$) to get the net force on the cell, which is divided by the friction factor due to bound integrins to calculate the distance the cell will move before the next time step, Equation 3.7.

$$\vec{d} = \Delta t \frac{\sum \vec{F}_i}{n_b \Pi} \tag{3.7}$$

where F is the force generated by each SF, n_b number of active integrin bonds, and Π is the friction factor for an individual bond. The direction of migration also determines the new leading and trailing edges of the cell.

8) SF ends attached to active integrin bonds remain stationary in space as the cell moves. ECM-Integrin-SF complexes deteriorate if all integrin-ECM bonds an SF is attached to are broken. When no ECM-Integrin-SF complexes remain attached in the FA, the FA is dissolved releasing a free SF into the cell. The position of the free SF end is updated with the cell position before the next iteration begins.

9) During any timestep, the dynamics of the free SFs (SFs not bound to integrins) are determined as described in part 2.

Values for each parameter used in this model are shown in Table S3.1. We simulate 24 hours of cell migration, and track the cells position relative to the soft/stiff boundary as in the time-lapse microscopy images. The model loops through the flow schematic in Figure S3.8A and described in detail above, with each loop comprising a single timestep.

3.5.8 Immunofluorescence staining and FA analysis

MDA-MB-231 cells were seeded onto single moduli gels (either 0.48 kPa or 1.8 kPa) and allowed to adhere overnight. Cells were washed with PBS with cations and fixed with 4% paraformaldehyde for 10 minutes. Fixed cells were then stained with deep red cell mask in PBS (1:1000 v/v; Thermofisher Scientific) for 10 minutes. 0.1% TritonX in PBS was used to

permeabilize the cells for 10 minutes. Blocking was done with PBS supplemented with FBS (10% v/v, Gemini Bio) for 20 minutes at room temperature. Cells were incubated overnight at 4° C with primary paxillin antibody (1:500; ab32084, Abcam) in blocking buffer. Gels were then washed with blocking buffer and incubated with secondary Alexa Fluor 488-conjugated antibody (1:500; A11008, Invitrogen) and rhodamine phalloidin (1:3000, R415, Thermofisher Scientific) for 1 hour at room temperature, followed by Hoechst 33342 (1:2000; Invitrogen) in DI water for 10 minutes. Coverslips were then mounted onto slides with Flouromount-G (Southern Biotech). Samples were imaged using a Zeiss LSM 780 confocal microscope (Zeiss) with a 63x oil-immersion objective. A custom MATLAB script was used to measure cell area and size and number of focal adhesions.

3.5.9 Cytokine antibody array

Media was analyzed using the Proteome Profiler Human XL Cytokine Array (R&D Systems). Briefly, membranes were blocked for 1 hour using array buffer, and media was then combined with array buffer overnight at 4°C with rocking. Membranes were washed, incubated with the antibody cocktail diluted for 1 hour, washed, and incubated with streptavidin-HRP for 30 minutes, and finally treated with chemiluminescent reagent mix; membranes were exposed to film and imaged. Pixel quantification was performed in ImageJ and normalized to positive and loading controls. Conditioned media for SA and WA cells on 0.35 and 1.8 kPa substrates were normalized to internal loading control spots and plotted against each other.

3.5.10 Quantification and statistical analysis

Comparisons for migration speeds and traction forces were done using a two-tailed unpaired t test or one-way ANOVA with Tukey test for multiple comparisons for the indicated comparisons where appropriate and as indicated. Categorical comparisons for durotactic, anti-

durotactic, and adurotactic cells were done using a Fisher's exact test using definitions from the 2D migration assay section of this manuscript; again, durotactic cells were defined as cells that are on the soft region at the start of the time lapse and migrated to the stiff in the 24 hours of imaging, and vice versa for anti-durotactic. Adurotactic cells were defined as cells that crossed the boundary at some point during imaging and returned to the substrate they started on. Probability density estimations were calculated using MATLAB's kernel smoothing function and plotted to visualize cell distributions at the start of imaging (t = 0 h) and after 24 hours of imaging (t = 24 h). The theoretical optimum bandwidth for the kernel smoothing function was used to generate reasonably smooth curves. Despite potential errors near the edges of the bounded region (−57.5 to 85 μm of the boundary), to reduce sensitivity to sampling error, we chose to use an unbounded KDE. This does not affect the cell density estimation near the stiffness gradient. P values for all analyses, ∗, $p < 0.05$; ∗∗, $p < 0.01$; ∗∗∗, $p < 0.001$; and ∗∗∗∗, $p < 0.0001$. Outliers were removed only in plotting using MATLAB's quartiles method, so box-and-whisker plots remove points outside the whisker ends, defined by 1.5 interquartile ranges above the upper quartile or below the lower quartile. Other error bars were expressed as mean ± SD. Statistical analyses were done using MATLAB.

3.6 Supplementary Information
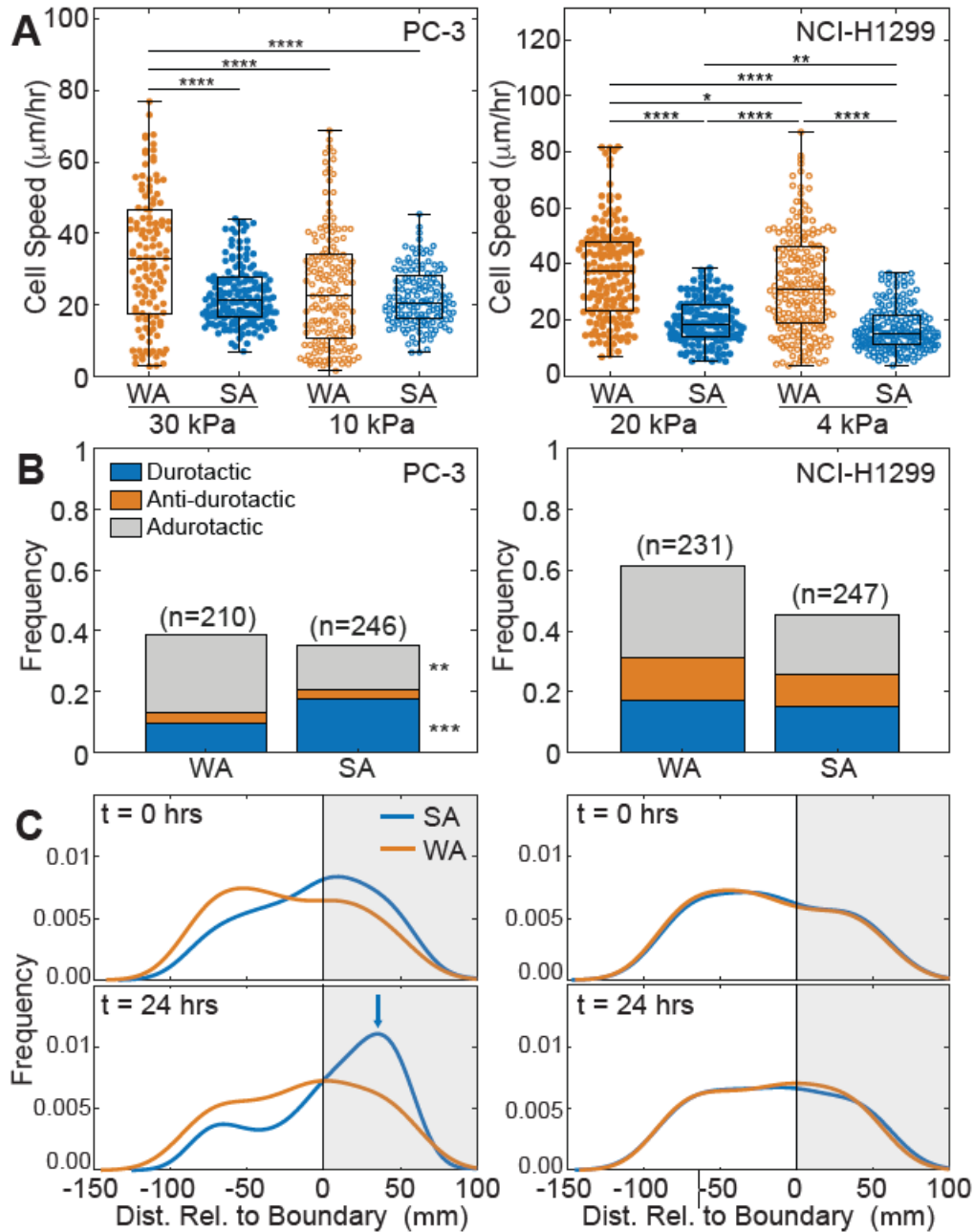
Supplemental Figure S3.5: Weakly adherent cells exhibit higher adurotactic behavior
(A) PC-3 (left) and NCI-H1299 (right) cell speed on soft or stiff side of step-gradient hydrogels is plotted. Data is shown for cells sorted by adhesion strength, i.e., weakly (orange) vs. strongly (blue), and cells on softer (open) vs. stiffer (closed) regions. (n>200 cells for each condition from triplicate experiments). (B) For adhesion sorted PC-3 and NCI-H1299 cells that encounter the step-gradient, the frequency of durotactic, anti-durotactic, and adurotactic behavior is plotted. Data represents n= 210, 246 for PC-3 and n= 231, 247 for NCI-H1299 cells over triplicate experiments. (C) At 0 and 24 hours, PC-3 and NCI-H1299 cell frequency versus hydrogel position is shown for weakly (orange) vs. strongly (blue) adherent cells from triplicate experiments. The stiffer region is shaded in gray. Blue arrow indicates a peak in the strongly adherent cell distribution at 24 hours. *p<0.05, **p<10-2, ****p<10-4, *****p<10-5 determined by paired student t-test for cell speeds and a Fisher's exact for durotactic frequencies for the indicated comparisons.
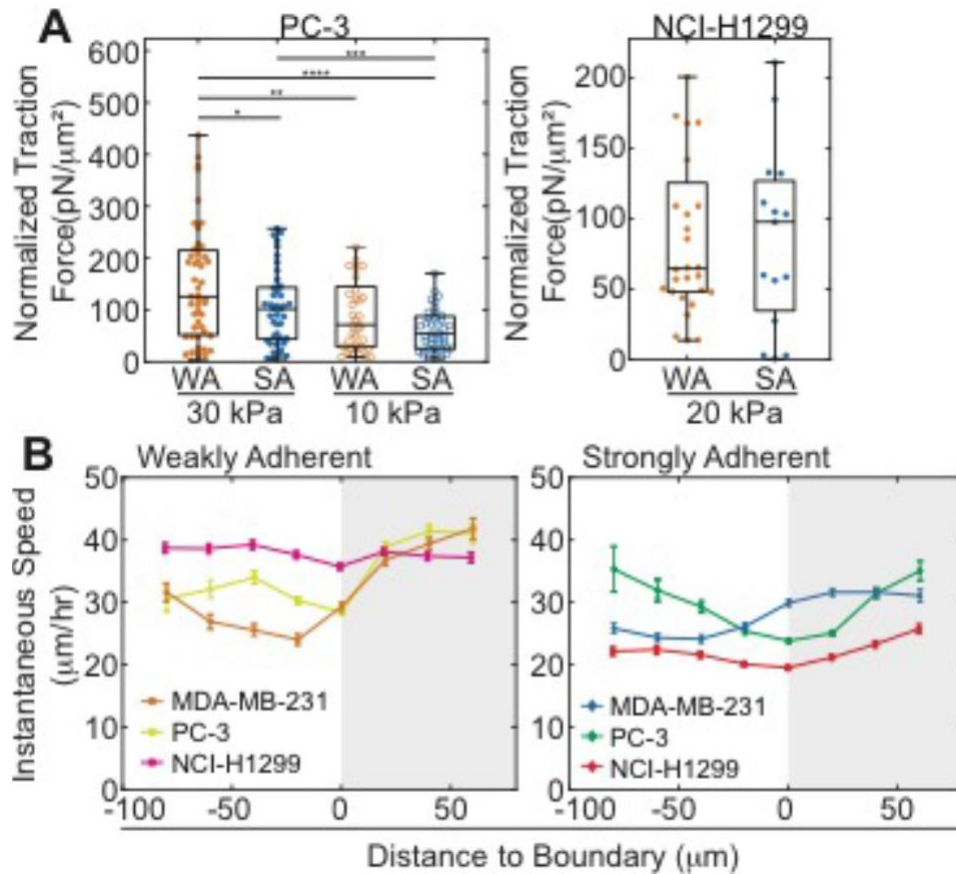
Supplemental Figure S3.6: Traction forces and instantaneous speed for PC-3 and NCI-H1299 cells
(A) Traction force, normalized to cell area, plotted for PC-3 cells on soft or stiff single-modulus (left) hydrogels and NCI-H1299 cells on stiff hydrogels (right). Data is shown for weakly (orange) vs. strongly (blue) adherent cells, and open circles for PC-3 cells on soft (n>47 for PC-3, n>15 for NCI-H1299). *p<0.05, **p<0.01,***p<0.001, and ****p<0.0001 via one-way ANOVA with Tukey test for multiple comparisons for the indicated comparisons. (B) Instantaneous cell speed is plotted as a function of position relative to the step-gradient for adhesion sorted weakly (left) and strongly (right) adherent MDA-MB-231 (orange/blue), PC-3 (yellow/green), and NCI-H1299 (pink/red) cells. Negative values are on the soft substrate and positive are on the stiff. Average speed ± standard error of the mean is plotted for n>144 cells for each condition from triplicate experiments.
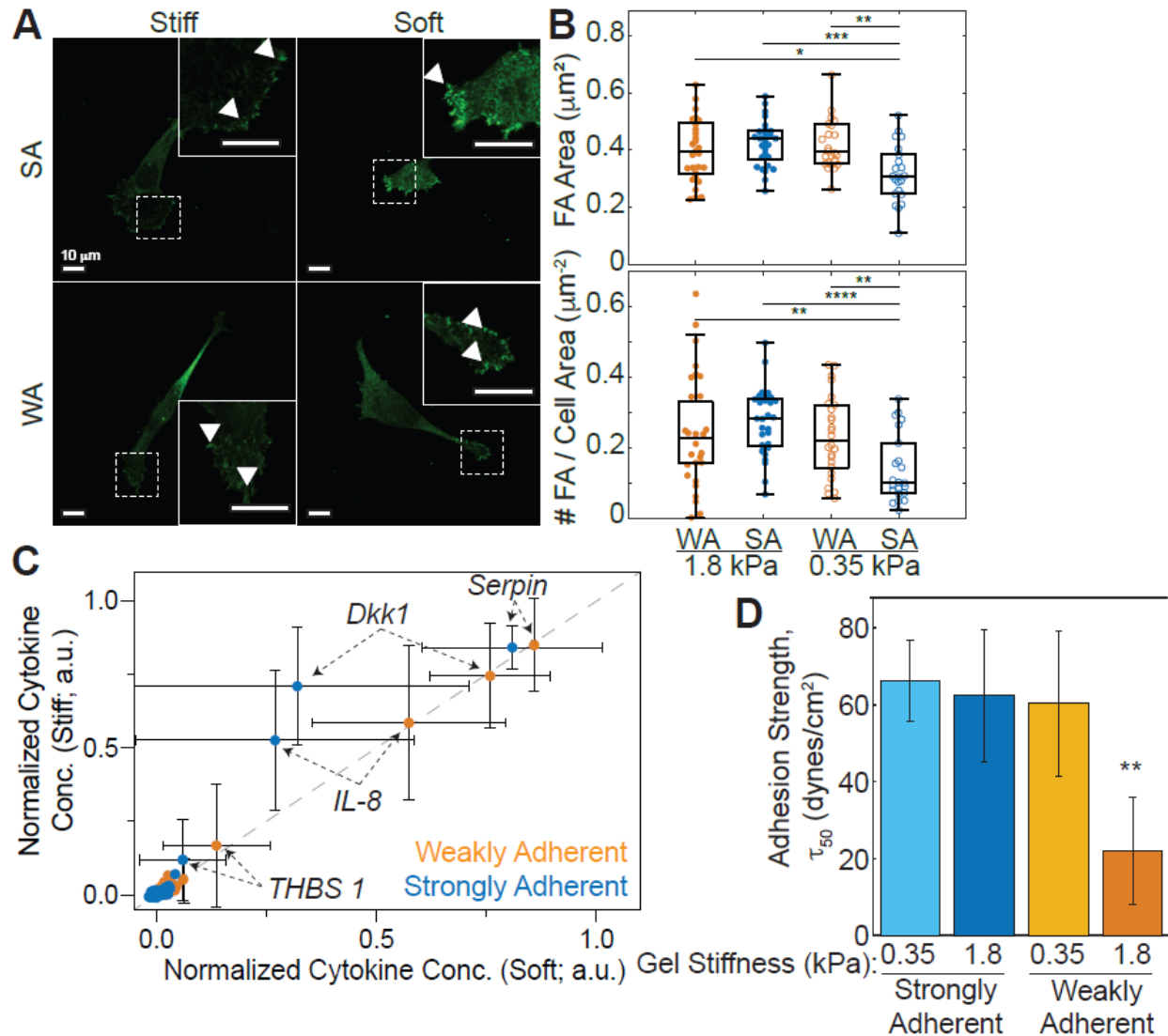
Supplemental Figure S3.7: Effects of focal adhesions, cytokines, and stiffness on adhesion

(A) Representative images of FAs in weakly and strongly adherent MDA-MB-231 cells on soft or stiff single modulus hydrogels. Paxillin is shown in green and highlighted in the inset images (dashed boxes indicating which regions are magnified) by arrowheads that point to representative paxillin adhesions. Scale bar is 10 μm. (B) FA area (top) and number of FAs normalized to cell area (bottom) are plotted for the indicated sorting and elasticities. n>20 cells/condition from triplicate experiments. (C) Cytokine expression for WA and SA cells, normalized to loading controls, is plotted ± standard deviation for 105 cytokines found in cell culture media collected from WA (orange) and SA (blue) MDA-MB-231 cells plated onto soft (0.35 kPa) and stiff (1.8 kPa) hydrogels for 65 24 hours. Specific cytokines expressed above background noise are noted with corresponding error bars from triplicate media collections; dashed arrows link cytokine names with their respective data. No data was statistically different between substrate stiffness or adhesion mechanotype based on one-way ANOVA with Tukey test for multiple comparisons. (D) Post-selection weakly and strongly adherent MDA-MB-231 cells were plated onto hydrogels of indicated stiffness and subjected to a shear stress gradient. Adhesion strength or t50, i.e., the shear stress at which 50% of the population detaches from the substrate, is plotted ± standard deviation. *p<0.05, **p<0.01, ***p<0.001, and ****p<0.0001 via one-way ANOVA with Tukey test for multiple comparisons for the indicated comparisons.

84
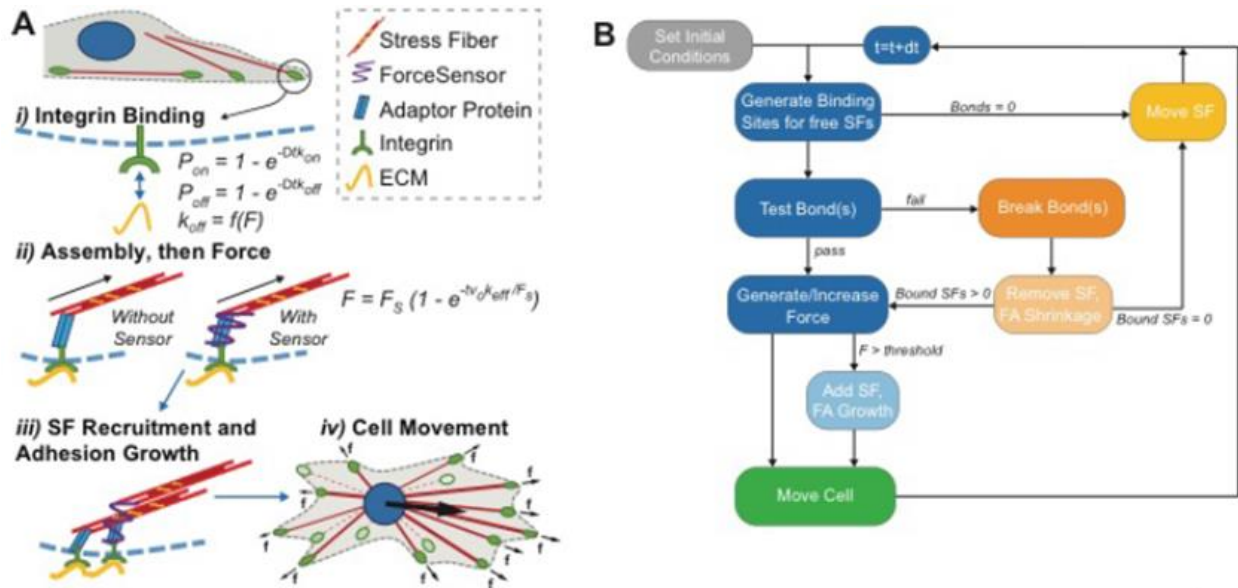
Supplemental Figure S3.8: Computational model schematic and sensitivity to stiffness
(A) Schematic of rigidity sensing in cells where softer catch bonds, i.e., strongly adherent cells, leads to asymmetric adhesion maturation at the step-gradient whereas stiffer bonds in weakly adherent cells break and prevent rigidity sensing. This occurs in four phases: i) integrin binding, ii) assembly and force production, iii) adhesion growth and stress fiber recruitment, and iv) cell movement. (B) Diagram indicates the decision logic for the computational durotaxis model described in Figures 2 and 3. Gray indicates initial conditions, which feed in to the force on adhesions equations (blue). Adhesion outcomes are shown in orange with cell migration shown in green. Arrows indicate the decision logic with notes about each pathway indicated above or to the side of the decision.
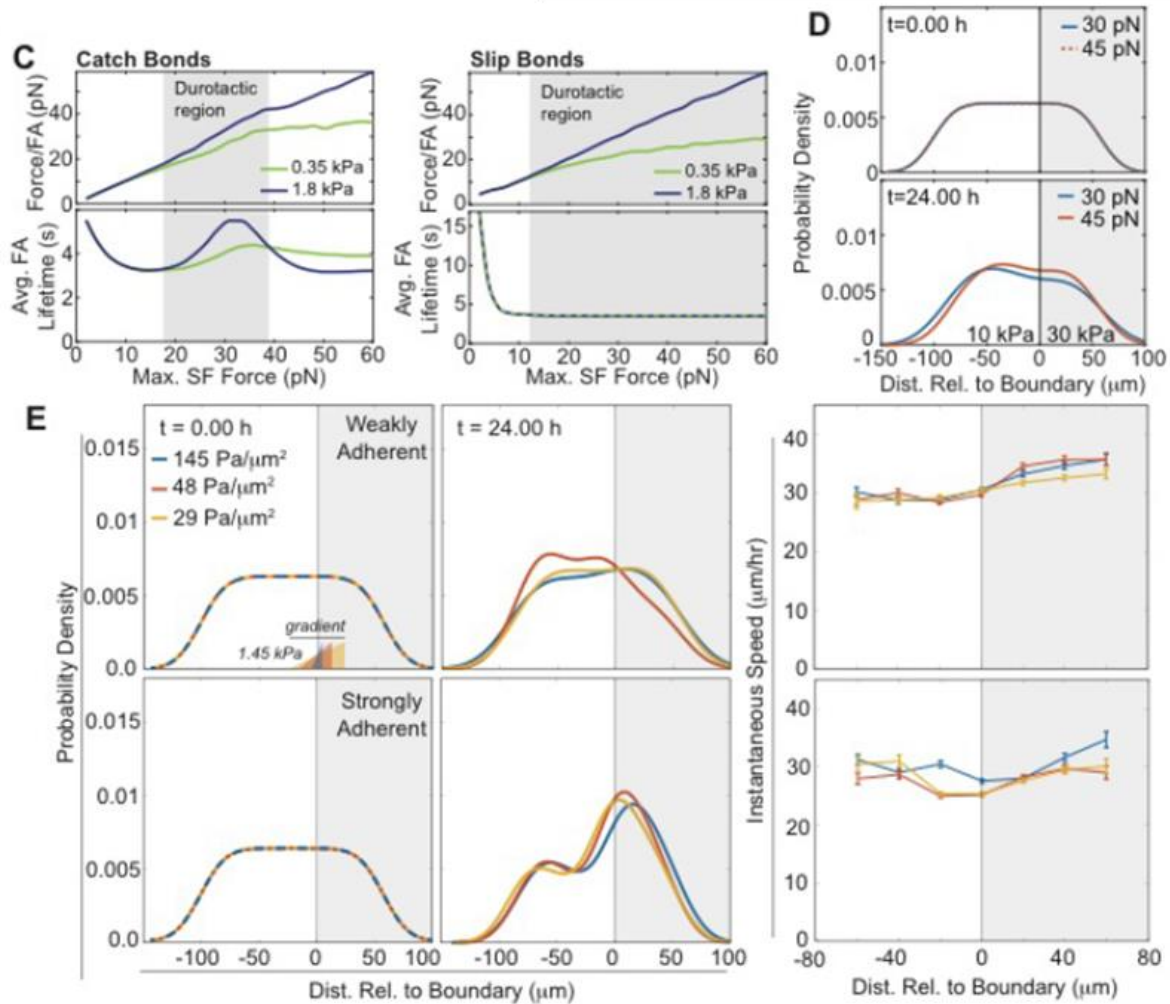
Supplemental Figure S3.9-Continued: Computational model schematic and sensitivity to stiffness
(C) Comparison of catch (left) and slip (right) bond dynamics, Force/FA (top) and average FA lifetime (bottom) as a function of max SF force for ECM stiffnesses fixed at 0.35 or 1.8 kPa (green and blue, respectively). The gray region highlights where force is greater and bond lifetime is also greater or equal than it is on soft, which corresponds to the onset of durotactic behavior. (D) Model cell durotaxis on gradients with a different stiffness range at 0 and 24 hours, model cell probability density versus simulated hydrogel position is shown for cells with 45 pN (orange) vs. 30 pN (blue) max SF force. The stiffer region is shaded in gray (30 kPa) vs. the softer region in white (10 kPa); values were chosen to mirror prostate tumor gradients rather than mammary tumor gradients to which model parameters were otherwise tuned. (E) Model cell durotaxis on gradients of different magnitude but same stiffness range. (Left) At 0 and 24 hours, model cell probability density versus simulated hydrogel position is shown for cells with 45 pN (Weakly Adherent) vs. 30 pN (Strongly Adherent) max SF force. The stiffer region is shaded in gray (1.8 kPa) vs. the softer region in white (0.35 kPa); gradient slope was changes as indicated. All previous simulations use 145 Pa/µm2 (blue) but plots here also include gradients 3- (dark orange) and 5-fold shallower (light orange). (Right) Instantaneous cell velocities ± S.E.M. for the indicated gradients and WA (top) or SA (bottom).

86

Supplementary Table S3.1: Model parameters and values

Parameter	Description	Value	Source
F_{myo}	Myosin Motor Force	2 pN	[222]
n_{myo}	# of Myosin Motors/F-actin	Adjustable, 10-25	[223]
Π	Bond friction factor	2×10^{-5} kg s^{-1}	[224]
t_{ret}	Retraction Time	10 s	[10,225]
F_{thres}	Force sensor threshold	1 pN	[217,218]
K_{on}	Integrin-SF assembly rate	0.1 s^{-1}	[226,227]
K_{act}	Actin-Talin assembly rate	1 s^{-1}	[228]
k_{off}	Unbinding rate	Calculated, s^{-1}	
μ_{Int}	Average Integrins/F-actin	1	[229]
P_{tal}	Probability of force-sensor protein	0.7	[230]
v_{dis}	Actin disassembly velocity	0.5 µm s^{-1}	[231]
v_{act_L}	Actin assembly, leading edge	0.2 µm s^{-1}	[231–233]
v_{act_T}	Actin assembly, trailing edge	0.1 µm s^{-1}	[231–233]
E_{stiff}	Young's modulus, Stiff	1800 Pa, Measured experimentally	
E_{soft}	Young's modulus, Soft	350 Pa, Measured experimentally	
L_{grad}	Gradient Length	10 µm, from AFM measurements	
n_{SF}	Maximum SFs/FA	Adjustable, 100	[233]
μ_{SF}	Average assembly sites/cell	Adjustable, 50	[234]
v_0	Myosin sliding velocity	1 µm s^{-1}	[235]
D_{rot}	Rotational diffusion constant of F-actin	Calculated, s^{-1}	
η	Cytoplasm (water) viscosity @ 37C	0.0006913 Pa s	
T	Temperature	310.15 K	
k_B	Boltzmann's constant	1.3806E-23 kg m^2 s^{-2} K^{-1}	
L	Length of actin filament	Calculated, µm	
d_{act}	Diameter of Actin	7 nm	[236]
A	Fitting constant	3.309	
B	Fitting constant	0.0003942	
C	Fitting constant	58.19	
ξ	Unbinding length	0.7959 nm	[130]
F_{max}	Max filament force	F_{myo} x n_{myo}	
K_{ECM}	ECM stiffness	ECM modulus x 0.1 µm	

3.7 Acknowledgements

Chapter 3, in full, is a reprint of the material as it appears in Yeoman, B., Shatkin, G., Beri, P., Banisadr, A., Katira, P., and Engler, A.J., "Adhesion Strength and Contractility Enable Metastatic Cells to become Adurotactic." *Cell Reports*, 2021. 34(10): 108816. The dissertation author was the primary author of this paper.

CHAPTER 4. STROMAL CELL ADHESION PREDICTS SEVERITY OF METASTATIC DISEASE

4.1 Abstract

Despite better outcomes with early-stage detection, local invasion significantly reduces patient survival rates for many carcinomas. Heterogeneity within and between tumors has precluded identification of predictive biological markers, but adhesion strength has emerged as a potential biophysical marker. Here we demonstrate that cells disseminating from mammary tumors are weakly adherent, and when presorted by adhesion, primary tumors created from strongly adherent cells exhibit fewer lung metastases than weakly adherent cells or unsorted populations. Migratory ontologies from tumors correlate with freshly sorted cells, suggesting that cell intrinsic differences are maintained *in vivo*. We further demonstrate that admixed cancer lines can be separated by label-free adhesive signatures using a next-generation flow chamber. When applied to metastatic tumors, the device retrospectively predicted metastatic disease from stromal samples with 100% specificity, 85% sensitivity, and AUC of 0.94. Data from this device suggest that label-free adhesive signatures may effectively predict clinical outcomes in patients.

4.2 Introduction

Tumors are often detected and treated when disease is local, but when epithelial carcinomas become regionally invasive, 5-year recurrence rates can exceed 15% for breast cancer and are even worse for other solid tumors[237,238]. Patient relapse is multifactorial, but it is due in part to our inability to identify metastasizing cells early, quantify their presence in stroma, and create appropriate risk assessments to guide standards of care. Significant efforts have

89

attempted to identify universal molecular prognostic markers[137,139] from liquid biopsies but have

only identified tumor-specific markers at best[139,239], owing in part to cell heterogeneity[153] and a

lack of marker exclusivity[139,240,241]. These assays also only surveil cells post-intravasation,

missing an opportunity to assess dormant cell populations resident in tumor-adjacent stroma[242].

Metastasis can be compartmentalized into a series of discrete physical events required for

all solid tumors: detachment from tumor, migration through stroma, and intravasation into the

blood stream[102,243–245]. At each step, cells undergo numerous, distinct biophysical changes that

enable metastasis[102,118,140–143]. As with many molecular marker assays, recent FDA-approved

devices that utilize biophysical markers focus on detecting circulating tumor cells (CTCs).

However, CTC detection in the blood may be a point at which disease has already progressed too

far for effective prognostic assessment; tumor cells can often remain dormant in stroma for

years[242], and significant sample dilution may allow some CTCs to escape detection. Conversely

stromal-based physical assays are now being used to probe cells from these heterogeneous yet

dormant populations[102] and determine their mechanotypes[90]. For example, microchannel assays

that confine cancer cells as they migrate have been used to determine invasive mechanisms[99] and

to assess progression-free survival[128], making widespread clinical adoption more feasible. Weak

adhesion strength is another biophysical metastatic marker that promotes migration via increased

focal adhesion turnover[123,144–149,246]. Triple negative breast cancer patients whose tumors have

transcriptomic profiles mirroring weakly adherent cells also have shorter disease-free

intervals[246], suggesting a correlation between clinical outcomes and physical properties, i.e., an

adhesion mechanotype.

Despite strong evidence, adhesion data have not yet established a predictive capacity for

metastatic disease. Herein, we use straight- and divergent-wall parallel plate flow chambers

(PPFCs) to evaluate sorting and analysis capabilities using admixed and stromal cell populations. We find an inverse relationship between adhesion strength and metastatic behavior using a murine mammary tumor model. Cells that sort as weakly adherent are more migratory, result in more secondary disease, and have a stable mechanotype *in vivo*. PPFC analyses provide label-free measurements of adhesion strength and cell abundance relative to the analyzed population, which when used for admixed cancer lines enables separation and when applied to metastatic disease can retrospectively predict metastatic potential. These results suggest that weakly adherent cells migrate out of the primary tumor microenvironment and can be isolated to prognostically assess future patient outcomes.

4.3 Results

4.3.1 Invading cells have decreased adhesion strength compared to primary tumors

Metastatic cell lines have lower adhesion strength and more labile focal adhesions than their non-metastatic counterparts[123]. To determine to what extent a mouse tumor model phenocopies adhesion, MDA-MB231 mammary epithelial cells were exposed to lentiviral vectors containing GFP and firefly luciferase (Luc) and selected for both markers (Supplemental Figure S4.6A-B). To ensure that transduction did not impact adhesion strength and migration, cells were selectively exposed to pre-determined shear stresses to isolate weakly and strongly adherent fractions[1] and their migration was assessed on collagen gels; weakly adherent cells exhibited greater migration speed and displacement compared to strongly adherent cells (Supplemental Figure S4.6C-D), which is consistent with untreated cells[246] and indicates that GFP and Luc transduction had minimal impact on function. Given that adhesion and migration speed are inversely correlated *in vitro*, we next determined this relationship *in vivo*. GPF$^+$Luc$^+$

MDA-MB231 cells were injected into inguinal fat pads of 11-week-old NOD/SCIDγ mice, monitored at 2-week intervals, and resected at 6 weeks post injection (Supplemental Figure S4.7A-B). GFP+ cells were isolated from tumor and stroma, sorted using FACS, and their adhesion profile quantified (Figure 4.1A, Supplemental Figure S4.7C). The GFP+ fraction in stroma was lower than in tumor (Figure 4.1B) and significantly less adhesive compared to tumor resident GFP+ cells (Figure 4.1C). For paired samples isolated from the same fat pad, GFP+ tumor cells were 60% more adherent than GFP+ stromal cells (Figure 4.1D), suggesting that cells of the weakly adherent mechanotype escape the tumor, consistent with the observations in culture[247].
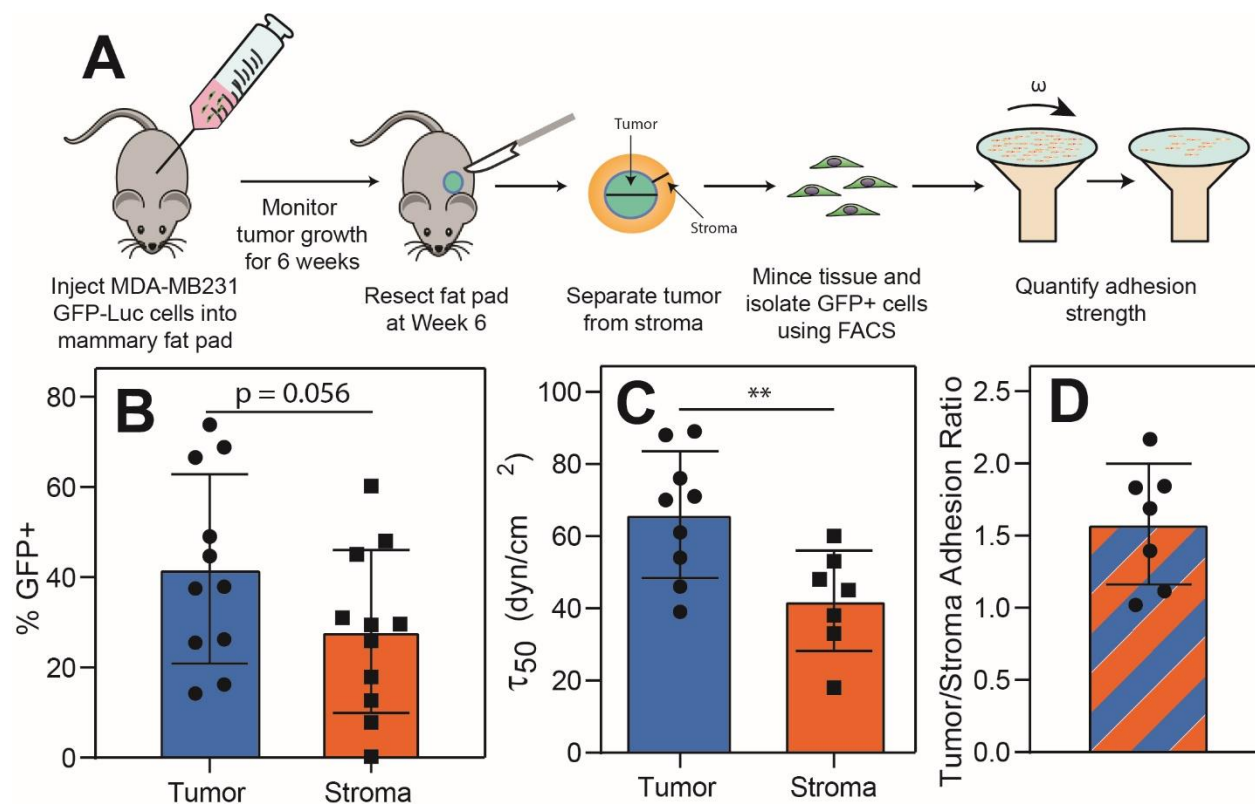
Figure 4.1: MDA-MB231 cells that have invaded into the stroma display decreased adhesion strength compared to cells in the stiff tumor

(A) Timeline of tumor resection and adhesion strength study. (B) There are fewer GFP-positive cells present in the stroma versus the tumor (n=11). (C, D) Invaded MDA-MB231 cells have decreased adhesion strength compared to MDA-MB231 cells that remain in the tumor (n=9 and 7 for tumor and stroma, respectively; n=7 for paired samples in panel D). (B, C) Statistical analysis via unpaired t-test. ** represents $p<0.01$.

4.3.2 Cell intrinsic adhesion differences correlate with lung metastatic frequency

While cells that disseminate are less adherent, it is not clear if this translates to a greater propensity to form secondary sites of disease. To artificially create differences in metastatic potential between tumors, GFP[+]Luc[+] MDA-MB231 cells were first sorted by adhesion using a parallel plate flow chamber (FFPC; Supplemental Figure S4.8) and then injected into inguinal fat pads. Tumors were allowed to grow for 6 weeks prior to assessing primary tumors and secondary disease in the lungs (Figure 4.2A-B). While there was no difference in primary tumor weight (Figure 4.2C), transcriptional analyses of primary tumors found 265 differentially expressed genes (DEGs) with adhesion strength (Figure 4.2D-E), indicating that they retain pre-injection differences. Gene ontology (GO) terms associated with DEGs were stratified and compared to those of cells sorted *in vitro* (Figure 2F)[246]; we found significant GO term overlap for biological processes, and among these terms, many were associated with cell migration and locomotion (Figure 4.2G, red; Supplemental Table S4.1). These data suggest a common gene signature that may correlate with metastatic risk and establish what constitutes an adhesive mechanotype.
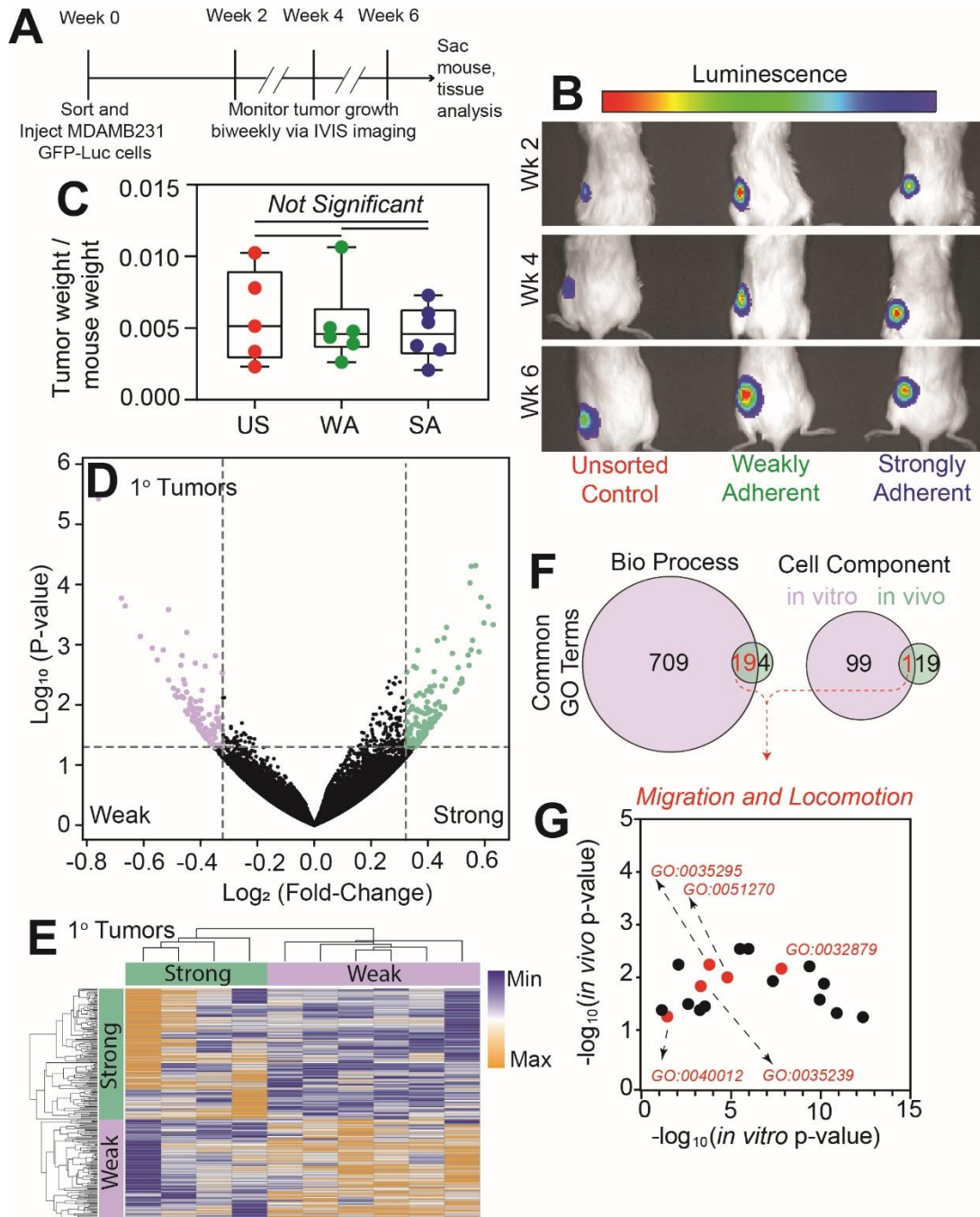
Figure 4.2: Primary tumors cluster based on adhesion phenotype of injected cells despite no difference in primary tumor size among groups

(A) Timeline of the lung metastases tumor study. (B) Representative IVIS imaging of mice injected with unsorted (US), weakly adherent (WA), or strongly adherent (SA) cells (left, middle, and right column, respectively) 2-, 4-, or 6-weeks post-injection (top, middle, and bottom rows, respectively). (C) Tumor to mouse weight ratio at time of sacrifice 6-weeks post injection (n=5, 6, and 6 for mice with unsorted, weakly adherent, and strongly adherent cells injected, respectively). (D) Differences in gene expression between WA and SA primary tumors are shown in a volcano plot (n=265 DEGs; 4 SA and 6 WA tumors). (E) Hierarchical clustering of differentially expressed genes (DEGs) between WA and SA cells. Vertical bars indicate clustering of genes that are upregulated in SA cells and WA cells (n=4 SA and 6 WA tumors). (F) Venn diagram of gene ontology (GO) terms associated with DEGs. (G) GO terms that are upregulated in WA tumors. Red terms indicate association with cell migration or locomotion. (C) Statistical analysis by one-way ANOVA with Tukey test for multiple comparisons.

To directly assess metastatic burden, we determined the number of GFP$^+$ lesions in lungs post resection. Mice receiving weakly adherent cells exhibited more metastases than those injected with strongly adherent cells or the unsorted parental line (Figure 4.3A-B); mice injected with strongly adherent cells consistently showed minimal metastatic activity, even after 8 weeks *in vivo*, in stark contrast to the broad range and greater average number of metastatic lung tumors in mice that received unsorted paternal or weakly adherent populations (Figure 4.3B, Supplemental Figure S4.9). Importantly, metastatic tumor size was not affected by pre-sorting on adhesion strength (Figure 4.3C), indicating that the fraction of cells disseminating, but not secondary tumor growth, differ with pre-injection adhesion sorting. Rather, differences may occur in the migration machinery of cells leaving the primary tumor, hence tumors composed of only strongly adherent cells are less likely to metastasize.
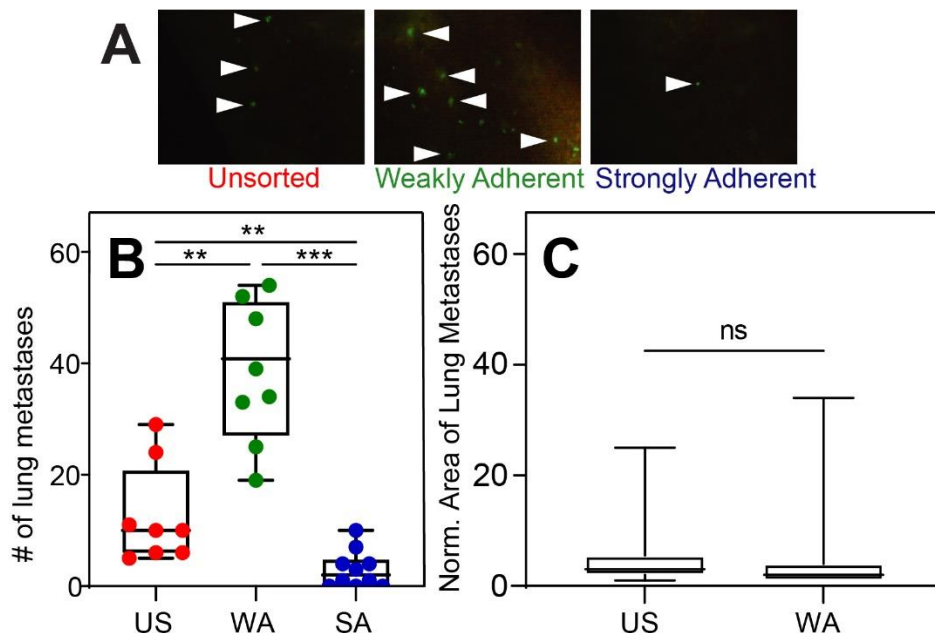
Figure 4.3: Mice injected with weakly adherent cells have more lung metastases
(A) Representative images of lung metastases from unsorted, weakly adherent, or strongly adherent cells (left, middle, and right column, respectively). (B) The number of lung metastases in mice injected with unsorted (US), weakly adherent (WA), or strongly adherent (SA) cells (n= 8, 8, and 10 for tumors composed of unsorted, WA, and SA cells, respectively). (C) Size of lung metastases (n=57 and 78 lesions analyzed for US and WA, respectively), excluding SA tumors given the low frequency of lesion formation. (B,C) Statistical analysis via (B) one-way ANOVA with Tukey test for multiple comparisons or (C) unpaired t-test. ** represents $p < 0.01$. *** represents $p < 0.001$. ns represents no significance.

4.3.3 Differences in metastatic and non-metastatic adhesion strength sort admixed populations

To determine if the inverse relationship between adhesion strength and metastatic propensity is not specific to MDA-MB-231 cells, adhesion strength of 8 other breast cancer and epithelial cell lines was measured using a divergent parallel plate flow chamber (dPPFC) where shear stress scales with chamber position (Supplemental Figure S4.10A-D). For each cell line, average adhesion strength, τ_{50}, was plotted against migration speed and displacement on hydrogels matched to breast tumor stiffness[248]. Cell lines that detached at τ_{50}<150 dyn/cm^2 have been largely characterized as metastatic[128,249,250] whereas those detaching at τ_{50}>150 dyn/cm^2 were derived from primary tumor or non-cancerous lines; thus, lower adhesion strength had a strong correlation with an increase in cell speed and displacement (Figure 4.4A-B), suggesting that an inverse relationship between adhesion strength and migration is not unique and that the dPPFC can measure parameters potentially important to outcomes.
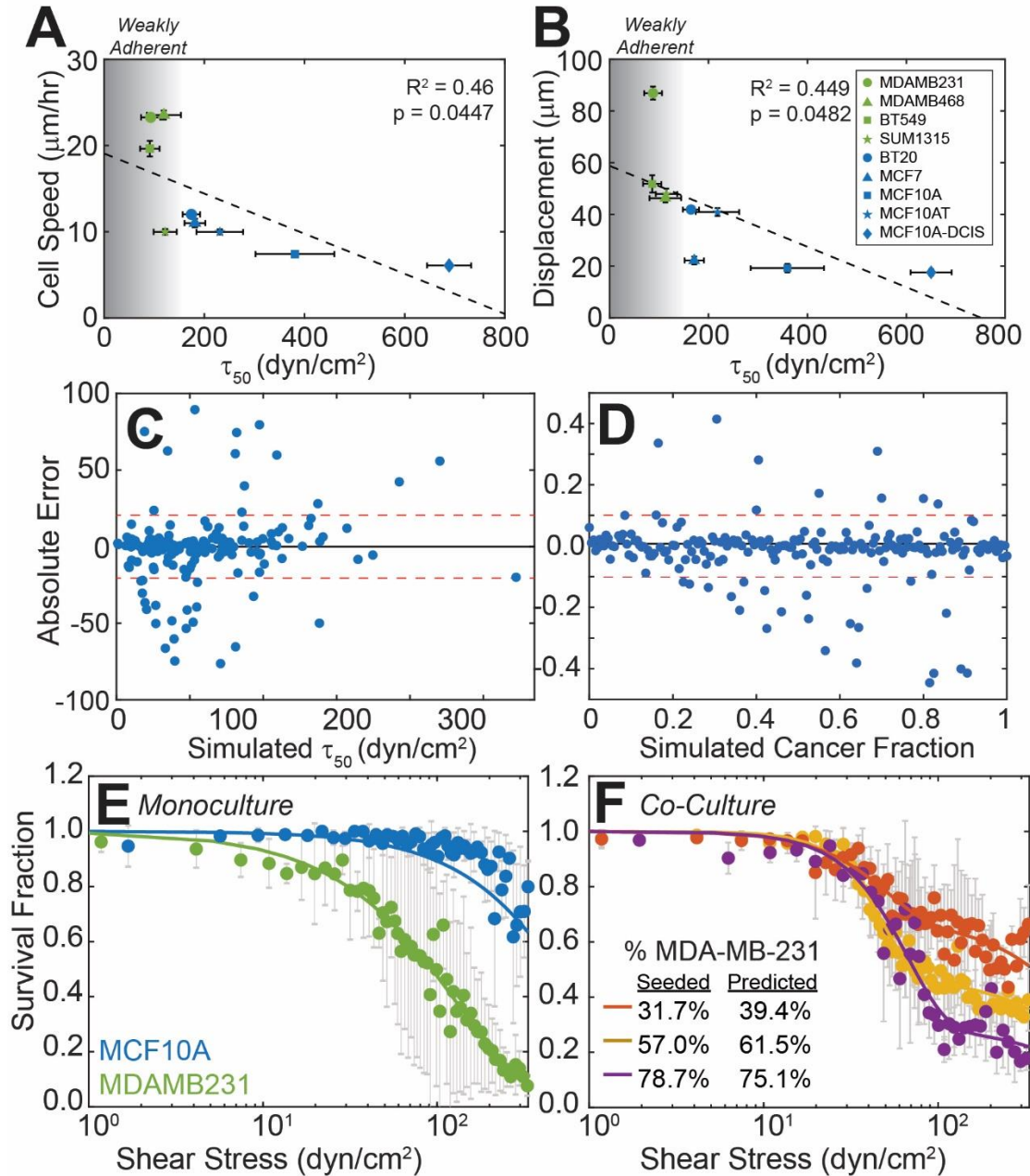
Figure 4.4: Cell line metastatic potential correlates with a decreased adhesion strength
(A) Cell speed and (B) displacement versus average shear stress of various metastatic (green) and non-metastatic cell lines (blue). Gradient represents shift from weakly adherent cells (gray) to strongly adherent cells (white). For cell speed and displacement, metastatic cell lines (green) had n = 553, 475, 137 and 306 cells analyzed for MDAMB231, MDAMB468, BT459, and SUM1315, respectively. For cell speed and displacement, non-metastatic cell lines (blue) had n = 609, 253, 253, 225, and 305 cells analyzed for BT20, MCF7, MCF10A, MCF10AT, and MCF10AT-DCIS, respectively. For adhesion strength, metastatic cell lines (green) had 13, 10, 13, and 12 replicates for MDAMB231, MDAMB468, BT459, and SUM1315, respectively. For adhesion strength, non-metastatic cell lines (blue) had 12, 10, 8, 9, and 9 replicates for BT20, MCF7, MCF10A, MCF10AT, and MCF10AT-DCIS, respectively. (C) The absolute error of simulated average shear stresses (n=192) and (D) simulated cancer fractions (n=196). (E) Shear stress plots of monocultured MCF10A (blue) and monocultured MDAMB231 (green) cells calculated using a divergent parallel plate flow chamber. (F) Shear stress plots of cocultured MCF10A and MDAMB231 cells (n>3 replicates). (E,F) Error bars denote the standard error of mean.

97

Since mouse and patient tumors are likely a mixed population of metastatic and non-metastatic cells, we developed a deconvolution method to distinguish adhesion profiles of two populations with different adhesion strengths. Using the parameters of a Weibull distribution to describe MDA-MB-231 and MCF10A adhesion profiles (see methods, λ and k from Equation 4.3), we simulated mixtures with varying adhesion strength to test the accuracy of the method's predictions of τ_{50} and cancer cell fraction in a virtual mixture. For monocultures, simulated populations randomly selected from Weibull distributions of MDA-MB-231 and MCF10A cells created adhesion profiles that matched experimental observations (Supplemental Figure S4.10E). For co-cultures simulated with pre-determined fractions of MCF10A and MDA-MB-231, we used a two population Weibull distribution to describe the overall obtained adhesion profile (see methods, Equation 4.5; Supplemental Figure S4.10F) based on the adhesion profiles of non-metastatic cells (e.g., MCF10A). We predicted the adhesion strength and metastatic cell fraction (e.g., MDA-MB-231, P_c) in the mixture and found that 80% of τ_{50} predictions for the metastatic population fell within ± 20 dyn/cm^2 and that 80% of predictions of the cancer fraction, P_c, i.e., the percentage of the population that is metastatic, fell within ± 0.06 of simulated values (Figure 4.4C-D). We validated mixtures experimentally by seeding MDA-MB-231 and MCF10A cells in ratios of 25:75, 50:50, and 75:25 into the dPPFC and measuring their combined adhesion profiles. The τ_{50} and cancer fraction were predicted using the same deconvolution method, and all cancer fractions were within $\pm 7.7\%$ and τ_{50} values were within ± 43 dyn/cm^2 of the measured monoculture values (Figure 4.4E-F). These results suggest that the dPPFC can accurately measure the cancer cell adhesion profile for heterogeneous populations without prior sorting.

4.3.4 Label-free assessment of stromal biopsies retrospectively predicts metastatic risk

To assess dPPFC functionality in predicting metastatic risk, we analyzed resected tumors, stroma, and contralateral fat pads from NSG mice. The adhesion profile of contralateral fat pads was used as the deconvolution standard to obtain the cancer fraction and τ_{50} of the stroma and tumor samples (Supplemental Figure S4.11A). Host cell adhesion strength from contralateral fat pads were ~3 fold higher than any of the cancer cells from the tumor or stroma samples (Supplemental Figure S4.11B). The number of GFP+ nodules observed in the lungs was inversely proportional to the τ_{50} measured from the tumor and stroma samples (Figure 4.5A and Supplemental Figure S4.11C). Only in the stroma was there a positive correlation with the estimated cancer fraction of the sample with GFP+ lung nodules (Figure 4.5B), whereas in the tumor biopsy there was less correlation (Supplemental Figure S4.11C). Next, we performed a ROC analysis to determine prediction accuracy for the cancer fraction and its τ_{50} for either high or low metastatic risk, defined as high risk if ≥2 GFP+ nodules were counted in the lungs. Classification accuracy was highest from stromal cancer fraction with an area under the curve (AUC) of 0.83 (Supplemental Figure S4.11D). However, by fitting the number of metastatic lesions, τ_{50}, and cancer fraction data with a logistic regression model, we generated probability estimates for ≥2 GFP+ nodules in lungs (Figure 4.5C and Supplemental Figure S4.11E-F). Stromal samples proved better at predicting risk, as the regression model for these data was the most statistically different from a constant model, determined by a deviance test (p=0.0167). We then used the probability estimates in the ROC analysis to evaluate how well the cancer fraction and its τ_{50} classify metastatic risk. Combining both metrics together improved prediction accuracy, increasing the AUC to 0.94 and specificity to 100% with a sensitivity of 85% (Figure 4.5D). Altogether, these data show that the dPPFC can detect cancer cells that have locally

invaded the surrounding stroma, and their quantity and adhesion mechanotype can be used to predict an increased rate of metastatic tumor formation.
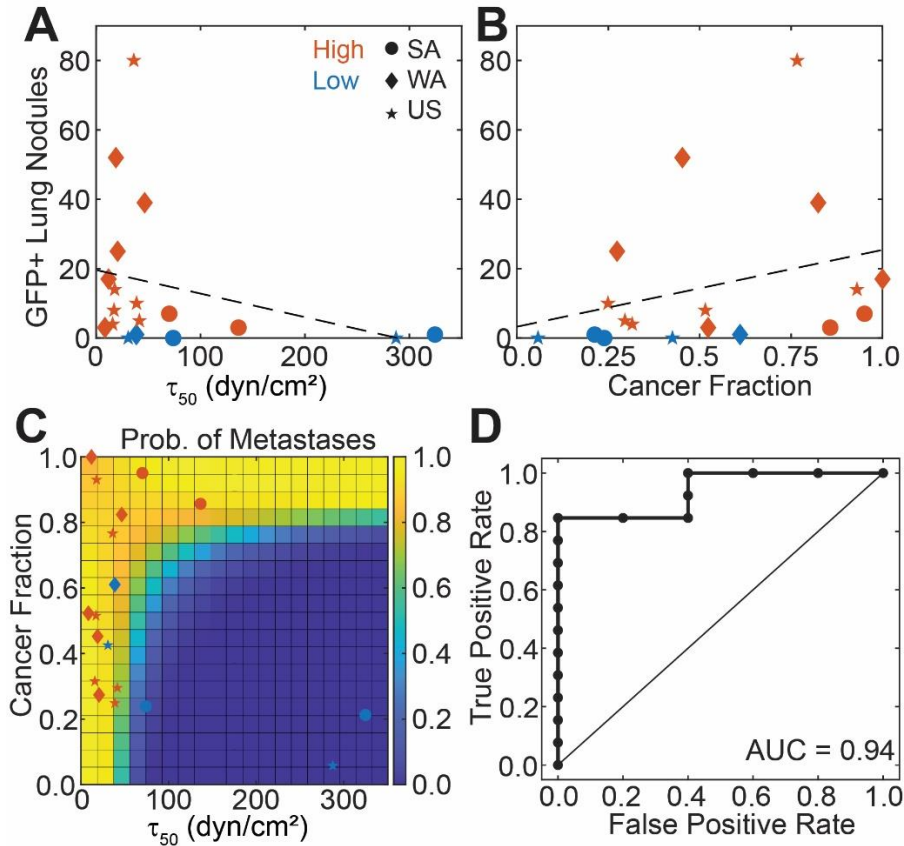
Figure 4.5: Average shear threshold of stroma surrounding the primary tumor predicts number of metastases in vivo
Tumors and surrounding stroma were dissected from mice injected with SA (circle), WA (diamond) or US (star) cells. (A) The average shear stress, and cancer fraction, P_c (B), as calculated from the combined adhesion profile of GFP+ cancer cells and mouse cells, plotted against the number of GFP+ lung nodules (n=20 lungs). (C) Logistic regression model showing probability estimate of a mouse having more than 1 tumor based on the average shear stress and cancer fraction measured from the dPPFC. (D) Receiver operating characteristics (ROC) curve of metastatic risk predictions based on model's probability estimates. Red points are classified as high metastatic risk and blue are low.

4.4 Discussion

Currently several independent parameters, e.g., tumor grade, stage, and subtype, are assessed histologically to help establish standard of care, but these data provide a far from complete assessment of tumor state and expected patient outcomes. Indeed, non-uniform distribution of genetic and phenotypic subpopulations within solid tumors causes many tumors of

similar histological grade to have vastly different metastatic potential, thus complicating existing prognostic assays[251–253]. Without more advanced detection methods, oncologists cannot provide the best recommendations for patients whose disease is marginal, low grade, or where consensus treatment options fail[237,238]. Notably, adhesion strength has emerged as a potential biophysical marker[123,144–149,246], but its links to cancer metastasis have only been demonstrated *in vitro* using surrogates, e.g. migration, velocity, and persistence[246]. Here, we showed that weak cellular adhesion correlates with increased metastatic risk *in vivo*, demonstrating possible clinical relevance of adhesion strength as a prognostic marker. Furthermore, our divergent parallel plate flow chamber (dPPFC) can be used as a label-free assay to accurately measure the adhesion profile and cancer cell frequency in tumor and stromal biopsies, and this measure may better assess clinical outcomes than standard methods.

The dPPFC appears to have several key advantages to other emerging or recently FDA-approved devices. While other methods surveil CTCs in liquid biopsies via single markers to detect cancer cells that have intravasated into the blood stream[254–258], many have been unable to accurately predict disease severity or increase patient survival. Often, disease may have already progressed, be hindered by intravasating cell heterogeneity[259–261], signal substantially diluted as CTC clear quickly from the bloodstream[262], or cells may disseminate after assessment due to significant tumor dormancy[242]. These considerations result in lower single marker assay specificity, sensitivity, and AUC[263] versus stromal-based physical assays[90,128,141,243,264,265]. While biomarker assays have also moved from single to multigene prognostic analyses (i.e., 21 to 70 genes)[266,267], even their prediction accuracy has remained less[268] than reported here or for other physical assays. Conversely, many physical assays have been benchmarked against large panels of normal epithelial, cancer, and transgenic cell lines that demonstrate predictive capabilities

when assessing metastatic potential. When distinguishing between these physical assays, the dPPFC may be faster and more robust owing to short interrogation time (minutes) versus channel confinement assays (hours)[128,243]. Confinement assays also require significant microfabrication and are single-use devices; dPPFC consumables are only the underlying standard-sized microscope slide. With multi-channel designs, dPPFC can still be used in moderate throughput to evaluate potential therapeutics. It also only requires $5x10^3$ cells to achieve an AUC of 0.94, which is an order of magnitude fewer cells than reported in other assays[128,243] with comparable sensitivity and specificity.

Relative to other physical markers, adhesion may be a more robust i*n vivo* indicator of metastatic disease. First, GPF+ cells that disseminated to the stroma were less adhesive, and when cells were pre-sorted to create tumors of a single adhesive mechanotype, strongly adherent cells often resulted in no or almost no GFP+ lesions in the lungs of injected NSG mice. RNA sequencing of these sorted cell types showed that cells in primary tumors up to 6 weeks *in vivo* maintained pre-injection differences[246]. Genes associated with weakly adherent cells corresponded to cell migration and locomotion, which is associated with shorter disease-free intervals in The Cancer Genome Atlas (TCGA)[246] and could constitute the gene signature of the adhesive mechanotype. Notably, our dPPFC detect and quantify cells with this adhesion mechanotype, which appears to directly correlate with metastatic tumor formation. These observations also suggest that a pharmacological strategy that alters the mechanotype of a disseminating cell, perhaps via changes to its transcriptome, could render it less metastatic.

Despite the broad implications of these findings, it is important to note ongoing limitations to dPPFC and other physical assays. First, patients often have tumors resected and then monitored for secondary disease without the primary tumor being present. Our model here

primarily involved tumor progression for 6 weeks without resection; results may reflect higher than normal metastatic burden relative to patients receiving standard of care. Second, patients are typically treated with a combination of doxorubicin hydrochloride (Adriamycin) and Cyclophosphamide followed by paclitaxel (Taxol), i.e., AC-T therapy[269], which may alter the adhesion mechanotype of disseminating cells. However, the perivascular niche can protect chemoresistant disseminating tumor cells[270], so despite treatment, the adhesive mechanotype may remain intact; indeed, only when combined with integrin function blocking antibodies was there significant sensitization to chemotherapy. Third, we assayed tumors from NSG mice, but the presence of immune cells could complicate disseminating cell signaling and dormancy; prolonged inflammation via neutrophil infiltration can awaken dormant cancer cells by cleaving extracellular matrix, activating integrins[271], and potentially changing adhesion mechanotype. While these concerns are important, we believe that the data shown here supports further *ex vivo* assessment of human samples using the dPPFC to predict the metastatic risk to the patient. Succinctly, our results suggest that adhesion strength and cancer fraction are two label-free metrics of the device that can serve as markers of metastatic potential and be utilized in a prognostic fashion to screen patient samples.

4.5 Methods

4.5.1 Cell culture

Cell lines were cultured according to media conditions in Supplemental Table S4.2. Products were purchased from Life Technologies. Cells were obtained from ATCC (authenticated by morphology, growth curve, and isoenzyme analysis) and verified mycoplasma free via PCR.

4.5.2 Creating GFP and luciferase-expressing MDA-MB 231 cells and validating adhesion heterogeneity

To make lentivirus particles, HEK293T were seeded into a 20 cm dish in high glucose DMEM supplemented with 10% FBS and 1% antibiotic/antimycotic. Cells were allowed to grow until 70% confluence. At this time, 3 μg of pMD2.G (Addgene 12259), 12 μg of pCMV deltaR8.2 (Addgene 12263), and 9 μg of either GFP or luciferase plasmid (generous gift of the Kun-Liang Guan lab) was added to 1.5 mL Opti-MEM. Separately, 36 μL of Lipofectectamine 2000 was added to 1.5 mL Opti-MEM. After incubating the solutions for 15 minutes, the solutions were mixed and allowed to incubate for an additional 30 minutes. The mixture was then added dropwise to HEK293T cells. After 48 hours, media was harvested and replaced. After an additional 24 hours, media was harvested again and all media was concentrated using an Amicon Ultra-15 ultrafilter (100,000 NMWL cutoff) to a final volume of 1 mL, which was aliquoted into 250 μL aliquots and frozen at -80°C.

Media with packaged lentiviral particles was added to cultured MDA-MB231 cells along with 8 μg/mL of polybrene. After 24 hours, the media was aspirated and replaced with normal culture media. Upon observation of GFP expression through fluorescence microscopy, the cultured cells were treated with 2 μg/mL of puromycin in culture media and cultured for two days. The remaining cells were sorted with a Becton Dickinson FACSAria II for presence of GFP, with unstained cells as a negative control to establish a gating strategy. All data was analyzed by FlowJo software. GFP expression was validated via fluorescence microscopy using a Nikon Eclipse Ti-S microscope at 10X magnification with FITC.

To validate that adhesion heterogeneity is maintained post-transduction, weakly and strongly adherent subpopulations were isolated by exposure to pre-determined low and high

shear stresses, respectively, in a microfluidic flow chamber as previously described[1]. Weakly and strongly adherent cell fractions were seeded onto 2.4 mg/mL Type I collagen gels (Corning) and imaged with a Nikon Eclipse Ti-S microscope equipped with a temperature- and CO2-controlled stage for 24 hours, after which their migration was tracked and analyzed using a custom MATLAB script. Cells that divided or did not remain in the frame for 24 hours were not tracked.

4.5.3 Isolation of MDA-MB 231 cells in tumor and surrounding stroma

All animal care and experiments were approved by the Institutional Animal Care and Use Committee of the University of California, San Diego (study #S11102). 10^6 MDA-MB 231 cells, expressing GFP and Luciferase, were suspended in 40 µL of Matrigel-PBS (1:1) mixture and were injected bilaterally into the inguinal mammary fat pads of 11-week-old female NOD/SCIDγ mice. Tumor growth was monitored at 2-week intervals and the mice were sacrificed at 6 weeks post-injection. Mice were dissected and the fat pads were surgically removed. Using an inverted fluorescent microscope, the stiffened tumor bolus was manually separated from the surrounding stroma. Both tumor and stroma were finely minced then treated with Accumax and placed on a shaker at room temperature for 2 hours. Cells were then pipetted through a 70 µm cell strainer and neutralized with culture media. For spinning disk assay cells were centrifuged and resuspended in FACS buffer (2% goat serum, 5 mM EDTA in PBS), and GFP-positive cells in tumor and stroma sections were sorted via FACS.

4.5.4 Spinning disk assay for quantification of cellular adhesion strength

GFP-positive MDA-MB231 cells from tumor and stroma fractions were seeded onto 25 mm glass coverslips—coated with 2 µg/mL of fibronectin and blocked with 5% bovine serum albumin—and incubated overnight at 37°C. Cells were then exposed to shear stress at varying RPMs using the spinning disk shear assay as previously described[2]. Cells were immediately

fixed in 3.7% formaldehyde for 10 minutes, after which they were stained with 1:2000 Hoechst in DI water. Quantification of cellular adhesion strength was performed as previously described[123].

4.5.5 Sorting of MDA-MB 231 cells and injection into mice for lung metastases study

GFP+ Luc+ MDA-MB 231 cells were seeded (~5000 cells/cm^2) overnight onto fibronectin-coated glass slides. Using the parallel-plate flow chamber, the slides were exposed to 15 dynes/cm^2 shear stress for 2 minutes to collect the weakly adherent cell fraction. Subsequently, the slides were exposed to 60 dyn/cm^2 shear stress for 2 minutes. Any cells that remained on the slide were removed via 0.25% trypsin and collected as the strongly adherent cell fraction. The weakly adherent and strongly adherent cell fractions were cultured separately for 48 hours, as well as a perfused but unsorted control population. 10^6 GFP and Luciferase expressing MDA-MB 231 cells from the strongly adherent fraction, weakly adherent fraction, or the unsorted control were suspended in 40 μL of Matrigel-PBS (1:1) mixture and were injected into the inguinal mammary fat pad of 11-week-old female NOD/SCIDγ mice. Tumor growth was monitored at 2-week intervals and the mice were sacrificed at 6 weeks post-injection. 6 weeks was chosen as the length of the study because few metastatic tumors were seen at 4 weeks (Supplemental Figure S4.9A), but the lungs were saturated with metastases at 8 weeks (Supplemental Figure S4.9B-C). At time of sacrifice, the lungs and primary tumors were harvested, frozen in optimal cutting temperature compound, and stored at -80ºC. Prior to freezing, the lungs were imaged using a GFP filter on a microscope to quantify the number of metastatic tumors.

4.5.6 RNA sequencing

Tumors were dissociated, and the resulting RNA purified using Qiagen RNeasy Mini Kit.

RNA quality was quantified and assessed using TapeStation (Agilent), RNA libraries were prepared using the Illumina TruSeq Stranded RNA, High Throughput Library Prep Kit. RNA was sequenced using the Illumina HiSeq 4000 system to generate 50 bp single-end reads. Data was analyzed using Rosalind, with a HyperScale architecture developed by OnRamp Bioenformatics, Inc. Reads were trimmed using cutadapt[173] and quality scores were assessed using FastQC[272]. Reads were aligned to the Homo Sapien genome build hg19 using STAR[175], while individual sample reads were quantified using HTseq and normalized via relative log expression using DESeq2 R library[176]. DESeq2 was also used to calculate fold-changes. Clustering for the differentially expressed gene heatmap was performed via the Partitioning Around Medoids method with the fpc R library[273]. Functional enrichment analysis of gene ontology was done using HOMER[180]. GO terms were assigned based on PANTHER pathways.

4.5.7 Quantification of lung metastases sizes

Images of lung metastases obtained from the GFP microscope were quantified using the ImageJ Particle Analysis plug-in. Briefly, a constant binary threshold was applied to each image to identify each incidence of a metastasis, the pixel area of each metastasis was recorded, and the sizes were normalized to the smallest metastasis recorded.

4.5.8 Validation of divergent parallel plate flow chamber design

The divergent parallel plate is based off of the linear shear stress flow chamber from Usami and co-workers[125], and designed using Solidworks. The width of the chamber was profiled so that it becomes increasingly wider along the length of the chamber so that shear stress in the device decreases exponentially, with the profile of the side walls varying according to,

$$w = w_{min}e^{\left(\frac{\ln(10)}{L_{max}}L\right)} \tag{4.1}$$

where L is the position along the channel, w_{min} is the narrowest part of the channel, L_{max} is the

length between the widest and narrowest points of the channel. The wall shear stress can then be

calculated at any point inside the device according to,

$$\tau = \frac{6Q\mu}{wh^2} \tag{4.2}$$

where Q, μ, and h are flow rate, viscosity, and channel height respectively. The V-shaped outlet

of the channel allows the shear stress to continue to decrease to zero from where the channel is

widest (Supplemental Figure S4.10C). Wall shear stress along the length of the chamber was

validated by finite element analysis using COMSOL Multiphysics and agreed with values

determined from equation 4.2 and shown in Supplemental Figure S4.10C.

The flow chamber was fabricated out of polycarbonate (McMaster-Carr, 8707K173). The

channel was made by cutting the divergent profile in 127µm thick silicone gasket (SMI) using a

craft cutter (Silhouette Cameo 4). A pocket was made out of 1 mm thick adhesive backed

silicone rubber (McMaster-Carr, 5787T115) to align a 25x75 mm glass slide against the gasket.

The slide was then clamped down onto the gasket by a second polycarbonate plate by screwing it

into the base plate.

4.5.9 Shear threshold quantification of mammary epithelial cancer cell lines

The cell lines used to quantify shear threshold are listed in Supplemental Table S4.2,

consisting of a mix of mammary cancer or epithelial origin. ~3000 cells/cm^2 were seeded onto

25x75 mm glass slides coated with 2 µg/cm^2 of human fibronectin and allowed to adhere

overnight. Before imaging, cells were stain with Hoechst 33342 (ThermoFisher, H3570) for 10

minutes prior to imaging, and then assembled in the divergent parallel flow plate chamber. A

2.1x45mm region within the chamber was scanned using a Nikon Eclipse Ti-S confocal

microscope at 10x in both phase and DAPI channels to count the number of cells in the chamber

before shearing. The device was then connected to a syringe pump with the flow rate set to obtain a maximum shear of either 330 or 660 dyn/cm^2. 4.5 g/L of dextrose in PBS without magnesium and calcium was used to shear cells for 3 minutes, before returning the device to the microscope to image and count the remaining cells.

The adhesion profiles for each cell line were determined by dividing the imaged region into 61 equal sized bins (775µm) and plotting the shear at the center of each bin versus the fraction of cells remaining after shearing. Using MATLAB's curve fitting toolbox, the curve of the adhesion profile was then fit to these points using the following equation,

$$S = e^{-\left(\frac{\tau}{\lambda}\right)^k} \tag{4.3}$$

where τ is the shear along the chamber, and λ and k are the scale and shape parameters of the Weibull distribution. The τ_{50}, or the shear stress at which 50% of the cells detach can then be calculated according to,

$$\tau_{50} = \lambda(-\ln(0.5))^{1/k} \tag{4.4}$$

Co-culture experiments were performed similarly, with a 25:75, 50:50, or 75:25 mixture of MDA-MB-231 and MCF10A cells seeded at a total ~3000 cells/cm^2. To predict the percentage and τ_{50} of the MDA-MB-231 cells in the mixture, the adhesion profile of the combined cell types was fit to,

$$S = P_c e^{-\left(\frac{\tau}{\lambda}\right)^k} + (1 - P_c)e^{-\left(\frac{\tau}{\lambda_{10A}}\right)^{k_{10A}}} \tag{4.5}$$

Using the known values for λ_{10A} and k_{10A} from the adhesion profile MCF10A cell line, the fraction of MDA-MB-231 cells, P_c, and their λ and k can be predicted from the curve fit.

4.5.10 Cell speed and displacement measurements

Cell speed and displacement was measured using timelapse microscopy on cells

migrating on 3.2kPa polyacrylamide gels. The Young's modulus of the gel was validated using

atomic force microscopy. Prior to seeding the cells, the surface of the gels was functionalized

with collagen I (150 µg/ml) using sulfosuccinimidyl 6-(4'-azido-2′-nitrophenylamino)hexanoate

(0.2 mg/ml, Sulfo-SANPAH; Pierce) as a crosslinker to the PA, and allowed to incubate at 37C

overnight. Cells were seeded at ~1500 cells/well and allowed to adhere to the PA gels overnight.

The cells were then imaged for 15 hours using a Nikon Eclipse Ti-S microscope equipped with a

temperature and CO2 controller (Pathology Devices Inc., LiveCell). Images were taken every 5

minutes using phase contrast at 10x. The cell trajectories were then traced using a custom

MATLAB script, and dividing cells were excluded in the analysis. Cell speed was calculated by

dividing the path length by the 15-hour runtime and displacement by finding the distance

between the starting and ending position of the cell.

4.5.11 Dissociation and adhesion quantification of tumor, stroma, and mammary fat pad

Tumor, stroma, and the tissue from the contralateral fat pad were resected from mice

sacrificed at 6 weeks post GFP+ Luc+ MDA-MB 231 cell injection. The tumor and stroma were

separated as described above. All tissues were finely minced and the cells were dissociated in a

collagenase solution comprised of 2mg/ml trypsin, 2mg/ml trypsin, 5% FBS, 50µg/ml

gentamicin, 5µg/ml insulin, and DMEM/F12, as described previously[274]. GFP+ cells from the

tumor were not FAC sorted to better recapitulate tumor samples obtain from a patient biopsy,

and test the flow chamber's ability to distinguish between cancer and healthy cells. All of the

dissociated mouse and cancer cells were then seeded and allowed to grow in a 6 well plate, for 2-

3 days or until there were enough for seeding onto 25x75mm FN coated glass slides. The cells

were then sheared in the flow chamber and the adhesion profile for each sample was determined

as described above. Tumor and stroma adhesion profiles were fit to equation 4.5 to predict the

τ_{50} and percentage of cancer cells in these samples, using the λ and k values measured from the adhesion profile of the contralateral fat pad in place of those from the MCF10A cells.

4.5.12 Logistic regression model and receiver operating characteristic (ROC) analysis

Metastatic risk was defined as either high or low by a threshold number of GFP+ lung nodules. For the stroma samples, using a threshold of 2 nodules, and comparing the τ_{50} and cancer fractions of mice with nodule counts above and below that threshold, gave us the most significant difference by a Wilcoxon rank sum test between the two groups. The binary response variable was then defined as low risk for mice with 1 or fewer GFP+ lung nodules and high risk for mice with more than 1 GFP+ lung nodule. A logistic linear regression model was then fit to obtain the probability estimates of having more than 1 tumor based on the following equation,

$$p = logit(y) = a + b\tau_{50} + cP_c + d\tau_{50}P_c \tag{4.6}$$

where a, b, c, and d are the estimated coefficients from MATLAB's generalized linear regression model, and τ_{50} and P_c are the median detachment shear and cancer fraction respectively. A deviance test was used to compare whether the model differs significantly from a constant model. The probability estimates from the model were then used as the classifier scores for obtaining the ROC curve and area under the curve (AUC) using MATLAB's perfcurve function.

4.5.13 Statistical analysis

For all analyses, *, $p < 0.05$; **, $p < 0.01$; ***, $p < 0.001$; and ****, $p < 0.0001$. Figures 4.1B-D, S4.6C, and 4.3C were performed using two-tailed unpaired t test. Figure 4.2C and 4.3B was analyzed using a one-way ANOVA with Tukey test for multiple comparisons. Data expressed as box-and-whisker plots show all points with the whisker ends corresponding to minimum and maximum values. All other values are expressed as mean ± SD. Statistical

analyses were performed using GraphPad Prism Software v9.0.

4.6 Supplementary Information
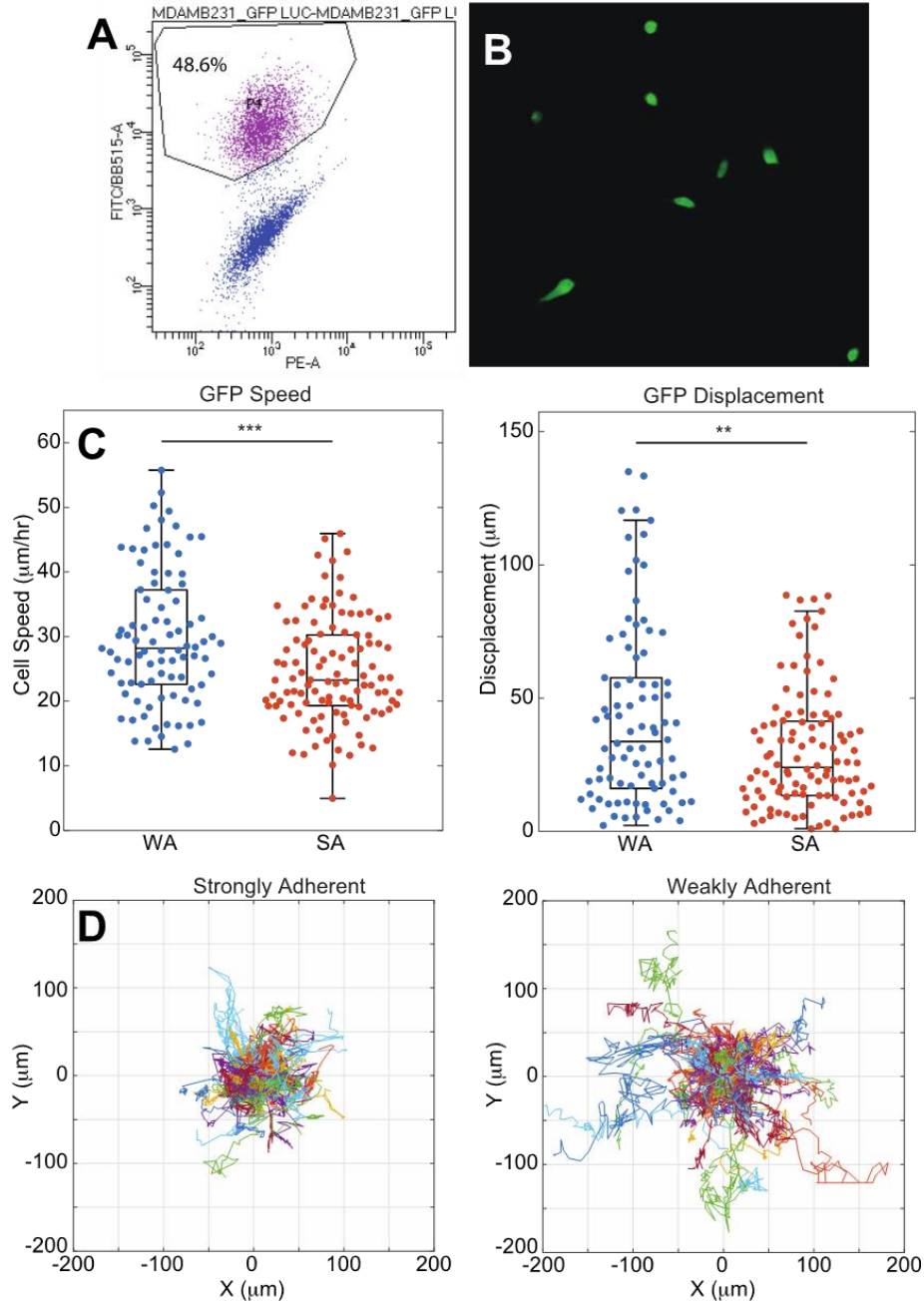
Supplemental Figure S4.6: GFP-Luciferase lentiviral transduction does not alter inherent heterogeneity of MDA-MB231 cells
(A) After treatment with puromycin to select for cells that expressed Luciferase, cells were sorted using FACS for GFP+ signal (y-axis). Gating strategy is based on excluding cells from an unlabeled control sample. (B) GFP expression was verified using fluorescence microscopy. (C, D) Weakly adherent cells were more migratory than their strongly adherent counterparts, consistent with previous findings. (n=89 and 111 for weakly and strongly adherent, respectively). (C) Statistical analysis via unpaired t-test. ** represents p<0.01. *** represents p<0.001.
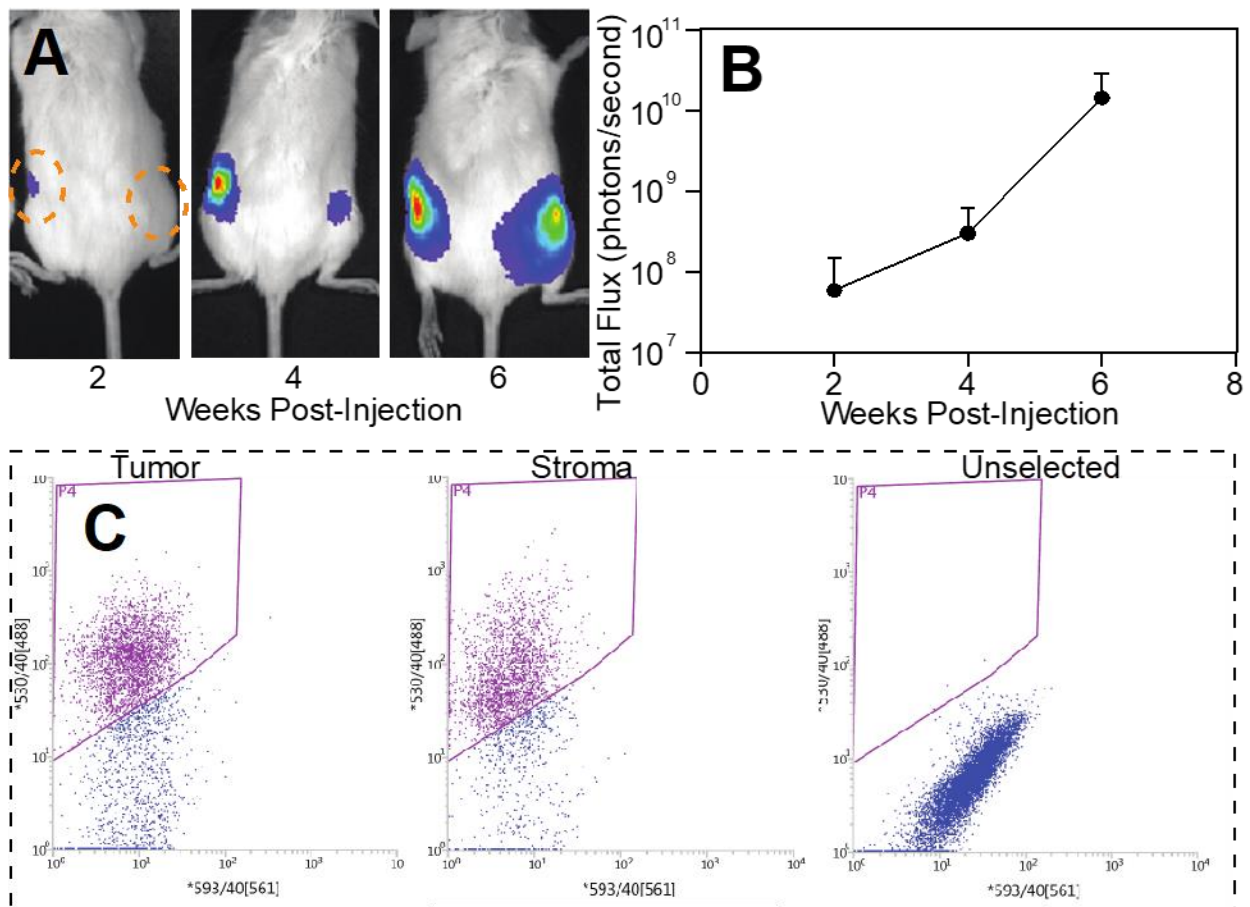
Supplemental Figure S4.7: Tumor growth was monitored using IVIS and GFP+ cells can be sorted from tumor and stroma

(A) Tumor growth was monitored using IVIS at 2-week intervals using (B) total flux as a measurement (n=6 mice). (C) After manual separation of the stiff tumor from the surrounding stroma and dissociation into single cells, GFP+ cells (y-axis) could be isolated from both tissue fractions using FACS.

20 ml/min   90 ml/min

0 10 20 30 40 50 60
Wall Shear Stress (dyn/cm²)
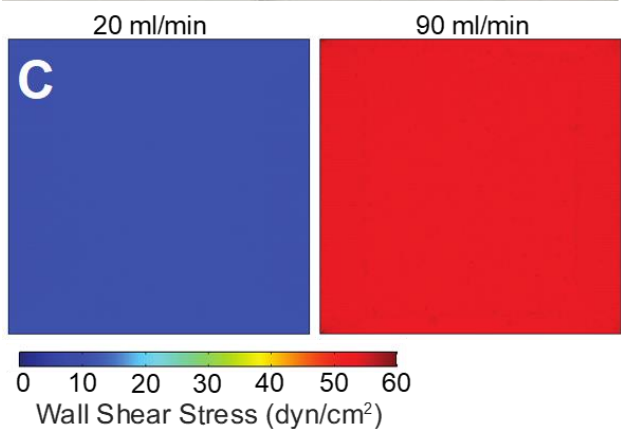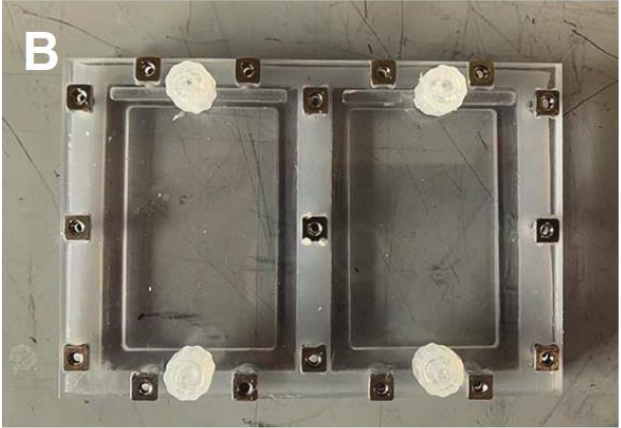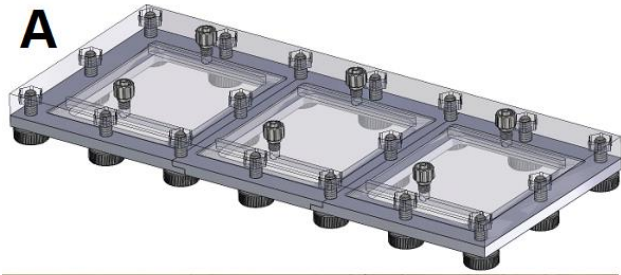
Supplemental Figure S4.8: Parallel plate flow chamber applies a uniform shear stress to cells seeded in the device
(A) SolidWorks design and (B) top-down view of a straight walled parallel plate flow chamber (PPFC). (C) COMSOL simulation of the shear stress profile through the straight-walled parallel plate flow chamber (PPFC).

	Unsorted Control	Weakly Adherent	Strongly Adherent
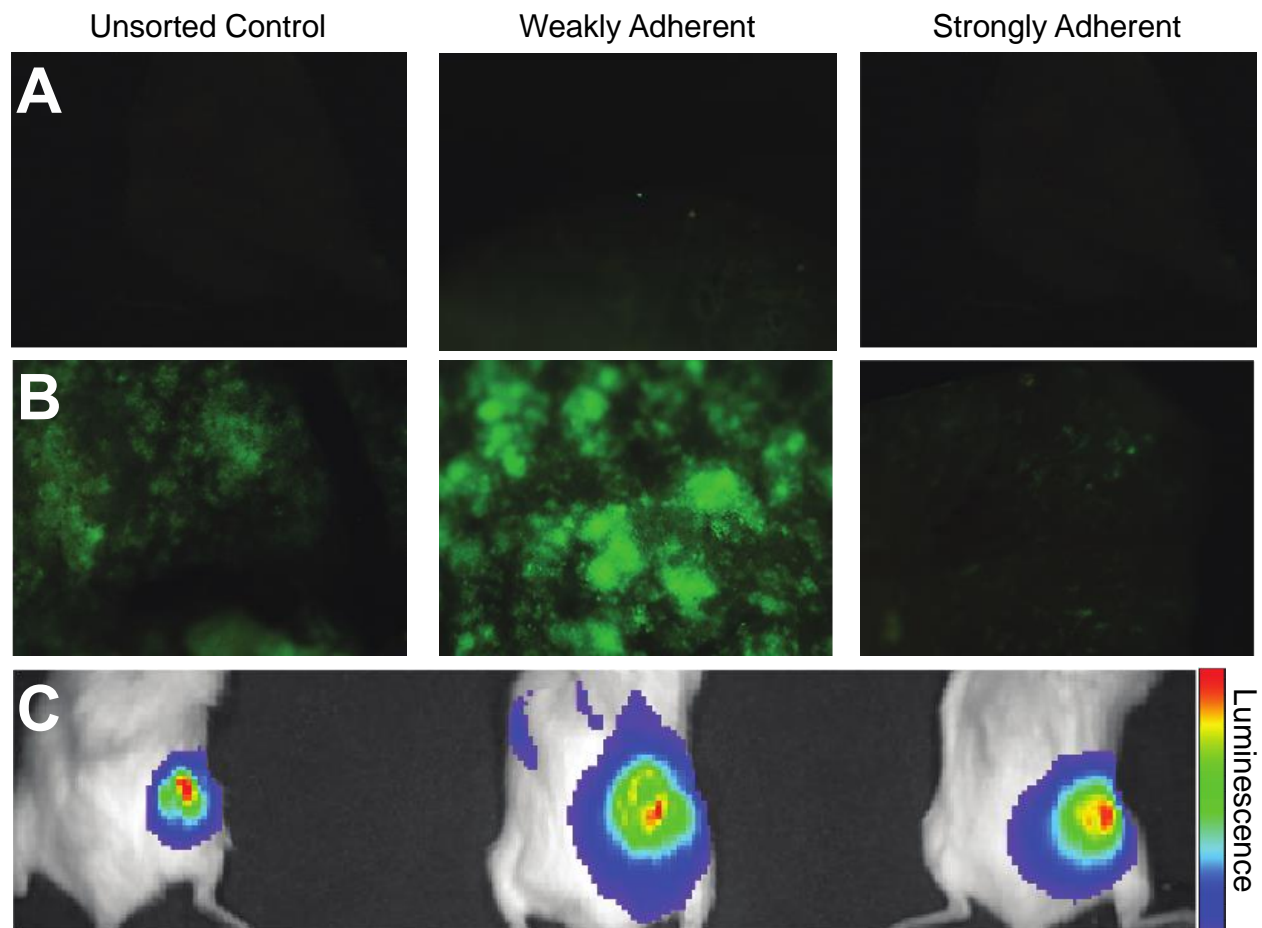
Supplemental Figure S4.9: Few lung metastases were seen 4 weeks post-injection, but lungs were saturated with metastases 8 weeks post-injection
Representative images of GFP+ lung metastases in mice sacrificed (A) 4 weeks or (B) 8 weeks post-injection. (B) Representative IVIS image of mice 8 weeks post-injection.
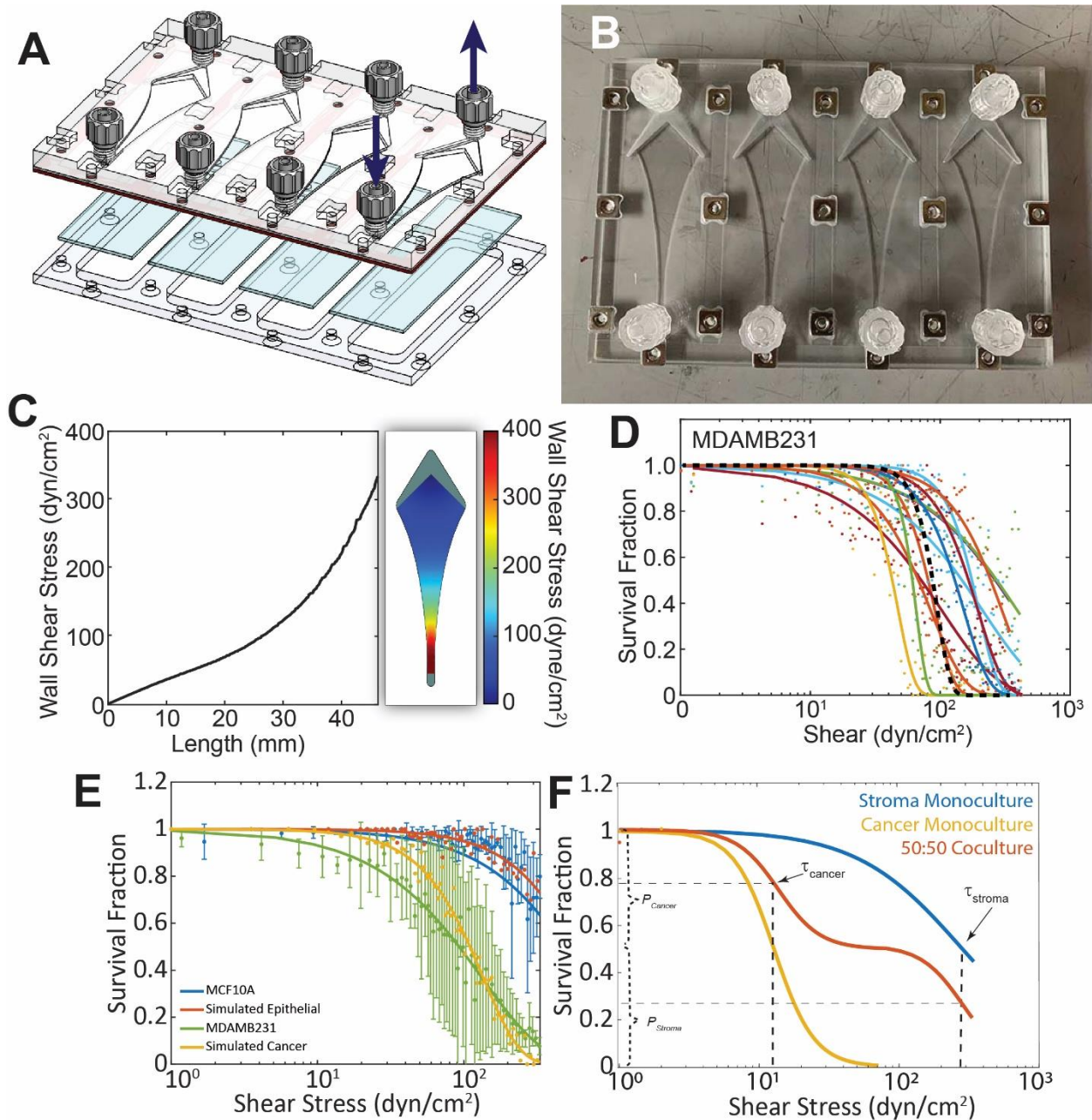
Supplemental Figure S4.10: Divergent parallel plate flow chamber applies an increasing shear stress to cells seeded in the device

(A) SolidWorks design, (B) top-down view, and (C) COMSOL simulation of the shear stress profile through the imaging, divergent parallel plate flow chamber (dPPFC). (D) Percent of attached cells versus shear stress value in the imaging PPFC for various replicates of perfusion of MDAMB231 cells. Black dashed line represents the average shear stress plot of the replicates (n=12 replicates; >500 cells/replicate). (E) Comparison of statistically generated adhesion profiles and experimental adhesion profiles (n=3 replicates/cell line). (F) Schematic of adhesion profile to highlight how cancer fraction, P_c, and adhesion strength are plotted on an adhesion metric with the dPPFC; dashed lines indicate P_{cancer} and P_{stroma} and darker dashed lines represent media cell adhesion strength for a given population.

116
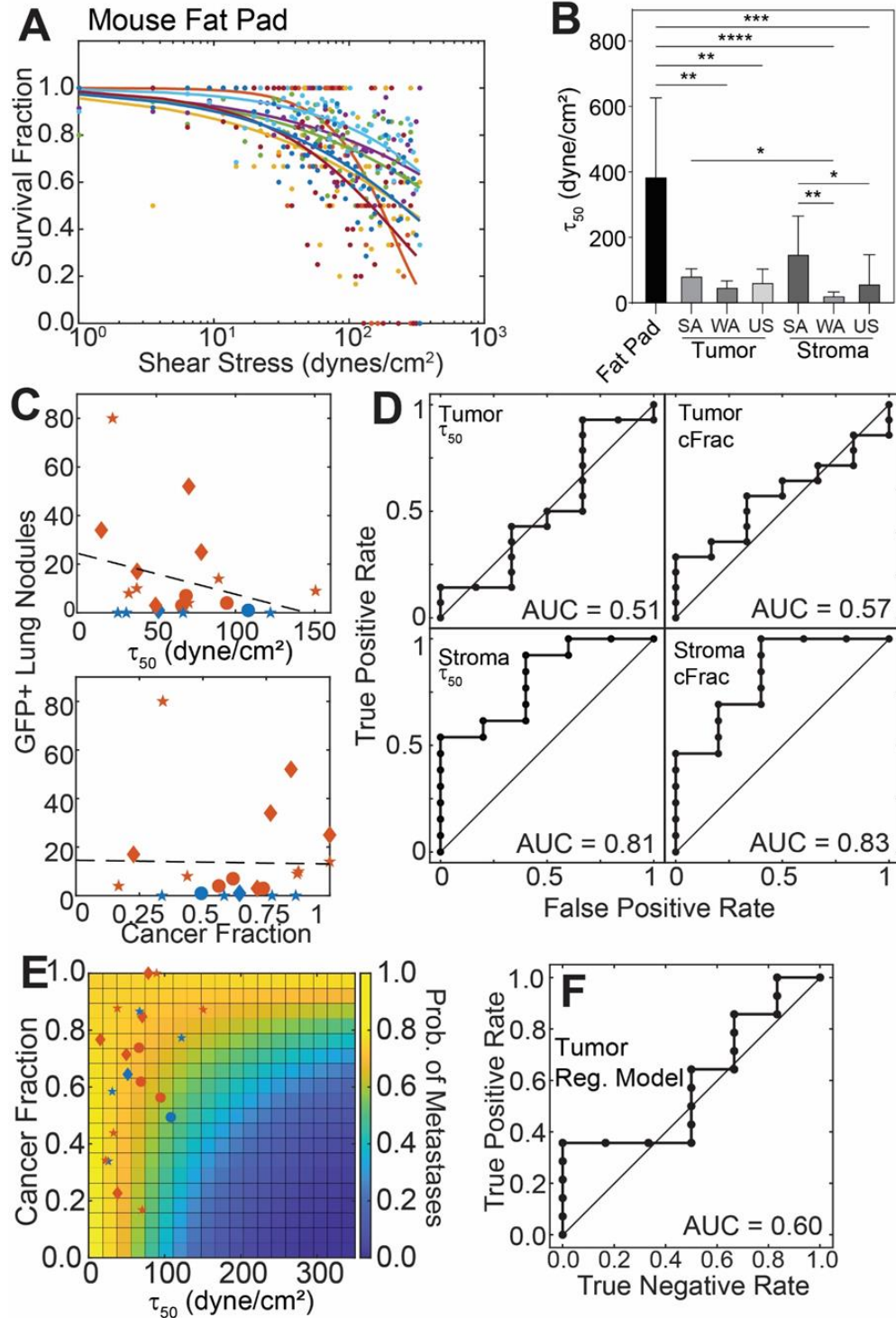
Supplemental Figure S4.11: Raw data from mammary epithelial cancer adhesion assays
(A) Shear plots of replicates of cells dissociated from the contralateral mammary fat pad (n=7 mice). (B) Average shear stress of cells dissociated from the contralateral mammary fat pads, tumors, and surrounding stroma (n=7 mice/condition). (C) Average shear stress and cancer fraction vs. GFP+ lung nodules from resected tumor samples (n=20 lungs). (D) ROC curves of metastatic risk predictions for average shear stress or cancer fraction for resected tumor and stroma samples. (E) Logistic regression model showing probability estimate of a mouse having ≥2 tumor based on the average shear stress and cancer fraction for tumor sample. (F) ROC curve of metastatic risk predictions based on model's probability estimates. Red points are classified as high metastatic risk and blue are low.

117

Supplemental Table S4.1: Intersection of migration and locomotion GO terms between primary tumors and pre-sorted cells
Top GO terms (as assigned by Panther) between in vitro and in vivo primary tumors and their corresponding p-Values as plotted in Figure 2F. Data is ordered by in vivo p-value.

GO Term	In Vivo GO p-Val	In Vitro GO p-Val
anatomical structure morphogenesis (GO:0009653)	1.310	12.740
animal organ development (GO:0048513)	1.344	11.197
anatomical structure formation involved in morphogenesis (GO:0048646)	1.367	3.939
tube development (GO:0035295)	1.371	1.440
system development (GO:0048731)	1.372	3.359
regulation of multicellular organismal process (GO:0051239)	1.374	2.943
regulation of localization (GO:0032879)	1.385	1.609
regulation of cellular component movement (GO:0051270)	1.554	10.383
tube morphogenesis (GO:0035239)	1.879	10.481
multicellular organism development (GO:0007275)	1.936	7.575
multicellular organismal process (GO:0032501)	2.000	3.335
anatomical structure development (GO:0048856)	2.048	4.967
regulation of locomotion (GO:0040012)	2.056	7.939
blood vessel morphogenesis (GO:0048514)	2.204	4.228
tissue development (GO:0009888)	2.230	9.801
developmental process (GO:0032502)	2.302	3.757
regulation of cellular process (GO:0050794)	2.389	2.326
regulation of biological process (GO:0050789)	2.437	5.783
biological regulation (GO:0065007)	2.438	5.572

Supplemental Table S4.2: Cell line culture conditions
Media formulation for each cell line. Note the following abbreviations: Dulbecco's Modified Eagle Medium (DMEM), fetal bovine serum (FBS), penicillin/streptomycin (P/S), hEGF, and horse serum (HS).

Cell Line	Media
MDAMB-231	DMEM + 10% FBS + 1% P/S
MDAMB-468	
BT20	
MCF-7	DMEM + 10% FBS + 1% P/S + 10 ug/mL insulin
BT549	DMEM + 10% FBS + 1% P/S + 1ug/mL insulin
SUM1315	DMEM/F-12 + 5% FBS + 1% P/S + 5ug/mL hEGF, 5ug/mL insulin
MCF10AT	Growth media: DMEM/F-12 + 5% HS + 0.5 ug/mL hydrocortisone, 20 ng/mL hEGF, 10 ug/mL Insulin, 100 ng/mL cholera toxin + 1% P/S
MCF10A-DCIS	
MCF10A	Resuspension media: DMEM/F-12 + 20% HS + 1% P/S

4.7 Acknowledgements

Chapter 4, in full, has been submitted for publication of the material as it may appear in Birmingham, K., Yeoman, B., Beri, P., Tuler, J., Williams, I., Kumar, A., Klein, S., Katira, P., and Engler, A.J. "Stromal Cell Adhesion Predicts Severity of Metastatic Disease." *Nature Biomedical Engineering*, 2022. The dissertation author was a primary author and equal contributor in the authorship of this paper.

CHAPTER 5. CONCLUSIONS

5.1 Weakly Adherent Cells Exhibit Greater Metastatic Potential

Epithelial cancers display a significant degree of heterogeneity in metastatic capability between the cells that comprise them. This results in a more aggressive subset within the population to be more likely to disseminate from the primary tumor. In chapters 2 and 3, we explored how the weakly adherent fraction of cancer cells presented characteristics *in vitro* indicative of having a greater metastatic potential. Weakly and strongly adherent cells were isolated from an isogenic population using a microfluidic parallel plate flow chamber, where less adherent cells could be detached and collected under low shear stress at low flow rates, and the then increasing the shear stress to wash away moderately adherent cells. By trypsinizing the remaining cells, we were then able to detach and collect the most strongly adherent fraction. These two groups could then be used to investigate migratory propensity in 2D and 3D environments, focal adhesion assembly, contractility, and differential gene expression. We found that increased focal adhesion disassembly and contractility attributed to the lower adhesion strength and increased migration speeds seen in the weakly adherent cells. Furthermore, computational modeling showed that increased contractility in weakly adherent cells allowed them to become adurotactic and migrate against the stiffness gradients seen in primary tumors. This was then validated experimental by inhibiting myosin activity by treating the weakly adherent cells with blebbistatin to restore durotactic behavior, or enhancing contractility with lysophosphatidic acid to make strongly adherent cells adurotactic, suggesting the more contractile, weakly adherent will exhibit higher metastatic potential.

RNA sequencing of weakly and strongly adherent MDA-MB-231 breast cancer cells

showed that they have inherent expression differences genes associated with the cytoskeleton, in particular microtubules and motor proteins involved in vesical transport and contractility. The gene expression profile of triple negative breast cancer patients that was more similar to the weakly adherent cells had a higher recurrence rate or continued progression of their cancer compared to patients with an expression profile similar to the strongly adherent cells. When both fractions were treated with microtubule stabilizing or destabilizing drugs, paclitaxel or nocodazole respectively, the weakly adherent cells become less migratory but no change was observed in the strongly adherent cells. Moreover, the adhesion phenotypes arising from these genetic differences was found to be stable for multiple weeks in culture. Taken together, these studies highlight the potential of using weak cell-ECM adhesion as a prognostic marker for metastatic risk and recurrence of cancer.

5.2 A Label-Free Metric of Metastatic Potential

Compared to other biophysical markers, adhesion strength may serve as a more robust *in vivo* indicator of metastatic disease. In a NOD/SCIDγ mouse model, GFP and Luciferase expressing MDA-MB-231 cells were injected into the inguinal mammary fat pad and allowed to grow for six weeks. Primary tumors and the surrounding stroma were resected and separated, after which the GFP expressing cancer were isolated using FACS and adhesion strength was measured using a spinning disk shear assay. The cells that had invaded the surrounding stroma were found to be less adherent than those that remained within the primary tumor. We then injected mice with presorted weakly or strongly adherent MDA-MB-231 cells, and found that the weakly adherent cells generated significantly more GFP+ lung nodules after 6 weeks. The primary tumors and stroma again were resected, and RNA sequencing of the cancer cells confirmed that gene ontologies associated with migration and invasion were maintained *in vivo*.

We then dissociated the cells collected in these samples to assess their adhesion strength in a divergent channel parallel plate flow chamber. With this device, we were able to deconvolve the adhesion profiles of the cancer and healthy host cells, and quantify the adhesion strength and percentage of metastatic cells in the sample in a label-free manner. Mice that presented with a greater percentage of less adherent cells in the stroma were found to have a higher chance of developing secondary metastases in the lungs, suggesting that these measurements could potentially be used to assess metastatic risk. It is important to note that these murine models may note fully reflect the standard of care received by a patient. Typically, patients will have the primary tumor resected early on in the treatment, followed by treatment with a combination of Adriamycin and Cyclophosphamide, followed by Taxol. Furthermore, the mice used in these studies lacked the presence an immune system, unlike the majority of cancer patients. Together, these differences could potentially lead to changes in the adhesion mechanotype of cells collected from a patient biopsy. While these concerns are important, we believe our results support further *ex vivo* assessment of metastatic risk by measuring the adhesion strength and cancer fraction from patient samples with the divergent parallel plate flow chamber.

5.3 Future Directions

While the results of this dissertation establish the potential of using adhesion strength and percentage of cancer cells as a predictor of metastatic risk in mice, additional studies are necessary to determine if these metrics are as capable for human samples. Repeating these analyses using patient biopsies will be required to validate the clinical relevance of the divergent parallel plate flow chamber. The progression and recurrence of cancer in these patients will be evaluated for at least 5 years to determine the prediction accuracy of the device. However, it remains unclear how or if the tumor microenvironment and its resident cells may affect the

adhesion mechanotype of the metastatic subpopulation. In parallel to these studies, we can characterize the different cell types present in the patient samples, then measure the adhesion profile of immortalized cell lines of the similar type and tissue origin. Then by developing an *in vitro* co-culture model, we can test how the adhesion mechanotype of FACS sorted GFP+ cancer cells changes in response to the presence of these different cell types. This model could also be used to test how the combination of the standard drug treatments affects the overall adhesion profile of the collective population.

Lastly, the ECM proteins found in the tumor microenvironment, as well as its stiffness, may also be of consideration for making improvements to the device's accuracy. To date, we have only measured cell-ECM adhesion strength on fibronectin coated glass slides, and it is unclear if the specific properties of the tumor ECM are required for to make accurate predictions. We can test this by simply repeating the experiments with the cohort of immortalized breast cancer cell lines coating the glass slides with other ECM proteins in place of the fibronectin, and see if cell migration speed and displacement has a better correlation with adhesion strength. Additionally, the glass slide can be coated with a polyacrylamide hydrogel that matches the stiffness of the tumor microenvironment, and coated with the protein of choice, to assess if the substrate stiffness better stratifies metastatic and non-metastatic cell lines.

REFERENCES

1. Taddei, M. L., Giannoni, E., Comito, G. & Chiarugi, P. Microenvironment and tumor cell plasticity: An easy way out. *Cancer Letters* **341**, 80–96 (2013).

2. Brábek, J., Mierke, C. T., Rösel, D., Veselý, P. & Fabry, B. The role of the tissue microenvironment in the regulation of cancer cell motility and invasion. *Cell Communication and Signaling* **8**, 22 (2010).

3. Lauffenburger, D. A. & Horwitz, A. F. Cell Migration: A Physically Integrated Molecular Process. *Cell* **84**, 359–369 (1996).

4. Bear, J. E. & Haugh, J. M. Directed migration of mesenchymal cells: where signaling and the cytoskeleton meet. *Curr Opin Cell Biol* **0**, 74–82 (2014).

5. Charras, G. T., Coughlin, M., Mitchison, T. J. & Mahadevan, L. Life and Times of a Cellular Bleb. *Biophys J* **94**, 1836–1853 (2008).

6. Cox, C. D. *et al.* Removal of the mechanoprotective influence of the cytoskeleton reveals PIEZO1 is gated by bilayer tension. *Nature Communications* **7**, 10366 (2016).

7. Lim, F. Y., Koon, Y. L. & Chiam, K.-H. A computational model of amoeboid cell migration. *Computer Methods in Biomechanics and Biomedical Engineering* **16**, 1085–1095 (2013).

8. Bravo-Cordero, J. J., Hodgson, L. & Condeelis, J. Directed cell invasion and migration during metastasis. *Current Opinion in Cell Biology* **24**, 277–283 (2012).

9. Tyson, R., Zatulovskiy, E., Kay, R. & Bretschneider, T. How blebs and pseudopods cooperate during chemotaxis. *Proceedings of the National Academy of Sciences of the United States of America* **111**, (2014).

10. Bosgraaf, L. & Van Haastert, P. J. M. Navigation of Chemotactic Cells by Parallel Signaling to Pseudopod Persistence and Orientation. *PLoS ONE* **4**, e6842 (2009).

11. Lämmermann, T. *et al.* Rapid leukocyte migration by integrin-independent flowing and squeezing. *Nature* **453**, 51–55 (2008).

12. Petrie, R. J., Koo, H. & Yamada, K. M. Generation of compartmentalized pressure by a nuclear piston governs cell motility in a 3D matrix. *Science* **345**, 1062–1065 (2014).

13. Gkretsi, V. & Stylianopoulos, T. Cell Adhesion and Matrix Stiffness: Coordinating Cancer Cell Invasion and Metastasis. *Front Oncol* **8**, (2018).

14. Ray, A. *et al.* Anisotropic forces from spatially constrained focal adhesions mediate contact guidance directed cell migration. *Nature Communications* **8**, 14923 (2017).

15. Jacquemet, G., Hamidi, H. & Ivaska, J. Filopodia in cell adhesion, 3D migration and cancer cell invasion. *Current Opinion in Cell Biology* **36**, 23–31 (2015).

16. O'Neill, G. M. The coordination between actin filaments and adhesion in mesenchymal migration. *Cell Adhesion & Migration* **3**, 355–357 (2009).

17. Alexandrova, A. Y. *et al.* Comparative Dynamics of Retrograde Actin Flow and Focal Adhesions: Formation of Nascent Adhesions Triggers Transition from Fast to Slow Flow. *PLOS ONE* **3**, e3234 (2008).

18. Cramer, L. P. Molecular mechanism of actin-dependent retrograde flow in lamellipodia of motile cells. *Frontiers in Bioscience-Landmark* **2**, 260–270 (1997).

19. Esmaeili Pourfarhangi, K., Cardenas De La Hoz, E., Cohen, A. R. & Gligorijevic, B. Contact guidance is cell cycle-dependent. *APL Bioeng* **2**, (2018).

20. Chitwood, C. A. *et al.* Breast tumor cell hybrids form spontaneously in vivo and contribute to breast tumor metastases. *APL bioengineering* (2018) doi:10.1063/1.5024744.

21. Krakhmal, N. V., Zavyalova, M. V., Denisov, E. V., Vtorushin, S. V. & Perelmuter, V. M. Cancer Invasion: Patterns and Mechanisms. *Acta Naturae* **7**, 17–28 (2015).

22. van Zijl, F., Krupitza, G. & Mikulits, W. Initial steps of metastasis: Cell invasion and endothelial transmigration. *Mutat Res* **728**, 23–34 (2011).

23. Paňková, K., Rösel, D., Novotný, M. & Brábek, J. The molecular mechanisms of transition between mesenchymal and amoeboid invasiveness in tumor cells. *Cell Mol Life Sci* **67**, 63–71 (2010).

24. Friedl, P. & Wolf, K. Plasticity of cell migration: a multiscale tuning model. *J. Cell Biol.* **188**, 11–19 (2010).

25. Ly, D. & Lumsden, C. 3D amoeboid migration of a eukaryotic cell in a fiber matrix. *Artificial Life and Robotics* **14**, 1–6 (2009).

26. Talkenberger, K., Cavalcanti-Adam, E. A., Voss-Böhme, A. & Deutsch, A. Amoeboid-mesenchymal migration plasticity promotes invasion only in complex heterogeneous microenvironments. *Sci Rep* **7**, (2017).

27. Sakamoto, Y., Prudhomme, S. & Zaman, M. H. Modeling of adhesion, protrusion, and contraction coordination for cell migration simulations. *J Math Biol* **68**, 267–302 (2014).

28. Fraley, S. I. *et al.* A distinctive role for focal adhesion proteins in three-dimensional cell motility. *Nature Cell Biology* **12**, 598–604 (2010).

29. Diz-Muñoz, A. *et al.* Steering cell migration by alternating blebs and actin-rich protrusions. *BMC Biology* **14**, 74 (2016).

30. Paul, R., Heil, P., Spatz, J. P. & Schwarz, U. S. Propagation of Mechanical Stress through the Actin Cytoskeleton toward Focal Adhesions: Model and Experiment. *Biophysical Journal* **94**, 1470–1482 (2008).

31. Yamada, K. M. & Sixt, M. Mechanisms of 3D cell migration. *Nature Reviews Molecular Cell Biology* **20**, 738–752 (2019).

32. Cukierman, E., Pankov, R., Stevens, D. R. & Yamada, K. M. Taking Cell-Matrix Adhesions to the Third Dimension. *Science* **294**, 1708–1712 (2001).

33. Ivetic, A., Hoskins Green, H. L. & Hart, S. J. L-selectin: A Major Regulator of Leukocyte Adhesion, Migration and Signaling. *Front Immunol* **10**, 1068 (2019).

34. Verkhovsky, A. B., Svitkina, T. M. & Borisy, G. G. Self-polarization and directional motility of cytoplasm. *Current Biology* **9**, 11-S1 (1999).

35. Siegel, R. L., Miller, K. D. & Jemal, A. Cancer statistics, 2018. *CA: A Cancer Journal for Clinicians* **68**, 7–30 (2018).

36. Wirtz, D., Konstantopoulos, K. & Searson, P. C. The physics of cancer: the role of physical interactions and mechanical forces in metastasis. *Nat Rev Cancer* **11**, 512–522 (2011).

37. Roussos, E. T., Condeelis, J. S. & Patsialou, A. Chemotaxis in cancer. *Nature Reviews Cancer* **11**, 573–587 (2011).

38. Rubashkin, M. G. *et al.* Force engages vinculin and promotes tumor progression by enhancing PI3K activation of phosphatidylinositol (3,4,5)-triphosphate. *Cancer Res.* **74**, 4597–4611 (2014).

39. Wong, J. Y., Velasco, A., Rajagopalan, P. & Pham, Q. Directed Movement of Vascular Smooth Muscle Cells on Gradient-Compliant Hydrogels. *Langmuir* **19**, 1908–1913 (2003).

40. Pelham, R. J. & Wang, Y. Cell locomotion and focal adhesions are regulated by substrate flexibility. *PNAS* **94**, 13661–13665 (1997).

41. Peyton, S. R. & Putnam, A. J. Extracellular matrix rigidity governs smooth muscle cell motility in a biphasic fashion. *Journal of Cellular Physiology* **204**, 198–209 (2005).

42. McKenzie, A. J. *et al.* The mechanical microenvironment regulates ovarian cancer cell morphology, migration, and spheroid disaggregation. *Scientific Reports* **8**, 1–20 (2018).

43. Fusco, S., Panzetta, V. & Netti, P. A. Mechanosensing of substrate stiffness regulates focal adhesions dynamics in cell. *Meccanica* **52**, 3389–3398 (2017).

44. Zhao, Y. *et al.* Acetylcholinesterase, a key prognostic predictor for hepatocellular carcinoma, suppresses cell growth and induces chemosensitization. *Hepatology* **53**, 493–503 (2011).

45. Wolf, K. *et al.* Physical limits of cell migration: Control by ECM space and nuclear deformation and tuning by proteolysis and traction force. *J Cell Biol* **201**, 1069–1084 (2013).

46. van Helvert, S., Storm, C. & Friedl, P. Mechanoreciprocity in cell migration. *Nature Cell Biology* **20**, 8–20 (2018).

47. Miller, J. P. *et al.* Clinical doses of radiation reduce collagen matrix stiffness. *APL bioengineering* (2018) doi:10.1063/1.5018327.

48. Thrivikraman, G. *et al.* Rapid fabrication of vascularized and innervated cell-laden bone models with biomimetic intrafibrillar collagen mineralization. *Nature Communications* **10**, 3520 (2019).

49. Ramamoorthy, P. *et al.* Metastatic Tumor-in-a-Dish, a Novel Multicellular Organoid to Study Lung Colonization and Predict Therapeutic Response. *Cancer Res.* **79**, 1681–1695 (2019).

50. Danuser, G., Allard, J. & Mogilner, A. Mathematical Modeling of Eukaryotic Cell Migration: Insights Beyond Experiments. *Annu Rev Cell Dev Biol* **29**, 501–528 (2013).

51. Schwarz, U. S., Erdmann, T. & Bischofs, I. B. Focal adhesions as mechanosensors: The two-spring model. *Biosystems* **83**, 225–232 (2006).

52. Moreo, P., García-Aznar, J. M. & Doblaré, M. Modeling mechanosensing and its effect on the migration and proliferation of adherent cells. *Acta Biomater* **4**, 613–621 (2008).

53. Crow, A. *et al.* Contractile Equilibration of Single Cells to Step Changes in Extracellular Stiffness. *Biophys J* **102**, 443–451 (2012).

54. Marcq, P., Yoshinaga, N. & Prost, J. Rigidity Sensing Explained by Active Matter Theory. *Biophys J* **101**, L33–L35 (2011).

55. Chan, C. E. & Odde, D. J. Traction Dynamics of Filopodia on Compliant Substrates. *Science* **322**, 1687–1691 (2008).

56. Zaman, M. H., Kamm, R. D., Matsudaira, P. & Lauffenburger, D. A. Computational Model for Cell Migration in Three-Dimensional Matrices. *Biophys J* **89**, 1389–1397 (2005).

57. Ribeiro, F. O., Gómez-Benito, M. J., Folgado, J., Fernandes, P. R. & García-Aznar, J. M. Computational model of mesenchymal migration in 3D under chemotaxis. *Computer Methods in Biomechanics and Biomedical Engineering* **20**, 59–74 (2017).

58. Schlüter, D. K., Ramis-Conde, I. & Chaplain, M. A. J. Computational Modeling of Single-Cell Migration: The Leading Role of Extracellular Matrix Fibers. *Biophys J* **103**, 1141–1151 (2012).

59. Sun, M. & Zaman, M. H. Modeling, Signaling and Integrated Modeling-experimental Frameworks in Cell Migration. *Wiley Interdiscip Rev Syst Biol Med* **9**, (2017).

60. Rens, E. G. & Edelstein-Keshet, L. From energy to cellular forces in the Cellular Potts Model: An algorithmic approach. *PLOS Computational Biology* **15**, e1007459 (2019).

61. Enderling, H. *et al.* Dependence of Invadopodia Function on Collagen Fiber Spacing and Cross-Linking: Computational Modeling and Experimental Evidence. *Biophys J* **95**, 2203–2218 (2008).

62. Maffei, J. S., Srivastava, J., Fallica, B. & Zaman, M. H. Combinative in vitro studies and computational model to predict 3D cell migration response to drug insult. *Integr Biol (Camb)* **6**, 957–972 (2014).

63. Scianna, M., Preziosi, L. & Wolf, K. A Cellular Potts Model simulating cell migration on and in matrix environments. *Math Biosci Eng* **10**, 235–261 (2013).

64. Shenoy, V. B., Wang, H. & Wang, X. A chemo-mechanical free-energy-based approach to model durotaxis and extracellular stiffness-dependent contraction and polarization of cells. *Interface Focus* **6**, (2016).

65. Ahmadzadeh, H. *et al.* Modeling the two-way feedback between contractility and matrix realignment reveals a nonlinear mode of cancer cell invasion. *Proceedings of the National Academy of Sciences* **114**, E1617–E1626 (2017).

66. Alert, R. & Trepat, X. Physical Models of Collective Cell Migration. *Annual Review of Condensed Matter Physics* **11**, 77–101 (2020).

67. Ziebert, F. & Aranson, I. S. Computational approaches to substrate-based cell motility. *npj Computational Materials* **2**, 1–16 (2016).

68. Palmieri, B., Bresler, Y., Wirtz, D. & Grant, M. Multiple scale model for cell migration in monolayers: Elastic mismatch between cells enhances motility. *Scientific Reports* **5**, 11745 (2015).

69. Kim, M.-C., Whisler, J., Silberberg, Y. R., Kamm, R. D. & Asada, H. H. Cell Invasion Dynamics into a Three Dimensional Extracellular Matrix Fibre Network. *PLoS Comput Biol* **11**, (2015).

70. Chen, J., Weihs, D., Van Dijk, M. & Vermolen, F. J. A phenomenological model for cell and nucleus deformation during cancer metastasis. *Biomech Model Mechanobiol* **17**, 1429–1450 (2018).

71. Niculescu, I., Textor, J. & de Boer, R. J. Crawling and Gliding: A Computational Model for Shape-Driven Cell Migration. *PLoS Comput Biol* **11**, (2015).

72. Bangasser, B. L. & Odde, D. J. Master equation-based analysis of a motor-clutch model for cell traction force. *Cell Mol Bioeng* **6**, 449–459 (2013).

73. Partridge, M. A. & Marcantonio, E. E. Initiation of attachment and generation of mature focal adhesions by integrin-containing filopodia in cell spreading. *Mol. Biol. Cell* **17**, 4237–4248 (2006).

74. Kim, M.-C., Neal, D. M., Kamm, R. D. & Asada, H. H. Dynamic Modeling of Cell Migration and Spreading Behaviors on Fibronectin Coated Planar Substrates and Micropatterned Geometries. *PLoS Comput Biol* **9**, (2013).

75. Cuvelier, D. *et al.* The universal dynamics of cell spreading. *Curr. Biol.* **17**, 694–699 (2007).

76. Yeoman, B. M. & Katira, P. A stochastic algorithm for accurately predicting path persistence of cells migrating in 3D matrix environments. *PLOS ONE* **13**, e0207216 (2018).

77. Collins, T. A., Yeoman, B. M. & Katira, P. To lead or to herd: optimal strategies for 3D collective migration of cell clusters. *Biomech Model Mechanobiol* (2020) doi:10.1007/s10237-020-01290-y.

78. Stokes, C. L. & Lauffenburger, D. A. Analysis of the roles of microvessel endothelial cell random motility and chemotaxis in angiogenesis. *J. Theor. Biol.* **152**, 377–403 (1991).

79. Tranquillo, R. T. & Lauffenburger, D. A. Stochastic model of leukocyte chemosensory movement. *J Math Biol* **25**, 229–262 (1987).

80. Dickinson, R. B. & Tranquillo, R. T. A stochastic model for adhesion-mediated cell random motility and haptotaxis. *J. Math. Biol.* **31**, 563–600.

81. Kim, M.-C., Silberberg, Y. R., Abeyaratne, R., Kamm, R. D. & Asada, H. H. Computational modeling of three-dimensional ECM-rigidity sensing to guide directed cell migration. *PNAS* 201717230 (2018) doi:10.1073/pnas.1717230115.

82. Zaman, M. H., Matsudaira, P. & Lauffenburger, D. A. Understanding Effects of Matrix Protease and Matrix Organization on Directional Persistence and Translational Speed in Three-Dimensional Cell Migration. *Ann Biomed Eng* **35**, 91–100 (2007).

83. Lo, C. M., Wang, H. B., Dembo, M. & Wang, Y. L. Cell movement is guided by the rigidity of the substrate. *Biophys J* **79**, 144–152 (2000).

84. Leventhal, K. R. *et al.* Matrix Crosslinking Forces Tumor Progression by Enhancing Integrin Signaling. *Cell* **139**, 891–906 (2009).

85. Paszek, M. J. *et al.* Tensional homeostasis and the malignant phenotype. *Cancer Cell* **8**, 241–254 (2005).

86. Malik, A. A., Wennberg, B. & Gerlee, P. The Impact of Elastic Deformations of the Extracellular Matrix on Cell Migration. *Bull. Math. Biol.* **82**, 49 (2020).

87. Kwon, T., Kwon, O., Cha, H.-J. & Sung, B. Stochastic and Heterogeneous Cancer Cell Migration: Experiment and Theory. *Scientific Reports* **9**, 16297 (2019).

88. Heck, T. *et al.* The role of actin protrusion dynamics in cell migration through a degradable viscoelastic extracellular matrix: Insights from a computational model. *PLoS Comput Biol* **16**, (2020).

89. Wisdom, K. M. *et al.* Matrix mechanical plasticity regulates cancer cell migration through confining microenvironments. *Nature Communications* **9**, 4144 (2018).

90. Ahmmed, S. M. *et al.* Multi-sample deformability cytometry of cancer cells. *APL Bioengineering* **2**, 032002 (2018).

91. Ehrbar, M. *et al.* Elucidating the Role of Matrix Stiffness in 3D Cell Migration and Remodeling. *Biophys J* **100**, 284–293 (2011).

92. Beri, P. *et al.* Cell adhesiveness serves as a biophysical marker for metastatic potential | Cancer Research. *Cancer Research* **80**, 901–911 (2020).

93. Bangasser, B. L. *et al.* Shifting the optimal stiffness for cell migration. *Nature Communications* **8**, 15313 (2017).

94. Bell, G. I. Models for the specific adhesion of cells to cells. *Science* **200**, 618–627 (1978).

95. Elosegui-Artola, A. *et al.* Mechanical regulation of a molecular clutch defines force transmission and transduction in response to matrix rigidity. *Nature Cell Biology* **18**, 540–548 (2016).

96. Plotnikov, S. V., Pasapera, A. M., Sabass, B. & Waterman, C. M. Force fluctuations within focal adhesions mediate ECM-rigidity sensing to guide directed cell migration. *Cell* **151**, 1513–1527 (2012).

97. Hecht, I. *et al.* Tumor invasion optimization by mesenchymal-amoeboid heterogeneity. *Sci Rep* **5**, 10622 (2015).

98. Doyle, A. D., Wang, F. W., Matsumoto, K. & Yamada, K. M. One-dimensional topography underlies three-dimensional fibrillar cell migration. *J. Cell Biol.* **184**, 481–490 (2009).

99. Holle, A. W. *et al.* Cancer Cells Invade Confined Microchannels via a Self-Directed Mesenchymal-to-Amoeboid Transition. *Nano Lett* **19**, 2280–2290 (2019).

100. Wang, M. *et al.* Microchannel Stiffness and Confinement Jointly Induce the Mesenchymal-Amoeboid Transition of Cancer Cell Migration. *Nano Letters* **19**, (2019).

101. Katt, M. E., Placone, A. L., Wong, A. D., Xu, Z. S. & Searson, P. C. In Vitro Tumor Models: Advantages, Disadvantages, Variables, and Selecting the Right Platform. *Frontiers in Bioengineering and Biotechnology* **4**, (2016).

102. Beri, P. *et al.* Biomaterials to model and measure epithelial cancers. *Nature Reviews Materials* **3**, 418–430 (2018).

103. Lee, J. Y. & Chaudhuri, O. Modeling the tumor immune microenvironment for drug discovery using 3D culture. *APL Bioengineering* **5**, 010903 (2021).

104. Acerbi, I. *et al.* Human breast cancer invasion and aggression correlates with ECM stiffening and immune cell infiltration. *Integrative Biology* **7**, 1120–1134 (2015).

105. Happe, C. L., Tenerelli, K. P., Gromova, A. K., Kolb, F. & Engler, A. J. Mechanically patterned neuromuscular junctions-in-a-dish have improved functional maturation. *MBoC* **28**, 1950–1958 (2017).

106. Palecek, S. P., Loftus, J. C., Ginsberg, M. H., Lauffenburger, D. A. & Horwitz, A. F. Integrin-ligand binding properties govern cell migration speed through cell-substratum adhesiveness. *Nature* **385**, 537–540 (1997).

107. McElwain, D. L. S. & Pettet, G. J. Cell migration in multicell spheroids: Swimming against the tide. *Bulletin of Mathematical Biology* **55**, 655–674 (1993).

108. Zanoni, M. *et al.* 3D tumor spheroid models for in vitro therapeutic screening: a systematic approach to enhance the biological relevance of data obtained. *Scientific Reports* **6**, 19103 (2016).

109. Mueller-Klieser, W. Multicellular spheroids. *J Cancer Res Clin Oncol* **113**, 101–122 (1987).

110. Gottfried, E., Kunz-Schughart, L. A., Andreesen, R. & Kreutz, M. Brave Little World: Spheroids as an in vitro Model to Study Tumor-Immune-Cell Interactions. *Cell Cycle* **5**, 691–695 (2006).

111. Friedrich, J., Seidel, C., Ebner, R. & Kunz-Schughart, L. A. Spheroid-based drug screen: considerations and practical approach. *Nat Protoc* **4**, 309–324 (2009).

112. Do, A.-V., Khorsand, B., Geary, S. M. & Salem, A. K. 3D Printing of Scaffolds for Tissue Regeneration Applications. *ResearchGate* **4**, (2015).

113. Mandrycky, C., Wang, Z., Kim, K. & Kim, D.-H. 3D bioprinting for engineering complex tissues. *Biotechnology Advances* **34**, 422–434 (2016).

114. Xiang, Y. *et al.* 3D bioprinting of complex tissues in vitro: state-of-the-art and future perspectives. *Arch Toxicol* **96**, 691–710 (2022).

115. Hong, M., Clubb, J. D. & Chen, Y. Y. Engineering CAR-T Cells for Next-Generation Cancer Therapy. *Cancer Cell* **38**, 473–488 (2020).

116. Boussommier-Calleja, A., Li, R., Chen, M. B., Wong, S. C. & Kamm, R. D. Microfluidics: A New Tool for Modeling Cancer–Immune Interactions. *Trends in Cancer* **2**, 6–19 (2016).

117. Lee, S. W. L. *et al.* Characterizing the Role of Monocytes in T Cell Cancer Immunotherapy Using a 3D Microfluidic Model. *Frontiers in Immunology* **9**, (2018).

118. Alibert, C., Goud, B. & Manneville, J.-B. Are cancer cells really softer than normal cells? *Biol Cell* **109**, 167–189 (2017).

119. Guo, Q., Park, S. & Ma, H. Microfluidic micropipette aspiration for measuring the deformability of single cells. *Lab on a chip* **12**, 2687–95 (2012).

120. Mak, M. & Erickson, D. A serial micropipette microfluidic device with applications to cancer cell repeated deformation studies. *Integr Biol (Camb)* **5**, 1374–1384 (2013).

121. Kraning-Rush, C. M., Califano, J. P. & Reinhart-King, C. A. Cellular traction stresses increase with increasing metastatic potential. *PLoS ONE* **7**, e32572 (2012).

122. Lo Sardo, V. *et al.* Unveiling the Role of the Most Impactful Cardiovascular Risk Locus through Haplotype Editing. *Cell* **175**, 1796-1810.e20 (2018).

123. Fuhrmann, A., Banisadr, A., Beri, P., Tlsty, T. D. & Engler, A. J. Metastatic State of Cancer Cells May Be Indicated by Adhesion Strength. *Biophys J* **112**, 736–745 (2017).

124. Banisadr, A. *et al.* EGFRvIII uses intrinsic and extrinsic mechanisms to reduce glioma adhesion and increase migration. *J Cell Sci* **133**, jcs247189 (2020).

125. Usami, S., Chen, H. H., Zhao, Y., Chien, S. & Skalak, R. Design and construction of a linear shear stress flow chamber. *Ann Biomed Eng* **21**, 77–83 (1993).

126. Qian, W., Zhang, Y. & Chen, W. Capturing Cancer: Emerging Microfluidic Technologies for the Capture and Characterization of Circulating Tumor Cells. *Small* **11**, 3850–3872 (2015).

127. So, W. Y. & Tanner, K. Emerging principles of cancer biophysics. *Fac Rev* **10**, 61 (2021).

128. Yankaskas, C. L. *et al.* A microfluidic assay for the quantification of the metastatic propensity of breast cancer specimens. *Nat Biomed Eng* **3**, 452–465 (2019).

129. Manak, M. S. *et al.* Live-cell phenotypic-biomarker microfluidic assay for the risk stratification of cancer patients via machine learning. *Nat Biomed Eng* **2**, 761–772 (2018).

130. Kong, F., García, A. J., Mould, A. P., Humphries, M. J. & Zhu, C. Demonstration of catch bonds between an integrin and its ligand. *J Cell Biol* **185**, 1275–1284 (2009).

131. Sunyer, R. *et al.* Collective cell durotaxis emerges from long-range intercellular force transmission. *Science* **353**, 1157–1161 (2016).

132. Escribano, J. *et al.* A hybrid computational model for collective cell durotaxis. *Biomech Model Mechanobiol* **17**, 1037–1052 (2018).

133. Ladoux, B. & Mège, R.-M. Mechanobiology of collective cell behaviours. *Nat Rev Mol Cell Biol* **18**, 743–757 (2017).

134. Boocock, D., Hino, N., Ruzickova, N., Hirashima, T. & Hannezo, E. Theory of mechanochemical patterning and optimal migration in cell monolayers. *Nature Physics* **17**, 1–8 (2021).

135. Steeg, P. S. Targeting metastasis. *Nat Rev Cancer* **16**, 201–218 (2016).

136. Quintana, E. *et al.* Efficient tumour formation by single human melanoma cells. *Nature* **456**, 593–598 (2008).

137. Polyak, K. Heterogeneity in breast cancer. *J Clin Invest* **121**, 3786–3788 (2011).

138. Sun, X. & Yu, Q. Intra-tumor heterogeneity of cancer cells and its implications for cancer treatment. *Acta Pharmacol Sin* **36**, 1219–1227 (2015).

139. Liu, Y. *et al.* Lack of correlation of stem cell markers in breast cancer stem cells. *British Journal of Cancer* **110**, 2063–2071 (2014).

140. Dudani, J. S., Gossett, D. R., Tse, H. T. K. & Carlo, D. D. Pinched-flow hydrodynamic stretching of single-cells. *Lab Chip* **13**, 3728–3734 (2013).

141. Gossett, D. R. *et al.* Hydrodynamic stretching of single cells for large population mechanical phenotyping. *PNAS* **109**, 7630–7635 (2012).

142. Qi, D. *et al.* Screening cell mechanotype by parallel microfiltration. *Scientific Reports* **5**, 17595 (2015).

143. Nyberg, K. D. *et al.* The physical origins of transit time measurements for rapid, single cell mechanotyping. *Lab Chip* **16**, 3330–3339 (2016).

144. Ridley, A. J. *et al.* Cell Migration: Integrating Signals from Front to Back. *Science* **302**, 1704–1709 (2003).

145. DiMilla, P. A., Stone, J. A., Quinn, J. A., Albelda, S. M. & Lauffenburger, D. A. Maximal migration of human smooth muscle cells on fibronectin and type IV collagen occurs at an intermediate attachment strength. *J Cell Biol* **122**, 729–737 (1993).

146. Bijian, K. *et al.* Targeting focal adhesion turnover in invasive breast cancer cells by the purine derivative reversine. *British Journal of Cancer* **109**, 2810–2818 (2013).

147. Indra, I. *et al.* An in vitro correlation of mechanical forces and metastatic capacity. *Phys Biol* **8**, 015015 (2011).

148. Reticker-Flynn, N. E. *et al.* A combinatorial extracellular matrix platform identifies cell-extracellular matrix interactions that correlate with metastasis. *Nat Commun* **3**, 1122 (2012).

149. *Metastasis Research Protocols*. vol. 1070 (Springer New York, 2014).

150. Palmer, C. P. *et al.* Single cell adhesion measuring apparatus (SCAMA): application to cancer cell lines of different metastatic potential and voltage-gated Na+ channel expression. *Eur Biophys J* **37**, 359–368 (2008).

151. Garcia, A. J. & Gallant, N. D. Stick and grip. *Cell Biochem Biophys* **39**, 61–73 (2003).

152. Veiseh, M. *et al.* Cellular heterogeneity profiling by hyaluronan probes reveals an invasive but slow-growing breast tumor subset. *Proceedings of the National Academy of Sciences* **111**, E1731–E1739 (2014).

153. Gupta, P. B. *et al.* Stochastic state transitions give rise to phenotypic equilibrium in populations of cancer cells. *Cell* **146**, 633–644 (2011).

154. Fuhrmann, A., Li, J., Chien, S. & Engler, A. J. Cation Type Specific Cell Remodeling Regulates Attachment Strength. *PLOS ONE* **9**, e102424 (2014).

155. Seltzer, M. H., Rosato, F. E. & Fletcher, M. J. Serum and tissue magnesium levels in human breast carcinoma. *Journal of Surgical Research* **10**, 159–162 (1970).

156. Seltzer, M. H., Rosato, F. E. & Fletcher, M. J. Serum and Tissue Calcium in Human Breast Carcinoma. *Cancer Research* **30**, 615–616 (1970).

157. Heppner, G. H. & Wolman, S. R. MCF-10AT: A Model for Human Breast Cancer Development. *The Breast Journal* **5**, 122–129 (1999).

158. Mierke, C. T. *et al.* Vinculin Facilitates Cell Invasion into Three-dimensional Collagen Matrices. *J Biol Chem* **285**, 13121–13130 (2010).

159. Stroud, M. J., Kammerer, R. A. & Ballestrem, C. Characterization of G2L3 (GAS2-like 3), a New Microtubule- and Actin-binding Protein Related to Spectraplakins. *J Biol Chem* **286**, 24987–24995 (2011).

160. Friedl, P., Wolf, K. & Lammerding, J. Nuclear mechanics during cell migration. *Current Opinion in Cell Biology* **23**, 55–64 (2011).

161. Jayo, A. *et al.* Fascin Regulates Nuclear Movement and Deformation in Migrating Cells. *Dev Cell* **38**, 371–383 (2016).

162. Kumar, N., Gupta, S., Dabral, S., Singh, S. & Sehrawat, S. Role of exchange protein directly activated by cAMP (EPAC1) in breast cancer cell migration and apoptosis. *Mol. Cell. Biochem.* **430**, 115–125 (2017).

163. Yang, M.-H. *et al.* MALAT1 promotes colorectal cancer cell proliferation/migration/invasion via PRKA kinase anchor protein 9. *Biochim. Biophys. Acta* **1852**, 166–174 (2015).

164. Ahmed, S. M. *et al.* KIF14 negatively regulates Rap1a-Radil signaling during breast cancer progression. *J. Cell Biol.* **199**, 951–967 (2012).

165.   Thériault, B. L. *et al.* Transcriptional and epigenetic regulation of KIF14 overexpression in ovarian cancer. *PLoS ONE* **9**, e91540 (2014).

166.   Mi, L. *et al.* The metastatic suppressor NDRG1 inhibits EMT, migration and invasion through interaction and promotion of caveolin-1 ubiquitylation in human colorectal cancer cells. *Oncogene* **36**, 4323–4335 (2017).

167.   Hu, J. & Verkman, A. S. Increased migration and metastatic potential of tumor cells expressing aquaporin water channels. *FASEB J* **20**, 1892–1894 (2006).

168.   Slack, J. K. *et al.* Alterations in the focal adhesion kinase/Src signal transduction pathway correlate with increased migratory capacity of prostate carcinoma cells. *Oncogene* **20**, 1152–1163 (2001).

169.   Frame, M. C., Fincham, V. J., Carragher, N. O. & Wyke, J. A. v-Src's hold over actin and cell adhesions. *Nat Rev Mol Cell Biol* **3**, 233–245 (2002).

170.   McLean, G. W. *et al.* The role of focal-adhesion kinase in cancer — a new therapeutic opportunity. *Nat Rev Cancer* **5**, 505–515 (2005).

171.   Feng, R. *et al.* Targeting the Microtubular Network as a New Antimyeloma Strategy. *Molecular Cancer Therapeutics* **10**, 1886–1896 (2011).

172.   Kumar, A. *et al.* Mechanical activation of noncoding-RNA-mediated regulation of disease-associated phenotypes in human cardiomyocytes. *Nat Biomed Eng* **3**, 137–146 (2019).

173.   Martin, M. Cutadapt removes adapter sequences from high-throughput sequencing reads. *EMBnet.journal* **17**, 10–12 (2011).

174.   Andrews, S. FAST QC: A quality control tool for high throughput sequence data. https://www.bioinformatics.babraham.ac.uk/projects/fastqc/.

175.   Dobin, A. *et al.* STAR: ultrafast universal RNA-seq aligner. *Bioinformatics* **29**, 15–21 (2013).

176.   Anders, S., Pyl, P. T. & Huber, W. HTSeq--a Python framework to work with high-throughput sequencing data. *Bioinformatics* **31**, 166–169 (2015).

177.   Love, M. I., Huber, W. & Anders, S. Moderated estimation of fold change and dispersion for RNA-seq data with DESeq2. *Genome Biology* **15**, 550 (2014).

178.   Wang, L., Wang, S. & Li, W. RSeQC: quality control of RNA-seq experiments. *Bioinformatics* **28**, 2184–2185 (2012).

179.   Hennig, C. *fpc: Flexible Procedures for Clustering*. (2020).

180. Heinz, S. *et al.* Simple combinations of lineage-determining transcription factors prime cis-regulatory elements required for macrophage and B cell identities. *Mol Cell* **38**, 576–589 (2010).

181. Liu, J. *et al.* An Integrated TCGA Pan-Cancer Clinical Data Resource to Drive High-Quality Survival Outcome Analytics. *Cell* **173**, 400-416.e11 (2018).

182. DuChez, B. J., Doyle, A. D., Dimitriadis, E. K. & Yamada, K. M. Durotaxis by Human Cancer Cells. *Biophysical Journal* **116**, 670–683 (2019).

183. Joaquin, D. *et al.* Cell migration and organization in three-dimensional in vitro culture driven by stiffness gradient. *Biotechnology and Bioengineering* **113**, 2496–2506 (2016).

184. Novikova, E. A., Raab, M., Discher, D. E. & Storm, C. Persistence-driven durotaxis: Generic, directed motility in rigidity gradients. *Phys Rev Lett* **118**, 078103 (2017).

185. Isomursu, A. *et al.* Negative durotaxis: cell movement toward softer environments. *bioRxiv* 2020.10.27.357178 (2020) doi:10.1101/2020.10.27.357178.

186. Singh, S. P., Schwartz, M. P., Lee, J. Y., Fairbanks, B. D. & Anseth, K. S. A peptide functionalized poly(ethylene glycol) (PEG) hydrogel for investigating the influence of biochemical and biophysical matrix properties on tumor cell migration. *Biomater Sci* **2**, 1024–1034 (2014).

187. Lara Rodriguez, L. & Schneider, I. C. Directed cell migration in multi-cue environments. *Integr Biol (Camb)* **5**, 1306–1323 (2013).

188. Lachowski, D. *et al.* Substrate Rigidity Controls Activation and Durotaxis in Pancreatic Stellate Cells. *Scientific Reports* **7**, 1–12 (2017).

189. Sawada, Y. *et al.* Force Sensing by Extension of the Src Family Kinase Substrate, p130Cas. *Cell* **127**, 1015–1026 (2006).

190. Holmes, W. R. & Edelstein-Keshet, L. A Comparison of Computational Models for Eukaryotic Cell Shape and Motility. *PLoS Comput Biol* **8**, (2012).

191. Mak, M. *et al.* Integrated Analysis of Intracellular Dynamics of MenaINV Cancer Cells in a 3D Matrix. *Biophysical Journal* **112**, 1874–1884 (2017).

192. Feng, J., Levine, H., Mao, X. & Sander, L. M. Cell motility, contact guidance, and durotaxis. *Soft Matter* **15**, 4856–4864 (2019).

193. Mak, M., Kim, T., Zaman, M. H. & Kamm, R. D. Multiscale mechanobiology: computational models for integrating molecules to multicellular systems. *Integr Biol (Camb)* **7**, 1093–1108 (2015).

194. Stefanoni, F., Ventre, M., Mollica, F. & Netti, P. A. A numerical model for durotaxis. *Journal of Theoretical Biology* **280**, 150–158 (2011).

195.   Shatkin, G., Yeoman, B., Birmingham, K., Katira, P. & Engler, A. J. Computational models of migration modes improve our understanding of metastasis. *APL Bioengineering* **4**, 041505 (2020).

196.   Cox, T. R. & Erler, J. T. Remodeling and homeostasis of the extracellular matrix: implications for fibrotic diseases and cancer. *Disease Models & Mechanisms* **4**, 165–178 (2011).

197.   Burgstaller, G. *et al.* The instructive extracellular matrix of the lung: basic composition and alterations in chronic lung disease. *European Respiratory Journal* **50**, (2017).

198.   Pankova, D. *et al.* RASSF1A controls tissue stiffness and cancer stem-like cells in lung adenocarcinoma. *EMBO J* **38**, (2019).

199.   White, E. S. Lung Extracellular Matrix and Fibroblast Function. *Ann Am Thorac Soc* **12**, S30–S33 (2015).

200.   Ahn, B.-M., Kim, J., Ian, L., Rha, K.-H. & Kim, H.-J. Mechanical property characterization of prostate cancer using a minimally motorized indenter in an ex vivo indentation experiment. *Urology* **76**, 1007–1011 (2010).

201.   L. Krupski, T. *et al.* Assessing mechanical properties of benign and malignant prostate tissue. *JCO* **28**, e15109–e15109 (2010).

202.   Zhai, L. *et al.* Characterizing the stiffness of Human Prostates using Acoustic Radiation Force. *Ultrason Imaging* **32**, 201–213 (2010).

203.   Boettiger, D. Quantitative Measurements of Integrin-Mediated Adhesion to Extracellular Matrix. in *Methods in Enzymology* vol. 426 1–25 (Academic Press, 2007).

204.   Morikis, V. A. *et al.* Selectin catch-bonds mechanotransduce integrin activation and neutrophil arrest on inflamed endothelium under shear flow. *Blood* **130**, 2101–2110 (2017).

205.   Zhu, C. & Chen, W. Catch Bonds of Integrin/Ligand Interactions. in *Single-molecule Studies of Proteins* (ed. Oberhauser, A. F.) 77–96 (Springer, 2013). doi:10.1007/978-1-4614-4921-8_3.

206.   Koenderink, G. H. *et al.* An active biopolymer network controlled by molecular motors. *Proc. Natl. Acad. Sci. U.S.A.* **106**, 15192–15197 (2009).

207.   Tan, S. J. *et al.* Regulation and dynamics of force transmission at individual cell-matrix adhesion bonds. *Science Advances* **6**, eaax0317 (2020).

208.   Chaudhuri, O., Cooper-White, J., Janmey, P. A., Mooney, D. J. & Shenoy, V. B. Effects of extracellular matrix viscoelasticity on cellular behaviour. *Nature* **584**, 535–546 (2020).

209.   Malandrino, A., Trepat, X., Kamm, R. D. & Mak, M. Dynamic filopodial forces induce accumulation, damage, and plastic remodeling of 3D extracellular matrices. *PLOS Computational Biology* **15**, e1006684 (2019).

210.   Münster, S. *et al.* Strain history dependence of the nonlinear stress response of fibrin and collagen networks. *Proc Natl Acad Sci U S A* **110**, 12197–12202 (2013).

211.   Heyes, D. M. Translational and rotational diffusion of rod shaped molecules by molecular dynamics simulations. *J. Chem. Phys.* **150**, 184503 (2019).

212.   Schaller, M. D. Paxillin: a focal adhesion-associated adaptor protein. *Oncogene* **20**, 6459–6472 (2001).

213.   Hansen, M. D. H. & Kwiatkowski, A. V. Chapter One - Control of Actin Dynamics by Allosteric Regulation of Actin Binding Proteins. in *International Review of Cell and Molecular Biology* (ed. Jeon, K. W.) vol. 303 1–25 (Academic Press, 2013).

214.   Legate, K. R., Montañez, E., Kudlacek, O. & Fässler, R. ILK, PINCH and parvin: the tIPP of integrin signalling. *Nat. Rev. Mol. Cell Biol.* **7**, 20–31 (2006).

215.   Wu, C. PINCH, N(i)ck and the ILK: network wiring at cell-matrix adhesions. *Trends Cell Biol.* **15**, 460–466 (2005).

216.   Wu, C. & Dedhar, S. Integrin-linked kinase (ILK) and its interactors. *J Cell Biol* **155**, 505–510 (2001).

217.   Grashoff, C. *et al.* Measuring mechanical tension across vinculin reveals regulation of focal adhesion dynamics. *Nature* **466**, 263–266 (2010).

218.   Rio, A. del *et al.* Stretching Single Talin Rod Molecules Activates Vinculin Binding. *Science* **323**, 638–641 (2009).

219.   Burridge, K. & Guilluy, C. Focal adhesions, stress fibers and mechanical tension. *Exp Cell Res* **343**, 14–20 (2016).

220.   Goley, E. D. & Welch, M. D. The ARP2/3 complex: an actin nucleator comes of age. *Nature Reviews Molecular Cell Biology* **7**, 713–726 (2006).

221.   Howard, J. *Mechanics of Motor Proteins and the Cytoskeleton*. vol. 55 (Sinauer Associates, Publishers, 2001).

222.   Molloy, J. E., Burns, J. E., Kendrick-Jones, J., Tregear, R. T. & White, D. C. S. Movement and force produced by a single myosin head. *Nature* **378**, 209–212 (1995).

223.   Cooper, G. M. & Hausman, R. E. *The Cell: A Molecular Approach*. (ASM Press, 2007).

224.   Pompe, T. *et al.* Friction-Controlled Traction Force in Cell Adhesion. *Biophys J* **101**, 1863–1870 (2011).

225.   Bosgraaf, L. & Van Haastert, P. J. M. The Ordered Extension of Pseudopodia by Amoeboid Cells in the Absence of External Cues. *PLoS ONE* **4**, (2009).

226.   Bidone, T. C., Skeeters, A. V., Oakes, P. W. & Voth, G. A. Multiscale model of integrin adhesion assembly. *PLOS Computational Biology* **15**, e1007077 (2019).

227.   Vicente-Manzanares, M., Choi, C. K. & Horwitz, A. R. Integrins in cell migration – the actin connection. *J Cell Sci* **122**, 199–206 (2009).

228.   Tapia-Rojo, R., Alonso-Caballero, A. & Fernandez, J. M. Direct observation of a coil-to-helix contraction triggered by vinculin binding to talin. *Science Advances* **6**, eaaz4707 (2020).

229.   Blystone, S. D. Integrating an integrin: a direct route to actin. *Biochimica et Biophysica Acta (BBA) - Molecular Cell Research* **1692**, 47–54 (2004).

230.   Himmel, M. *et al.* Control of High Affinity Interactions in the Talin C Terminus. *J Biol Chem* **284**, 13832–13842 (2009).

231.   Vavylonis, D., Yang, Q. & O'Shaughnessy, B. Actin polymerization kinetics, cap structure, and fluctuations. *PNAS* **102**, 8543–8548 (2005).

232.   Pollard, T. D. Rate constants for the reactions of ATP- and ADP-actin with the ends of actin filaments. *J Cell Biol* **103**, 2747–2754 (1986).

233.   Prahl, L. S., Stanslaski, M. R., Vargas, P., Piel, M. & Odde, D. J. Predicting Confined 1D Cell Migration from Parameters Calibrated to a 2D Motor-Clutch Model. *Biophysical Journal* **118**, 1709–1720 (2020).

234.   Elosegui-Artola, A. *et al.* Image Analysis for the Quantitative Comparison of Stress Fibers and Focal Adhesions. *PLOS ONE* **9**, e107393 (2014).

235.   Brizendine, R. K. *et al.* Velocities of unloaded muscle filaments are not limited by drag forces imposed by myosin cross-bridges. *PNAS* **112**, 11235–11240 (2015).

236.   Cooper, G. M. Structure and Organization of Actin Filaments. *The Cell: A Molecular Approach. 2nd edition* (2000).

237.   Siegel, R. L., Miller, K. D., Fuchs, H. E. & Jemal, A. Cancer Statistics, 2021. *CA: A Cancer Journal for Clinicians* **71**, 7–33 (2021).

238.   Visser, L. L. *et al.* Predictors of an Invasive Breast Cancer Recurrence after DCIS: A Systematic Review and Meta-analyses. *Cancer Epidemiol Biomarkers Prev* **28**, 835–845 (2019).

239.   Taneja, P. *et al.* Classical and Novel Prognostic Markers for Breast Cancer and their Clinical Significance. *Clin Med Insights Oncol* **4**, 15–34 (2010).

240. Weigelt, B., Peterse, J. L. & van 't Veer, L. J. Breast cancer metastasis: markers and models. *Nat Rev Cancer* **5**, 591–602 (2005).

241. Medema, J. P. Cancer stem cells: the challenges ahead. *Nat Cell Biol* **15**, 338–344 (2013).

242. Niravath, P. O. Evaluation of Patients for Metastasis Prior to Primary Therapy. in *Disease of the Breast* (eds. Lippman, M. E., Harris, J. R., Morrow, M. & Osborne, C.K.) 488–494 (Wolters Kluwer, 2014).

243. Wong, B. S. *et al.* A microfluidic cell-migration assay for the prediction of progression-free survival and recurrence time of patients with glioblastoma. *Nat Biomed Eng* **5**, 26–40 (2021).

244. Gensbittel, V. *et al.* Mechanical Adaptability of Tumor Cells in Metastasis. *Dev Cell* **56**, 164–179 (2021).

245. Wirtz, D., Konstantopoulos, K. & Searson, P. C. The physics of cancer: the role of physical interactions and mechanical forces in metastasis. *Nature Reviews Cancer* **11**, 512–522 (2011).

246. Beri, P. *et al.* Cell Adhesiveness Serves as a Biophysical Marker for Metastatic Potential. *Cancer Res* **80**, 901–911 (2020).

247. Yeoman, B. *et al.* Adhesion strength and contractility enable metastatic cells to become adurotactic. *Cell Reports* **34**, 108816 (2021).

248. Paszek, M. J. *et al.* Tensional homeostasis and the malignant phenotype. *Cancer Cell* **8**, 241–254 (2005).

249. Kuperwasser, C. *et al.* A mouse model of human breast cancer metastasis to human bone. *Cancer Res* **65**, 6130–6138 (2005).

250. Jin, X. *et al.* A metastasis map of human cancer cell lines. *Nature* **588**, 331–336 (2020).

251. Suvà, M. L. & Tirosh, I. Single-Cell RNA Sequencing in Cancer: Lessons Learned and Emerging Challenges. *Molecular Cell* **75**, 7–12 (2019).

252. Zhu, S., Qing, T., Zheng, Y., Jin, L. & Shi, L. Advances in single-cell RNA sequencing and its applications in cancer research. *Oncotarget* **8**, 53763–53779 (2017).

253. Bartoschek, M. *et al.* Spatially and functionally distinct subclasses of breast cancer-associated fibroblasts revealed by single cell RNA sequencing. *Nature Communications* **9**, 5150 (2018).

254. Wang, L. *et al.* Promise and limits of the CellSearch platform for evaluating pharmacodynamics in circulating tumor cells. *Seminars in Oncology* **43**, 464–475 (2016).

255.   Sheng, Y. *et al.* Comparison of analytic performances of Cellsearch and iFISH approach in detecting circulating tumor cells. *Oncotarget* **8**, 8801–8806 (2017).

256.   de Wit, S. *et al.* The detection of EpCAM(+) and EpCAM(-) circulating tumor cells. *Sci Rep* **5**, 12270 (2015).

257.   Gorges, T. M. *et al.* Improved Detection of Circulating Tumor Cells in Metastatic Colorectal Cancer by the Combination of the CellSearch® System and the AdnaTest®. *PLoS One* **11**, e0155126 (2016).

258.   Smerage, J. B. *et al.* Circulating tumor cells and response to chemotherapy in metastatic breast cancer: SWOG S0500. *J Clin Oncol* **32**, 3483–3489 (2014).

259.   Dagogo-Jack, I. & Shaw, A. T. Tumour heterogeneity and resistance to cancer therapies. *Nat Rev Clin Oncol* **15**, 81–94 (2018).

260.   Goel, S. *et al.* Normalization of the vasculature for treatment of cancer and other diseases. *Physiol Rev* **91**, 1071–1121 (2011).

261.   Martin, J. D., Fukumura, D., Duda, D. G., Boucher, Y. & Jain, R. K. Reengineering the Tumor Microenvironment to Alleviate Hypoxia and Overcome Cancer Heterogeneity. *Cold Spring Harb Perspect Med* **6**, (2016).

262.   Alix-Panabières, C. *et al.* Detection and characterization of putative metastatic precursor cells in cancer patients. *Clin Chem* **53**, 537–539 (2007).

263.   Satelli, A., Brownlee, Z., Mitra, A., Meng, Q. H. & Li, S. Circulating tumor cell enumeration using a combination of EpCAM and Cell-surface vimentin based methods for monitoring breast cancer therapeutic response. *Clin Chem* **61**, 259–266 (2015).

264.   Byun, S. *et al.* Characterizing deformability and surface friction of cancer cells. *Proc Natl Acad Sci U S A* **110**, 7580–7585 (2013).

265.   Otto, O. *et al.* Real-time deformability cytometry: on-the-fly cell mechanical phenotyping. *Nat Methods* **12**, 199–202, 4 p following 202 (2015).

266.   Paik, S. *et al.* A multigene assay to predict recurrence of tamoxifen-treated, node-negative breast cancer. *N Engl J Med* **351**, 2817–2826 (2004).

267.   van 't Veer, L. J. *et al.* Gene expression profiling predicts clinical outcome of breast cancer. *Nature* **415**, 530–536 (2002).

268.   Saha, A., Harowicz, M. R., Wang, W. & Mazurowski, M. A. A study of association of Oncotype DX recurrence score with DCE-MRI characteristics using multivariate machine learning models. *J Cancer Res Clin Oncol* **144**, 799–807 (2018).

269.   Symmans, W. F. *et al.* Long-Term Prognostic Risk After Neoadjuvant Chemotherapy Associated With Residual Cancer Burden and Breast Cancer Subtype. *J Clin Oncol* **35**, 1049–1060 (2017).

270.   Carlson, P. *et al.* Targeting the perivascular niche sensitizes disseminated tumour cells to chemotherapy. *Nat Cell Biol* **21**, 238–250 (2019).

271.   Albrengues, J. *et al.* Neutrophil extracellular traps produced during inflammation awaken dormant cancer cells in mice. *Science* **361**, eaao4227 (2018).

272.   FastQC: a quality control tool for high throughput sequence data – ScienceOpen. https://www.scienceopen.com/document?vid=de674375-ab83-4595-afa9-4c8aa9e4e736.

273.   Hennig, C. *fpc: Flexible Procedures for Clustering*. (2020).

274.   Zong, Y., Goldstein, A. S. & Witte, O. N. Dissociated Prostate Regeneration under the Renal Capsule. *Cold Spring Harb Protoc* **2015**, pdb.prot078063 (2015).